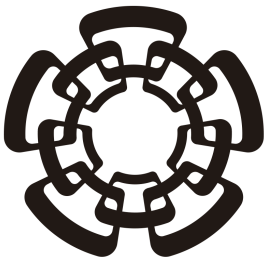

CENTRO DE INVESTIGACIÓN Y DE ESTUDIOS AVANZADOS DEL INSTITUTO POLITÉCNICO NACIONAL

UNIDAD ZACATENCO

PROGRAMA DE DOCTORADO EN NANOCIENCIA Y NANOTECNOLOGÍA

Mejora en la emision del infrarrojo cercano bajo luz UV en fosforos de CaF_2:Nd/Yb/Li.

T E S I S

Que presenta

M. en C. Jessica De Anda Gil

Que para obtener el grado de

Doctor en Ciencias en Nanociencias y Nanotecnología

Director de Tesis

Dr. Ciro Falcony Guajardo

Ciudad de México **Mayo, 2022**

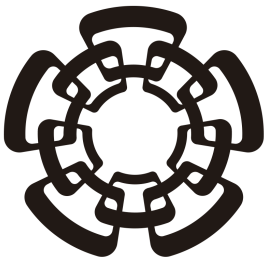

CENTRO DE INVESTIGACIÓN Y DE ESTUDIOS AVANZADOS DEL INSTITUTO POLITÉCNICO NACIONAL

UNIDAD ZACATENCO

PROGRAMA DE DOCTORADO EN NANOCIENCIA Y NANOTECNOLOGÍA

Improvement of NIR emission upon UV light in CaF_2:Nd/Yb/Li phosphors

T H E S I S

Submited by

M. en C. Jessica De Anda Gil

To obtain the academic degree

Doctor en Ciencias en Nanociencias y Nanotecnología

Thesis Advisor

Dr. Ciro Falcony Guajardo

Mexico City **May, 2022**

A todos los que creyeron en mí.

Agradecimientos

A CONACyT por el apoyo económico brindado, con la beca 640301.

Al Centro de Investigación y Estudios Avanzados del Instituto Politécnico nacional (CINVESTAV), por prestarme sus instalaciones y un lugar donde poder trabajar y desarrollar mi trabajo de tesis.

Al programa de Nanociencias y Nanotecnología por el conocimiento y experiencia adquirida a través de los talleres, seminarios y conferencias organizadas y de las clases impartidas por profesores que se encuentran dentro del programa.

A mi familia, mi mamá Josefina Gil González, mi papá Jaime De Anda Ontiveros, mi segundo papá y tío Ignacio Gil González, mi tía Beatriz Gil González y mis hermanos Janeth De Anda Gil y Jonathan De Anda Gil por todo el apoyo incondicional que siempre me han dado, por el amor y el cariño que me han dado, con el que siempre me trataron y el que me inculcaron, por enseñarme como se deben hacer las cosas y a perseverar. Pero sobre todo gracias por siempre creer en mí.

A familia en el ámbito académico, mi maestro, amigo y director de tesis el Doctor Ciro Falcony Guajardo, quien supo guiarme en todo momento, me mostró el camino de la ciencia y la investigación, me enseñó y corrigió cuando era necesario, me inspiró, me alentó y apoyo incondicionalmente en todo este proceso y algunos procesos personales, por su gran

aportación en este trabajo, por compartir sus ideas y sus enseñanzas tanto académicas como personales. A mis colegas (hermanos mayores) y amigos Dra. Evelyn Huerta, Dr. Uriel Balderas, Dr. Vicente Vargas, Dra. Miriam Téllez, por adentrarme en el mundo de la síntesis, enseñarme, alentarme e inspirarme con su trabajo y personalidad, por siempre apoyarme y compartir conmigo su conocimiento e ideas, por impulsarme, contribuir a este trabajo y siempre apoyarme en diferentes situaciones de mi vida. A mis amigos (hermanos menores) y colegas, Luis Alberto Becerril, José Iván Olivera, Bibiana Rodríguez, por compartir ideas, por las charlas, por las risas, por apoyarme en todo. Al Dr. Iván Merlín y Dr. Salvador Carmona, quienes me alentaron y me dieron confianza desde el primer día que llegue al grupo y quienes continúan enseñándome el camino.

A los miembros de mi comité tutorial Dr. José Gerardo Cabañas Moreno, Dr. Omar Solorza Feria, Dr. Yasuhiro Matsumoto Kuwahara, Dr. Manuel García Hipólito por todo el apoyo, los comentarios, preguntas y sugerencias que permitieron enriquecer este trabajo.

A los coordinadores del progama Dr. José Gerardo Cabañas Moreno y al Dr. Arturo Isaías Martínez Enríquez, por su gran labor y apoyo durante toda mi estancia.

A mis apreciados amigos, Sandra Amaro, Rebeca Ramírez, David Villanueva, Alejandro Ruiz, Arturo Zalapa, Job Quiroz, Rocío Yazmin ("Roomie"), Carlos Ramírez, Valeria González, Daniel Silva, Jenny Hernández, Marlene, Chepe, Ángel Mandujano, Pabel Carrillo, sin importar el orden en que los nombre, gracias por todos sus consejos, por apoyarme durante todo este camino, por estar ahí incondicionalmente, por sus abrazos, por sus palabras, por impulsarme en mi crecimiento y hasta por aguantarme.

A Zacarias Rivera, técnico del laboratorio y amigo, por todo el apoyo y ayuda durante mi estancia en el laboratorio, por todas esas veces que me salvo de incendiar el laboratorio,

por todas las charlas, por todo el aporte que dio a mi trabajo de tesis, por los consejos y el apoyo moral que siempre me brindo. A Diana por la disposición, apoyo en congresos y por la mano y sonrisa sincera que siempre me brindo. A las auxiliares de investigación Marcela Guerrero, Ana Soto, quienes siempre mostraron disposición y apoyo en todas las mediciones requeridas, por su contribución en mi trabajo y por todos los consejos en estas y otras circunstancias.

A Roxana Yazmin De Lorenz, secretaria del Posgrado y amiga, por apoyarme en todos los trámites desde el comienzo de esta nueva etapa, por las charlas, por escucharme y por sus valiosos consejos.

Y a la incondicional y amorosa compañía de mi gatito Snowy y de Piloncillo.

Resumen

El incremento constante de consumo de energía produce problemas ambientales debido a la generación de la misma. Por lo que es importante desarrollar soluciones sustentables. Una excelente opción es hacer uso de la energía solar a través de celdas solares. Sin embargo, las celdas solares de Silicio (Si) tienen un límite de eficiencia del 30% aproximadamente, esto a causa de diferentes parametros, uno de ellos, el principal, es el desfase que existe entre el espectro electromagnético solar y la zona de absorpción de la celda fotovoltaica. Por esta razón y con el fin de mejorar dichas eficiencias, se han sintetizado y estudiado materiales dopados con lantánidos, materiales luminiscentes que son también conocidos como fósforos, para ser usados en forma de peliculas sobre celdas solares como concentradores/convertidores de luz. Por lo que en este trabajo, se sintetizaron y caracterizaron fósforos de CaF_2 dopados con Nd, Yb y Li, como materiales para mejorar la eficiencia de celdas solares de Silicio. Los fósforos mencionados anteriormente se caracterizan por tener absorciones en el rango del ultravioleta y visible, picos característicos de las transiciones del Nd y su transferencia de energía a los iones Yb, los cuales emiten eficientemente en el infrarrojo cercano, en el rango de 975 nm, que es altamente eficiente para las aplicaciones de celdas solares. En particular la absorción del UV, da lugar a procesos de Down conversion (DC), en los que un fotón absorbido en el UV es convertido en dos fotones emitidos en el NIR. Los fósforos de CaF_2:Nd/Yb/Li fueron sintetizados mediante las técnicas de coprecipitación e hidrotermal, encontrando mejores condiciones estructurales en los fósforos sintetizados por la técnica hidrotermal, esto debido a las condiciones de presión y temper-

atura de la técnica. Se determinó que incorporación de Li en la estructura de estos fósforos mejora en un factor de hasta cinco veces la intensidad luminiscente en el infrarrojo cercano. Esto es debido a que iones de Li fungen como compensadores de carga, promoviendo una mejor cristalinidad y reduciendo procesos no radiativos en este material. Por otro lado, se confirmó que en estos materiales se producen procesos *downconversion* excitando estos fósforos con luz UV, lo que permite tener una mayor eficiencia de rendimiento cuántico en la emisión en el infrarrojo cercano, comparado con los fósforos excitados con luz visible. Lo cual podría mejorar la eficiencia de las celdas solares que incorporan este material como concentrador/convertidor solar.

Abstract

The continuous increasement in energy consumption leads to environmental problems associated with its production. Consequently, environmentally sustainable solutions are essential. In order to address this problem, solar cells will be an excellent solution through the use of photovoltaic generation. However, in the Si solar cell, efficiency is limited to 30 % due to poor matching between solar spectra and the photovoltaic sensitivity of the Si cells. Hence, light concentrators/converters based on lanthanide-doped materials are being added as layers to solar cells to overcome these inefficiencies. This work describes the synthesis and characterization of Nd, Yb, and Li codoped CaF_2, which are materials for improving silicon solar cells. These phosphors exhibit ultraviolet and visible absorption, as a result of characteristic transitions between electronic energy levels of Nd, and a near-infrared emission at 975 nm, characteristic of radiative recombination transition within electronic energy levels of Yb, which is highly efficient for Si solar cells. Particularly upon UV ligh excitation, where down conversion occurs. This process involves the absorption of a UV photon and the emission of two NIR photons. CaF_2:Nd/Yb/Li phosphors were synthesized by either coprecipitation or hydrothermal methods. The phosphors synthesized by hydrothermal techniques had better structural properties due to the temperatures and pressures involved. Furthermore, Li incorporation in these phosphors enhances the luminescent intensity up to five times in the near-infrared. This occurs because Li ions acting as charge compensators, improving crystallinity and reducing non-radiative transitions. Additionally, CaF_2:Nd/Yb/Li phosphors have been demonstrated underggo down

conversion processes that enhance quantum yield efficiency in NIR and make solar cells with light concentrators/converters that incorporate this material more efficient.

Contents

List of Figures

List of Tables

Introduction

The consumption of energy and its production continuously results in environmental problems. The study of sustainable energies and the technology behind harvesting them has boomed considerably in the last half-century. In particular, solar energy is one of the most promising alternatives. Unfortunately, not all solar energy can be used. If all solar energy could be used, humans' total energy requirements could be met. Currently, photovoltaic solar cells are the most commonly used devices to harvest solar energy. There are, however, some limiting factors that make it impossible to get and use solar energy effectively. In solar cells, silicon (Si) is the most common material, with a bandgap of 1.12 eV. Consequently, photons with lower energy cannot be absorbed, and photons with higher energy use the necessary energy to overcome the energy gap, and the rest is thermally wasted. In 1961, Shockley and Queissier calculated the theoretical efficiency of silicon solar cells and estimated that this phenomenon limits the maximum efficiency to 30 %. Therefore, some efforts have been made to get around this limit. Silicon quantum dots (Si-QDs) deposited as films on solar cells reduce solar cell reflection, increasing solar cell absorption [2]. Films comprised of perovskite-quantum dots improve perovskite solar cells (PSCs), modifying their crystalline structure performance [3] . In addition, there are also down-conversion (DC) and up-conversion (UC) materials based on lanthanides that utilize energy transfer processes to produce extra electrons-holes pairs, thereby improving the efficiency of solar cells. Up-conversion refers to the process in which two or more photons are converted into one photon with a higher energy. While down-conversion also called quantum cutting, is

the process by which one higher-energy photon is transformed into two lower-energy photons. Hence, our goal is to develop DC materials based on lanthanides that can improve the efficiency of Si solar cells

The first application of DC matherials in solar cell was studied theoretically by Trupke et al. in 2002 [4]. They showed that a Si solar cell can achieve 38.6 % of maximum power conversion efficiency (PCE) with an ideal DC layer and unconcentrated sunlight.

In DC luminescent materials, the energy transfer between lanthanide ions constitutes an important aspect. To assure the successful energy transfer between ions, materials with a large bandgap and low phonon energy are used as host matrices to avoid multiphonon nonradiative relaxations between spaced energy levels of lanthanides ions. Oxides and fluorides are typically used as hosts for lanthanides, because of their wide bandgaps and low phonon energies. There are a variety of fluorides that are used as matrix, showing the DC process, for example, KY_3F_10 [5], LaOF [6].Furthermore, $NaYF_4$ doped with Ho^{3+} and Yb^{3+} was synthesized via the hydrothermal method by Deng et al.[7], achieving an efficiency of 115,2 %. Pr^{3+}/Yb^{3+} codoped $Na_5Y_9F_{32}$ was obtained by Hu et al.[8] in 2018 where a theorical quantum efficiency of 180 % was calculated. CaF_2 is also a good host for pairs of lanthanides, Eu^{2+}/Yb^{3+} [9], Er^{3+}/Yb^{3+}[10], Eu^{3+}/Tb^{3+}[11], Tb^{3+}/Yb^{3+}[12, 13], Ce^{3+}/Tb^{3+} [14, 15], Eu^{2+}/Tb^{3+} [16, 17], Ce^{3+}/Yb^{3+} [18, 19], with solar cell applications from the Ultraviolet (UV) to visible or Near Infrared Region (NIR). In this work, CaF_2 was selected as a matrix to be codoped with lanthanides for photovoltaic applications. Nd^{3+} was chosen as a collector of UV energy in order to transfer energy to Yb^{3+}, since it emits on only one energy level in the NIR region. Nd^{3+} and Yb^{3+} codoped CaF_2 crystals were reported for the first time by V. Petit et al. for laser applications[20]. However, DC analyses of these materials have not been performed. Here, nanostructured phosphors of CaF_2:Nd/Yb were synthesized, analyzed, and enhanced as a material to improve the

efficiency of solar cells.

The first chapter of this study reviews energy problems and challenges, possible solutions, and how luminescent materials based on lanthanides play a crucial role in this field. Lanthanides and their optical characteristics are explained in the second chapter. In the third chapter, two synthesis methods of luminescent materials based on lanthanides are presented, coprecipitation and hydrothermal. The fourth chapter explains why Nd and Yb doped CaF_2 were selected, and how they influence the optical and structural properties of this material when synthesized by coprecipitation and hydrothermal processes. Chapter five describes the changes in crystallinity and luminescent properties caused by Li incorporation in CaF_2:Nd/Yb phosphors. Chapter six concludes with a study and discussion about down-conversion in optimized CaF_2:Nd/Yb/Li phosphors.

Chapter 1

Energy and Silicon solar cell challenges

1.1 Energy challenges

Increasing electricity consumption results in increased carbon dioxide emissions annually, resulting in environmental damage. The global electricity demand decreased by 1 % as a result of the COVID-19 pandemic but grew by more than 5 % in 2021 [21]. Due to this, the study, development, and applications of renewable energy technologies have increased in order to mitigate the consequences and risks associated with other energy sources. However, each technology poses its own set of challenges.

Solar energy is one of the most promising sources of sustainable energy because the Sun provides more energy to the earth in less than one hour than the world consumes in a year [1]. Solar energy applications face challenges related to efficient harvesting, conversion, and storage. Sunlight can be harvested in various ways, including solar thermal systems and solar cell technology, converting sunlight into electricity. One of the principal difficulties in harvesting and converting solar energy through solar cells are a mismatch between the solar spectrum and the solar cells. Variations in solar spectral distributions depend on the time of day, the season, latitude, weather conditions and limitations. Fortunately, the standard solar spectrum, AM1.5G, air mass of 1.5 [22] (figure 1.1), can be used as a reference. This

spectrum shows the intensity percentage in the UV, visible, and IR regions covered by Sun and the fraction that would be absorbed and available for photovoltaic conversion in crystalline Si solar cells.

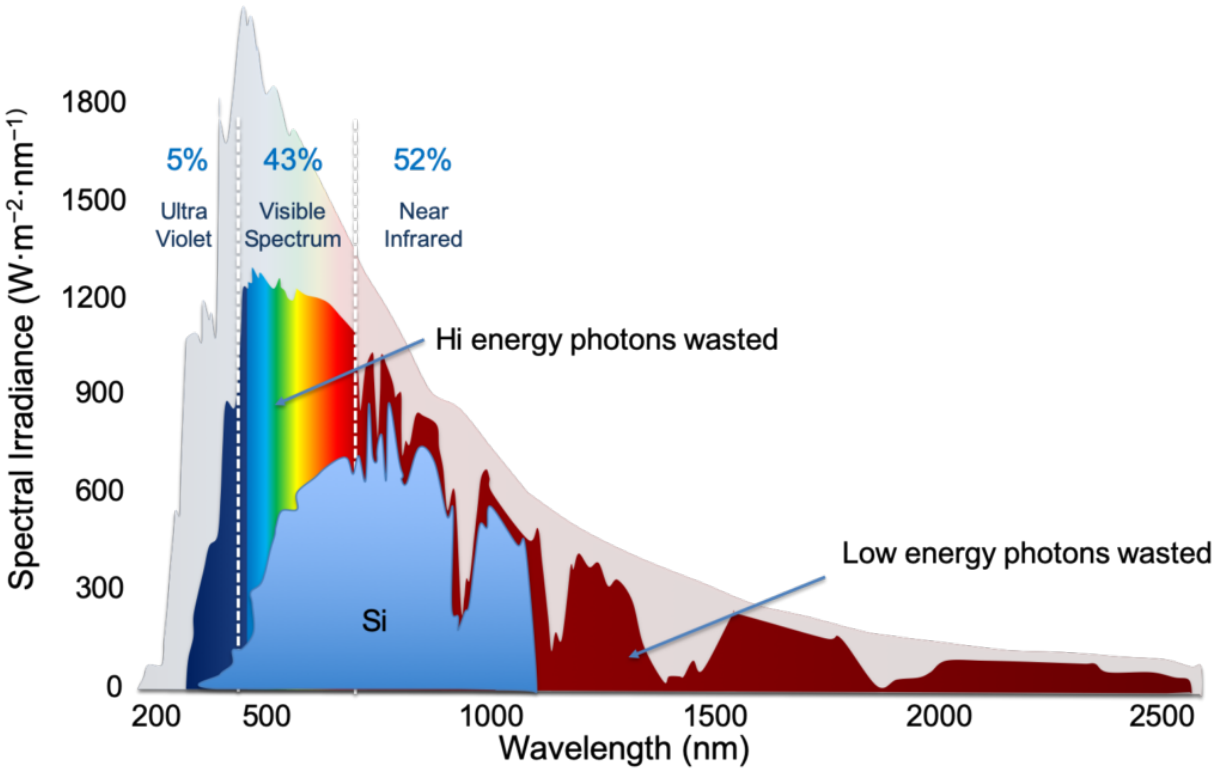

Figure 1.1: Air-Mass(AM1.5G) terrestrial solar spectrum, showing the fraction that is currently absorbed by a crystalline silicon device [1]

1.2 Photovoltaic cells

Solar cells are typically composed of p-type and n-type semiconductor layers. The semiconductor bandgap determines the minimum energy required to generate a single electron-hole pair. An electron is excited into the conduction band of a semiconductor when a photon with higher energy than the bandgap is absorbed in the valence band, leaving a hole and providing the solar cell with two charge carriers. The electrons in the conduction band

flow to the n-type side, while the holes in the valence band flow in the opposite direction, resulting in an electrical current. If the energy absorbed is greater than the bandgap semiconductor energy, most unused energy is relaxed in hot charge carriers. Due to this, the excess energy is dissipated as heat by thermalizing the electrons to the edges of the conduction and valence bands. Furthermore, solar cells are transparent to photons having lower energy than the semiconductor bandgap. This means that, depending on their energy photons might contribute to a more significant loss of solar energy efficiency. Accordingly, in 1961, Shockley and Queissier published the results of their theoretical calculations of the efficiency limit of silicon solar cells as 30 % [23]. About 80 % of the solar cell market is made up of crystalline Si solar cells (c-Si SC). Different types of materials have been studied and used in solar cell technologies, such as Cadmium sulfide (CdS), Cadmium telluride (CdTe), and Copper Indium Gallium Di-Selenide (CIGS). This approach is known as second-generation solar cell technology, without exceeding the theoretical Shockley-Queissier limit[24]. To improve efficiency and reduce costs, a third-generation that is based on dye-sensitized cells [25, 26], perovskite solar cells [27] and quantum dots solar cells [28] has been proposed, exhibiting low percentages of energy conversion efficiency. To improve this characteristic, intermediate band solar cells (IBSCs), have emerged and improved efficiency in conventional single gap solar cells [29]. Other alternatives are the reduction of recombination losses, using selective junctions, and incorporating hydrogen into amorphous and microcrystalline Silicon, a-Si:H and mc-Si, as well as Hydrogen passivated Silicon in Si/Perovskite Tandem Solar cells, reducing the charge recombination at the grain boundary which correlated to the degradation and recovery of passivation in amorphous Silicon [30–32]. Still other alternatives have been investigated, analyzed, and developed, such as heterojunction interdigitated back-contacted solar cells, organic solar cells, and hybrid solar cells, with the objective of improving efficiency and breaking the Queisser-Shockley limit [33]. Lanthanide-based luminescent layers are another excellent alternative for improving solar cell efficiency. In these materials, solar energy is better

utilized via internal processes such as downconversion, downshifting, and upconversion.

1.3 Downconversion, downshiting and upconversion to improve solar cell efficiency

The downconversion process (DC) involves the absorption and conversion of one higher energy photon into two lower-energy photons. Hence, this indicates that UV photons can be absorbed and create two electron-hole pairs and reduce energy loss due to thermalization.

A DC layer must be placed on the front surface to achieve the desired result in a single-junction solar cell. Additionally,in DC process the energy absorbed must be at least twice the bandgap semiconductor energy ($2E_g$). According to the AM1.5g spectrum, approximately 32 % ($149Wm^{-2}$) of the sunlight intensity can be used in the downconversion mechanism for c-Si SCs [34]. Hence, the maximum efficiency for a front-mounted downconversion layer was calculated for $E_g = 1.1$ eV given a value of 38.6 % [4], which exceeds the Queisser-Schokley limit.

The downshifting mechanism is similar to that of downconversion, but in this case, one higher energy photon emits just one lower energy photon, thereby improving the efficiency of solar cells without exceeding Queisser-Shockley limits.

Contrary to downconversion, upconversion adds two lower-energy photons to form one higher energy photon, which can be absorbed by solar cells. This mechanism involves two sequential transitions from the valence band to an intermediate level, followed by a transition to the conduction band. Taking into account the possible variation in intensities concerning air mass coefficients, the sunlight intensity for upconversion is approximately 35 % ($164\ Wm^{-2}$) [34].

Lanthanide ions are excellent candidates for use as spectral converters due to their multiple energy transitions. Furthermore, they have been studied and analyzed for potential use on solar cells as up-and-down converters.

Chapter 2

Physical and optical properties of Lanthanides

Lanthanides, also known as rare-earth elements, consist of 15 metallic elements with similar physical properties, ranging from lanthanum to lutetium, which have atomic numbers 57 to 71. The most common and stable oxidation state of lanthanide is 3+, which is usually founde in crystalline compounds. Also oxidation state of 2+ can be founded in Eu, Sm and Yb, which can reduce to 2+, because these divalent ions are unstable in oxigenated solutions [35]. The most common form of bonding between these elements is ionic coordination. Furthermore, these elements are more attracted to electronegative elements, including oxygen and flour.

Lanthanides are f-f block elements characterized by 4f valence orbitals, which are buried within the core and shielded from the filled 5s and 5p orbitals, except for lanthanum (La^{3+}), which has the 4f shell empty and lutetium (Lu^{3+}) which has a filled up 4f shell. These characteristics contribute to the specific luminescence properties, such as weak and narrowband emissions and long lifetimes of the excited states.

2.1 Luminescence in Lanthanides

Luminescence refers to the light emitted by a material that is not due to heat. Luminescence refers to a variety of processes, including chemiluminescence, bioluminescence, thermoluminescence, triboluminescence, and photoluminescence. The latter is caused by electromagnetic radiation (light excitation). Usually, the wavelengths of the emitted light are equal to or longer than the wavelengths of the excitation light, from ultraviolet (UV) to visible (Vis) or near-infrared (NIR). Lanthanides offer a wide range of energy levels, thus interlectronic state radiative transitions cover almost the entire electromagnetic spectrum, making them suitable for luminescence applications.

2.1.1 Absorption and emission photons in Lanthanides

In general, photon absorption involves enough energy transfered to an electron to cause it to jump to a higher an energy level. On the other hand, the emission photon is the radiative transition of an excited electron to a lower energy state. When the emitted photon has the same frequency, polarization, and direction as the incident photon, the process is known as stimulated emission. In the spontaneous process, photons are emitted randomly in a direction.

The absorption and emission of photons are promoted by nature light operators, such as the even-parity electric dipole (ED) operator, the odd-parity magnetic dipole (MD) operator, and the electric quadrupole (EQ).

2.2 Transitions of Lanthanide Ions

The emission and excitation lanthanide spectra result from transitions between electronic energy levels of the multiple excited electronic energy states of the lanthanide ion. Judd-Ofelt theory is the basic theory that describes the intensity of electrons' transition within the 4f configuration of a lanthanide ion. Three types of electronic transitions are involved in

lanthanide ions: sharp intra-configurational 4f-4f, broader 4f-5d, and broad charge-transfer transitions.

In lanthanides, transitions from the ground state to the excited state involve rearranging electrons in their f-orbitals. The allowed transitions are described by selection rules [36].

Laporte's parity is a selection rule which indicates that electric dipole transitions cannot connect states with the same parity. Hence, f-f transitions are forbidden by the electric dipole mechanism. Nevertheless, when lanthanide ions are under the influence of a ligand field, the selection rules are relaxed and partially allow the transitions. Moving 4f electrons can generate ligand fields. It occurs when Ln ions are inserted into a chemical environment, destroying the spherical symmetry of the Ln electronic structure [37]. Further, since 4f orbitals are shielded from the external environment by 5s and 5p shell orbitals, their mixing with close orbitals remains very small. The non-centrosymmetric interactions allow the mixing of opposite parity of electronic states into the 4f wave functions and partially transitions, called an induced electric dipole transition.

Electric dipole transitions have odd parity and can be considered as linear charge displacements. On the other hand, magnetic dipole transition corresponds to a rotational displacement of charge, which does not present changes upon inversion; thus, it has even parity. The order of magnitude of intensity is similar that of induced electric dipole transitions. Quadrupolar transitions are parity allowed and are much weaker than the two transitions mentioned above. Some electric dipole transitions are highly sensitive to the small changes in the Ln^{3+} environments. In fact, these transitions are called hypersensitive or pseudo-quadrupolar transitions because they tend to exhibit the same selection rules as electronic quadrupolar transitions [36]. A spin selection rule is also required, as no spin changes are expected. Because heavy atoms have large spin-orbit couplings, the spin selection rule is relaxed. Consequently, the non-degenerate energy levels of the 4f orbitals are caused by electronic repulsion, spin-orbit coupling, and the environment, specifically

the ligand field.

Differences between 4f energy levels are in the order of 10^4 cm^{-1} since the strongest interaction between electrons disrupts the degeneracy. Splitting energy levels into J-states is caused by spin-orbit interaction, which means interactions between electrons' magnetic moments due to their spin and the magnetic moments due to the movement around the nucleus. The order of splitting of these energy levels is the order of 10^3 cm^{-1}. The J-degeneracy is regularly not very pronounced due to 4f electrons are shielded from 5s and 5p orbitals. These splittings re of the order of 10^2 cm^{-1} and the degeneracy is partially removed in a coordination environment by the ligand field [38].

According to the Russel-Saunders scheme, J-states are written as $^{2S+1}L_J$, where S is the total spin-impulse momentum of the system. The angular momentum L is represented by S(L=0), P(L=1), D(L=2), F(L=3), G(L=4), H(L=5), I(L=6).

To identify the lowest energy levels in the ground state, Hund's rules must be applied.

1. The spin multiplicity (2S+1) should be a maximum.

2. The orbital angular momentum (L) should be a maximum.

3. Total orbital angular momentum (J) should be maximum if the sub-shell is more than half full; otherwise, it should be minimum.

Accordingly, if we consider a Nd^{3+} ion, it has an electron configuration of [Xe] $4f^3$, the electrons populating f orbitals are unpaired and the orbitals are less than half full (figure 2.1).The S value for Nd is S=Σs=3/2, and the L value is L=Σl=1+2+3=6. Therefore multiplicity is $2S+1=4$. And the J values are L+S, L+S-1, L+S-2, ..., L-S, from L+S to L-S, $6+3/2=15/2$ to $6-3/2=9/2$. It means that, the lowest energy term of Nd^{3+} is $^4I_{9/2}$. And the order of energies states in the ^4I of Nd^{3+} are $^4I_{9/2}$, $^4I_{11/2}$, $^4I_{13/2}$, $^4I_{15/2}$

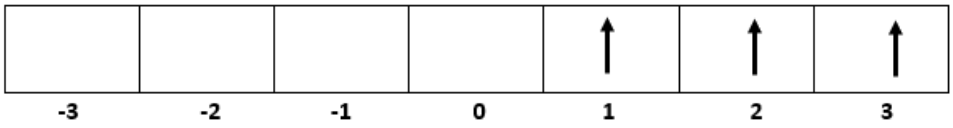

Figure 2.1: Diagram showing electron configuration of Nd^{3+}, $4f^3$.

In the case of Yb^{3+}, we have the next configuration [Xe] $4f^{13}$ (Figure 2.2). Where the S value is S=Σs=1/2 and the L value is L=Σl=-3+2(-2-1+1+2+3)=6-3=3. Hence, L=3 ->F, the multiplicity is 2S+1=1+1=2, and J has values from $L + S = 3 + 1/2 = 7/2$ to $L - S = 3 - 1/2 = 5/2$. Therefore, the energies states of Yb^{3+} are $^2F_{5/2}$ and $^2F_{7/2}$.

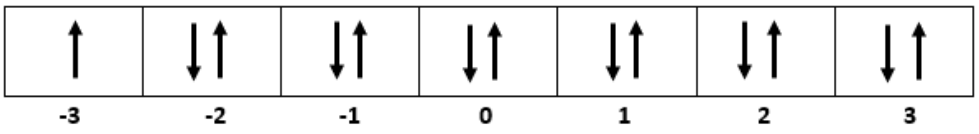

Figure 2.2: Diagram showing electron configuration of Yb^{3+}, $4f^{13}$.

Lanthanides possess a wide range of energy levels in the infrared and visible spectrum. Dieke reported the state energy levels of Ln from the 4f electron configurations in 1960 [39] and are presented in the following figure 2.3

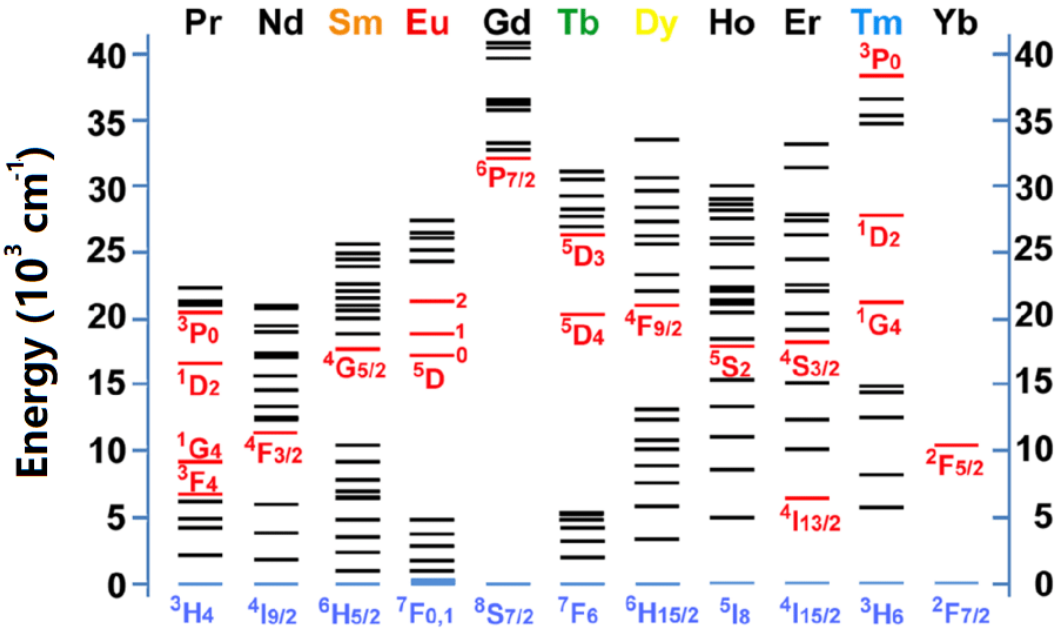

Figure 2.3: Energy Levels for the lanthanides ions.

2.2.1 d-f Electronic Trasitions

Interconfigurational 5d→4f transitions are orbital allowed by Laporte selection rule. Since the 5d orbitals are more sensitive to the surroundings of the lanthanides ions, the bands are broad, and their wavelengths are sensitive to the surroundings, which produces a shifting of the 5d centroid energy orbitals and a large splitting caused by the crystal effect. Transitions such as these are found in lanthanides that are readily oxidized, such as divalent Sm^{2+}, Eu^{2+}, Yb^{2+}, and trivalent lanthanides such as Ce^{3+}, Pr^{3+} and Tb^{3+} ions.

2.2.2 Charge-Transfer Electronic Transitions

Other allowed transitions are interconfigurational charge-transfer transitions which give rise to broad absorption bands, which is the case of O^{2-} ligands with some lanthanides, tetravalent Ce^{4+}, Pr^{4+} and Tb^{4+}, and trivalent Sm^{3+}, Eu^{3+} and Yb^{3+}ions [40].

2.3 Radiative and non-radiative transitions

Radiative and non-radiative processes are involved in transitions. During a radiative transition, a photon is emitted. Radiative transfer is not always efficient; internal relaxation and multiple interactions between ions could reduce radiative transfer and release the energy in other ways. Due to competition between the non-radiative and radiative transitions, the quantum efficiency (QE) is limited.

Non-radiative relaxation could dominate the radiative decay when the energy between two energy levels is smaller than five times the phonon energy.

Moreover, energy can be dissipated by non-radiative transitions in the lattice matrix arising from vibrational modes surrounding the lanthanide ions. Vibrational relaxation takes place at a higher vibrational level of the excited state and then is relaxed to its lowest vibrational level. Molecules, such as O-H, N-H, and C-H bonds, with high energy vibration, quenching the luminescence because of the small mass and charge of hydrogen.

Internal Conversion (IC) is another non-radiative mechanism, also known as radiationless de-excitation. It occurs when an electronically excited vibrational state couples to a vibrational state with a lower electronic state such that the spin state remains. A transition between states with different spin multiplicities is called an intersystem crossing (ISC), which refers to a relaxation molecule transitioning from a singlet excited state to a triplet excited state with lower energy. CR is a phenomenon where a portion of the excitation energy of one ion is transferred to a neighboring ion, leading to a rapid decay from a lower energy level to the ground state. Concentration quenching is another non-radiative process; this process occurs primarily as a result of the migration of energy between lanthanide ions. Because of the excited energy state of lanthanide ions, they may migrate to the nearest ion instead of emitting a photon, thereby reducing their lifetimes. Luminescence can also be quenched through thermal, concentration, impurities. Also in inorganic solids, electrons de-excitation via population of lattices phonons represent a significant nonradiative process [41]

2.4 Energy Transfer

The emission and excited spectra of lanthanides result from transitions between multiple excited states. Specifically, transitions involving radiative processes.

This process can occur in a host doped with a single lanthanide ion, as well as in a host with two or more lanthanides ions. The energy transfer (ET) occurs between the donor ion, D, also called the sensitizer ion in literature, and the acceptor ion, A, also known as the activator ion. Energy can be transferred by radiative or non-radiative processes. A highly efficient energy transfer process involves resonance between the emission band of a sensitizing ion and the absorption band of an acceptor ion. The Dieke diagram indicated the potential for resonant energy transfer between ions pairs based on the relative positions of the Lanthanide ions (figure 2.4 (a)). Also, non-radiative energy can be transferred via non-radiative resonant energy, phonon-assisted non-radiative energy transfer, and cross-

relaxation (figure 2.4)

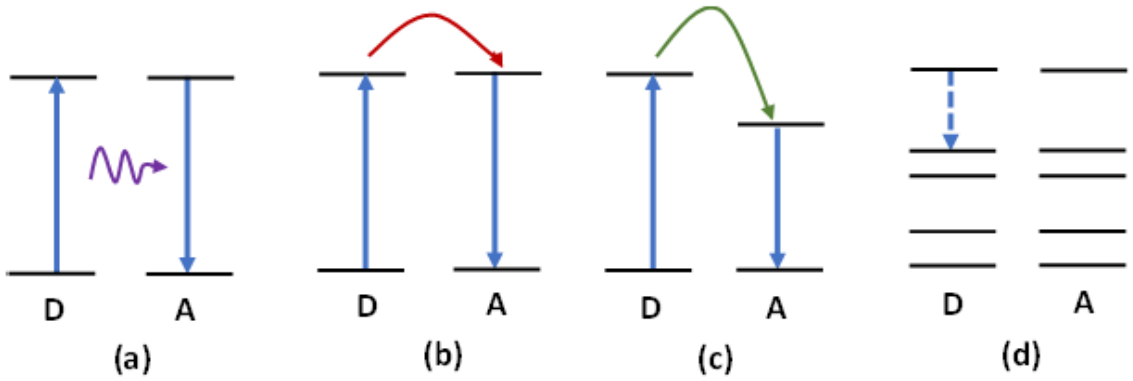

Figure 2.4: Representation of different energy transfer mechanisms. (a) Radiative energy transfer. (b) Non-radiative resonant energy transfer. (c) Phonon non-radiative energy transfer. (d) Cross-relaxation.

In order for ET to occur, two conditions must be met. Initially, the emission from the donor (D) and the emission from the acceptor (A) must overlap. This condition is known as the resonance condition. A second requirement is that two ions must interact either through an exchange interaction (wavefunction overlap) or a multipole-multipole interaction. Since the distance between acceptor and donor ions decreases exponentially the transfer probability, this P_{DA} can be calculated as following [42]:

$$P_{DA} = \frac{1}{\tau_D}\left(\frac{R_0}{R}\right)^6 \tag{1}$$

τ_D is the donor excited-state lifetime, including multi-photon relaxation, while R_0 is the critical distance where spontaneous deactivation of the excited donor state has the same probability as excitation energy transfer. To ensure high emission efficiency, each donor needs to have as many acceptor neighbors as possible, in order to increase the probability of energy transfer from donor to acceptor ions. However, if the ion concentration exceeds a certain concentration quantity, called critical concentration, the luminescence intensity will be reduced. This effect is known as *concentration quenching*.

2.4.1 Upconversion ET mechanisms

As was mentioned in section 1.3, upconversion (UC) is a mechanism where two lower-energy photons add up their energy to get a higher energy photon. One of the most efficient upconversion processes is APTE (Addition de Photon par Transferts d'Energie), often abbreviated as ETU (Energy Transfer Upconversion). The process involves two ions of type I absorbing a photon, transferring the energy to another ion of type II with a higher energy level. Energy is transferred in two steps via an intermediate level of type II ions that is close to that of type I ions. It can also be described as GSA/ETU, a ground state absorption (GSA) followed by an energy transfer step, figure 2.5(a). UP can also take place on a single ion I when the ion has already been excited and a second photon is absorbed to reach the higher energy level. The mechanism is described as GSA followed by excited-state absorption (ESA), figure 2.5(b). Other UP mechanisms involve one or more virtual energy levels, implying lower efficiency.

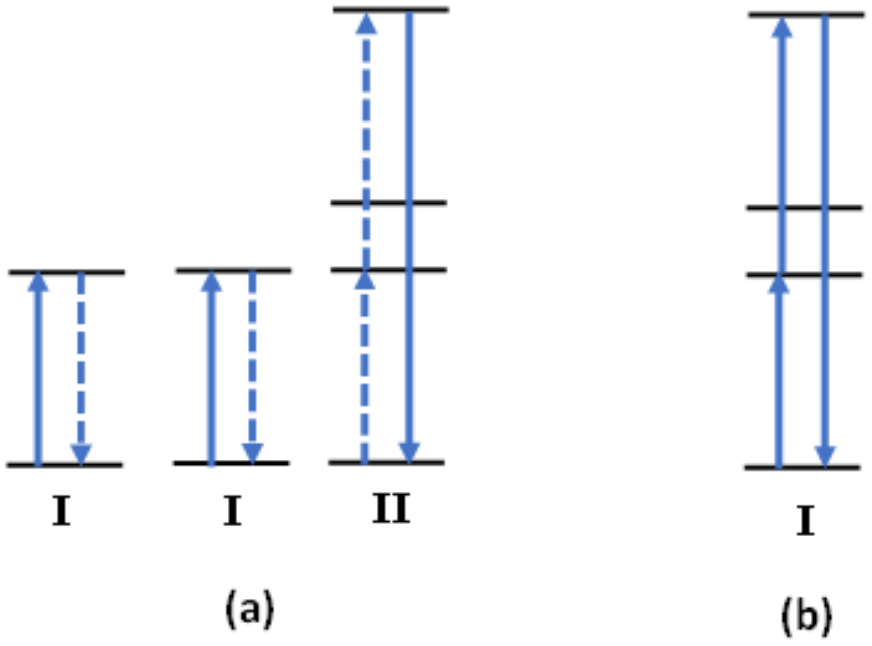

Figure 2.5: Energy levels scheme for UC mechanisms; (a) GSA/ETU, (b) GSA/ESA

2.4.2 Downconversion ET mechanisms

Downconversion on lanthanides pairs can take place in different ways. The first step is always the excitation of ion I. The energy can decay via cross-relaxation between ions I and II, followed by energy transfer between them, ending with emission from ion II. The emission of a photon from both ions is another mechanism that involves an energy transfer step between ions I and II. A cascade emission occurs when a high-energy photon is split into lower-energy photons on a single lanthanide ion.

2.4.3 Dexter ET

The donor energy transfer is carried out between two molecules, which exchange electrons. In a non-radiative exchange, two excited chemical groups, donor (D) and acceptor (A), exchange their electrons. In most cases, this exchange occurs at a short distance, typically 10 Å. The exchange mechanism is governed by Wigner spin conservation. The allowed spin process could be:

Singlet-singlet energy transfer

$^1D +^1 A \rightarrow^1 D +^1 A$

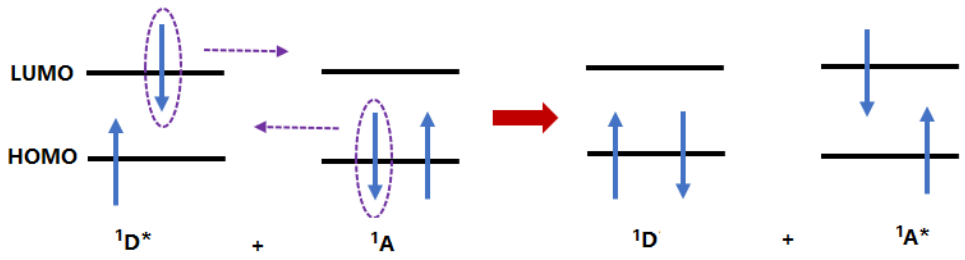

Figure 2.6: Schematic diagram for singlet-singlet Dexter energy transfer.

Triplet-triplet energy transfer

$^3D^* +^1 A \rightarrow^1 D +^3 A^*$

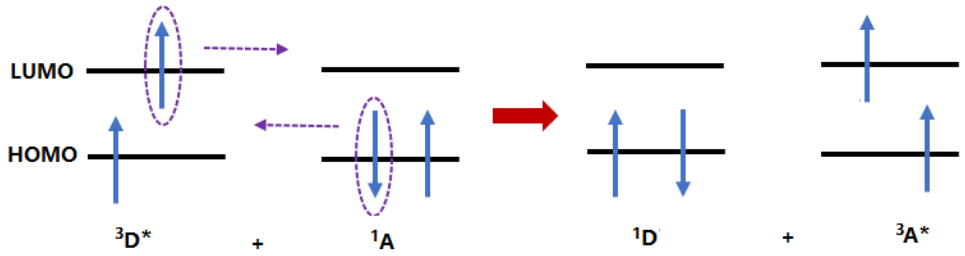

Figure 2.7: Schematic diagram for triplet-triplet Dexter energy transfer.

2.4.4 Föster ET

Föster or fluorescence resonance energy transfer (FRET) mechanism describes the energy transfer between two light-sensitive molecules (chromophores). In this transfer mechanism, a photon excited by a donor group, transfer energy to an accepto, through non radiative dipole-dipole coupling. The donor group is excited to the lowest excited singlet state, S_1. When the electron returns to the ground state, S_0, the energy released may excite the acceptor group simultaneously through non-radiative dipole-dipole coupling. This non-radiative process is also known as "resonance" (Figure 2.8). Finally, without quenching states, the excited acceptor emits a photon and returns to the ground state.

2.5 Photoluminescence lifetime

Photoluminescence lifetime is a measure of how long it takes for a molecule (or ion) to remain in an excited state before it returns to its lower energy state during a fast electronic deactivation process.

Measurements of luminescence lifetime are important because they provide fluorescence and phosphorescence bands. As a rule of thumb, lifetimes on the order of nanoseconds and picoseconds indicate phosphorescence, while lifetimes on the order of microseconds and more prolonged lifetimes indicate fluorescence.

All light emissions competing radiative and non-radiative processes, which generally

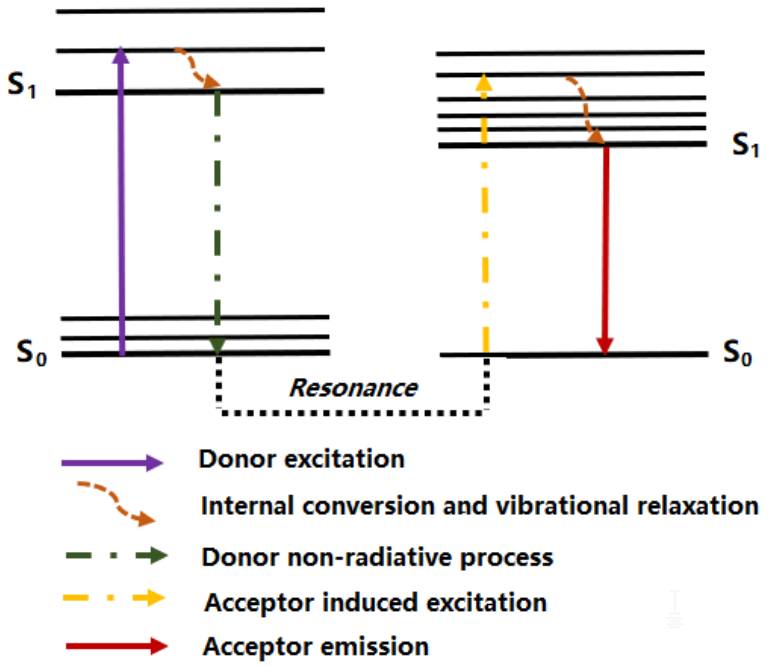

Figure 2.8: Schematic diagram for Föster resonance energy transfer.

generates shorter luminescence lifetimes than the natural lifetime. The fluorescence lifetime, τ, describes the combined rate of the radiative and nonradiative pathways.

$$\tau = \frac{1}{\Gamma + k} \tag{2}$$

Where Γ is the radiative and k the non-radiative processes.

In general non-radiative process have a slower decay time. Hence, luminescence decay time measurements can be used to obtain more information about internal processes. Vibrational relaxations process occur in 10^{-14} -10^{-12} s, while the internal conversion takes a time the order of 10^{-12} s, and intersystem crossing processes occur more slowly in a time scale the order of 10^{-8}.

All decay curves can be described by a double exponential decay time, the result of the

sum of a fast and slow exponential decay:

$$I(t) = I_0 + A_1 e^{\frac{1}{\tau_1}} + A_2 e^{\frac{1}{\tau_2}} \tag{3}$$

where $I(t)$ is the emission intensity at time t, I_0 is the intensity background constant, A_1 and A_2 are amplitude constants, and τ_1 and τ_2 are the fast and slow lifetime components, respectively.

2.5.1 Inokuti-Hirayama Model

The time evolution model for the fluorescence amplitude results from the Föster, Dexter and Inokuti-Hirayama theories is:

$$S(t) = Aexp(-t/\tau)exp[\gamma(t/\tau)^{\theta}] \tag{4}$$

Where A is the initial amplitude of the fluorescence, τ is the lifetime of the exponential fluorescence decay if there is no energy transfer, t is the time, γ is the scaling factor, and the exponent θ, characterizes the effect of energy transfer with a non-exponential result.

2.5.2 Bursthein Model

To obtain more information about transfer energy and other processes, the Burshtein model:

$$I(t) = I_0 \cdot exp(-\frac{t}{\tau_0} - \gamma_s t^{3/S} - w_m t) \tag{5}$$

where I_0 is the intensity at t=0, tau_0 is the average lifetime of the donor ion, γ_s is related with the direct energy transfer, w_s is the migration rate and $\boldsymbol{S}$ is related with the electric interaction and can take 6, 8 and 10 constant values, 6 for dipole-dipole (d-d), 8 for dipole-quadrupole (d-q) and 10 for quadrupole-quadrupole (q-q). Direct energy transfer

can be calculated through Inokuti-Hirayama model following the next equation [43, 44]:

$$\gamma = \frac{4\pi}{3}\Gamma(1-\frac{3}{S})N_A(\frac{R_0}{\tau_0^{1/S}})^3 \tag{6}$$

where N_A is the acceptor concentration and R_0 is the critical transfer distance.

2.6 Quantum Efficiency

Quantum efficiency in luminescent materials is defined as the ratio between the observed emission lifetime and the intrinsic lifetime:

$$IQE = \frac{\tau_o bs}{\tau_r ad} \tag{7}$$

The external (effective) quantum yield (QY_{eff}) measurements can be done using an integrating sphere. It is determined from the ratio of the number of photons emitted to the number of photons absorbed by the sample. To measure scattering spikes and the emission spectrum of a sample, two different detectors should be used. As a result, differences in sensitivity must also be considered, and the equation can be written as follows:

$$Q_{eff} = \frac{A_{em}}{(A_{scatref} - A_{scatsample})k_{Red-PMT/NIR-PMT}} \tag{8}$$

where A_{em}, represents the area of the number of photons emitted under the spectrally corrected emission peak for a sample. The number of photons absorbed is determined by the difference between the Rayleigh scattering peak areas of a reference sample and a study sample: $A_{scatref} - A_{scatsample}$. Finally, $k_{Red-PMT/NIR-PMT}$ is the ratio between sensitivities of the two detectors.

In the case of downconversion, a $QE > 1$ is expected.

Quantum efficiency in photovoltaic systems

By definition, quantum efficiency (QE) is the ratio of electrons collected by the solar cell to photons incident on it. In an ideal situation, each incident photon would produce an electron-hole pair. Despite this, the quantum efficiency of most solar cells is reduced due to recombination effects. Hence, by definition, $QE < 1$.

A device's external quantum efficiency (EQE) includes optical losses, such as transmission and reflection. Furthermore, the internal quantum efficiency (IQE) or internal quantum yield (IQY) is calculated by only taking into account photons that are not reflected nor transmitted from the cell and can produce carriers.

$$IQE = \frac{N_r ad}{N_t otal} \tag{9}$$

2.7 Sensitized Lanthanide

Because of unique luminescence properties, lanthanide ions have low absorption coefficients, of the order of $1\mathrm{M}^{-1}$ cm^{-1}[45], which is one of the disadvantages for efficient excitation. Not the case of organic molecules, for which excitation leads to a lengthening of chemical bonds, resulting in significant Stokes' shifts and broad emission bands due to the strong coupling with vibrations[36]. To overcome this drawback, lanthanides have been linked with a chromophore, which has a higher absorption coefficient, taking the roll of as antennas.

The energy transfer path between an organic ligand and lanthanides is the following; the antenna chromophore is excited into its singlet excited state; subsequently, the energy is transferred to the lanthanide ion through the intersystem crossing process. Generally, this process takes place via the antenna triplet state through the Dexter mechanism.

The success of the sensitization process can be demonstrated with the increase of the luminescence intensity. To have an efficient sensitization process in lanthanide complexes, the following conditions have to be considered:

The antenna should have a high absorption coefficient.

The antenna chromophore should be close to the lanthanide ion because the energy transfer process is strongly dependent on the distance.

2.8 Hosts of lanthanides

Most applications require the lanthanide ions to be incorporated into a matrix.Oxides and fluorides are suitable as host materials due to their wide bandgaps and low-energy phonons, which are less prone to multiphonon relaxations. It has been reported that CaF_2 has high chemical stability, low phonon energy, and optical transparency in a wide range of wavelengths [46]. Thus, CaF_2 has been used as a host for lanthanides [9–16, 18, 19]. These compounds have been synthesized using various methods, most commonly hydrothermal and co-precipitation.

Chapter 3

Synthesis luminescent materials based on lanthanides

To synthesize nanomaterials, a variety of techniques have been employed, including chemical vapor deposition, thermal decomposition, co-precipitation, solvothermal, hydrothermal, pulse laser ablation, combustion, and sol-gel. This Chapter focuses on the hydrothermal and co-precipitation methods.

3.1 Co-precipitation

One of the simplest and fastest syntheses methods is co-precipitation. These reactions are characterized by the simultaneous occurrence of nucleation, growth, and/or agglomeration processes.

In order to form a precipitate, chemical reactions are required. In this method, the nucleation process is a crucial step where many small particles are formed. The products are formed when supersaturation conditions prevail. The properties of these products are affected by secondary processes, such as aggregation and Ostwald ripening.

$$xAy^{+}_{(aq)} + yBx^{-}_{(aq)} \rightarrow AxBy_{(s)}$$

This method has additional advantages beyond its simplicity, including that it generally works at low temperatures and that composition can be controlled easily

3.1.1 Co-precipitation steps

At room temperature, stoichiometric amounts of precursors (lanthanides and host) are dissolved in deionized water and mixed using a magnetic stirrer. After that, the solution is left to precipitate for some hours (Fig. 3.1). It is centrifuged and washed at least twice in order to remove any possible remnants. Following this process, the product is vacuum dried. To improve their structural quality, the powers are then annealed.

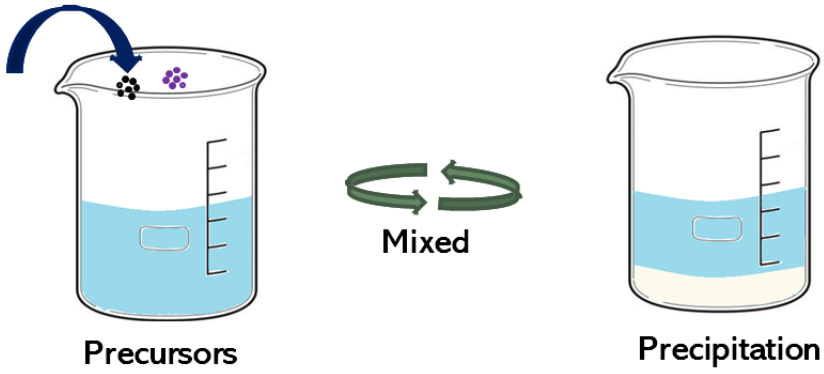

Figure 3.1: Main steps process of co-precipitation synthesis

3.2 Hydrothermal

Hydrothermal synthesis uses water as a solvent and, as a result, increases the solubility of the precursors through pressure and/or temperature.

Historically, hydrothermal synthesis was associated with geology. It was first used by British geologist Roderick Murchison (1792-1871) to describe the changes in the earth's

crust to form rocks and minerals due to the action of pressure and water at elevated temperatures.

The advantages of this technique include the ability to obtain products in a specific phase, intermediate state, or metastable state. The material can be controlled in terms of size, shape, and crystallinity with great precision. Furthermore, most materials can be dissolved in a suitable solvent due to pressure and temperature at their critical point. On the other hand, some disadvantages include the inability to observe the reaction process and the high price of the autoclave.

3.2.1 Hydrothermal steps

Stoichiometric amounts of precursors (lanthanides and host) are dissolved in deionized water and mixed by a magnetic stirrer at room temperature for a short time. The solution is transferred to a Teflon-lined autoclave and heated for some hours above 100 °C. The autoclave is left to cool down at room temperature (Fig. 3.2). Finally, the phosphors are washed, dried, and sometimes annealed.

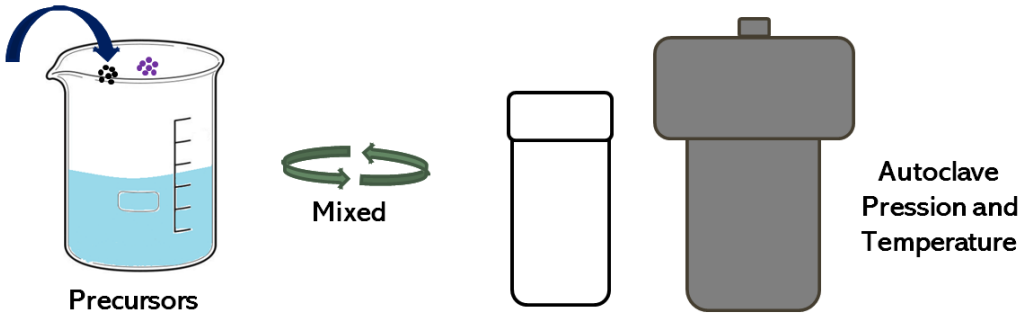

Figure 3.2: Main Hydrothermal synthesis steps

Thus, luminescent materials based on lanthanides have been synthesized by Coprecipitation and Hydrothermal methods. The materials' properties will be discussed and

compared in the next Chapter.

Chapter 4

Nd, Yb doped CaF_2 as luminescent material

This chapter describes the synthesis, characterization, and luminescent properties of CaF_2 doped with Nd and Yb phosphors.

CaF_2 was chosen as a host for lanthanides due to its excellent optical properties, low phonon energy, and chemical stability. In this study, Nd^{3+} was chosen because it is able to absorb in the UV and visible regions. UV-excited materials are desirable since DC processes occur within them. Yb^{3+}, the other lanthanide chosen, shows a unique transition energy level in the near-infrared, close to the absorption region of silicon solar cells. Thus, CaF_2:Nd/Yb phosphors can emit in the NIR and absorb in the UV and Vis regions due to energy transfer between Nd and Yb lanthanides.

4.1 Co-precipitation vs Hydrothermal method for CaF_2: Nd/Yb phosphors synthesis

The co-precipitation method (CP) is easier and faster than the Hydrothermal method (HT). However, due to the rapid nucleation and agglomeration processes, it can affect

the size and structural properties of the products, which is reflected in the luminescent characteristics [47]. On the other hand, Hydrothermal (HT) synthesis, because of high temperature and pressure reaction conditions, may avoid high agglomeration [48]. Thus, materials synthesized by HT typically have better crystallinity, which is reflected in their optical properties. Further, CaF_2:Nd/Yb phosphors were synthesized using both CP and HT methods in order to examine the structural and optical differences between these methods. In order to analyze them, X-Ray Diffraction (XRD) and photoluminescence (PL) measurements were performed.

4.2 Synthesis of CaF_2:Nd/Yb

4.2.1 Materials

To carry out the synthesis, the following materials were used: $CaCl_2 \cdot H_2O$ (99.0 %), $NdCl_3 \cdot 6H_2O$ (99.9 %), $YbCl_3 \cdot 6H_2O$ (99.9 %) and NH_4F (98.0 %) were purchased from Sigma-Aldrich.

4.2.2 Synthesis of CaF_2:Nd/Yb

The solution was prepared by dissolving stoichiometric amounts of $CaCl_2$, $YbCl_3$, and $NdCl_3$ in 10 mL of deionized water for 10 minutes. Fluoride was added to chloride solution by adding 15 mL of NH_4F solution (1 M).

Co-precipitation Synthesis

The chloride and fluoride solutions are mixed with a magnetic stirrer for 1 hour at room temperature in an air atmosphere to produce an opaque white suspension. In order to remove any possible remnants of the suspension, the suspension was washed at least two times with deionized water and centrifuged for 10 minutes at 5000 rpm. Afterward, the

material was dried in a vacuum at 60°C for 12 hours. In order to improve their structural quality, the phosphors were annealed gradually at 200°C for 30 minutes, 400°C for 30 minutes, and finally 600°C for an hour in an air atmosphere.

Hydrothermal Synthesis

The hydrothermal (HT) synthesis was conducted by mixing the chloride solution with NH_4F using a magnetic stirrer for ten minutes at room temperature (ambient atmosphere). The prepared sample was placed in an autoclave lined with Teflon and heated to 170°C for eight hours. The autoclave was to be cooled down to room temperature. Finally, the phosphors were washed, dried, and annealed using the same CP annealing procedure.

4.3 XRD analysis

Here, a comparison of structural lattice changes in CaF_2: Nd/Yb phosphors synthesized by CP and HT is described. XRD measurements were performed by Siemens D-500 diffractometer with CuKα ($\alpha = 1.54$). The XRD diffractograms from both methods are shown in Figure 4.1. The observed diffraction peaks and intensities for both diffractograms correspond to the CaF_2 cubic phase (standard PDF card #96-100-0044). In order to analyze possible changes in structure, a local magnification was carried out for the most intense peak, 202 (Fig. 4.1 b))

Local magnification (Fig. 4.1b)) reveals a shift towards lower angles (green and purple lines) and changes in the width at half maximum (FWHM). The characteristics are associated with the incorporation of lanthanides and the crystallinity of the material.
In the CaF_2 matrix, a charge neutrality initially exists; however, when lanthanides with 3+ charges are introduced, substituting divalent Ca ions, an unbalanced of charge is produced. In order to compensate the charge, more F^- ions are incorporated into the matrix, which results in charge repulsion between the F^- ions, increasing the lattice strength [49]. In

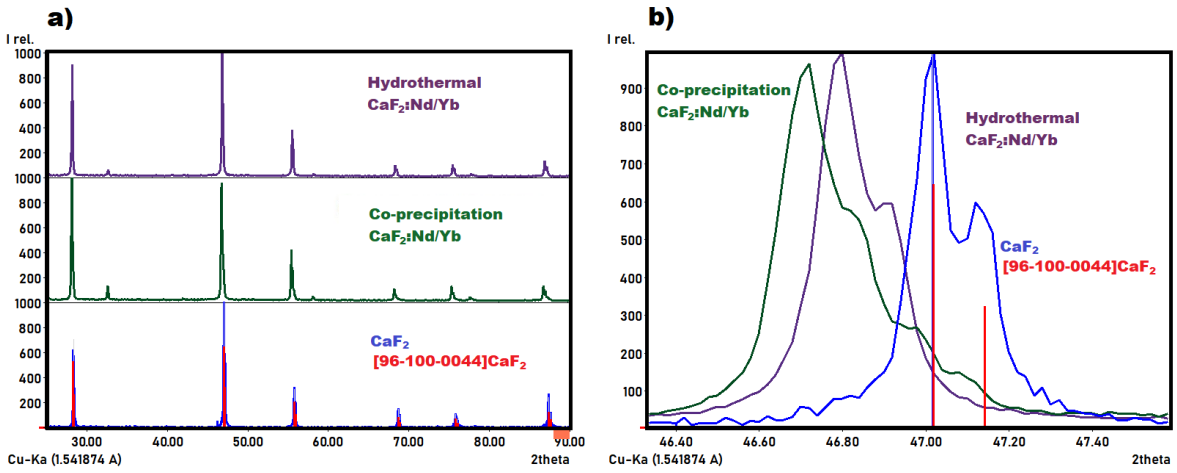

Figure 4.1: (a) XRD diffractogram of host CaF_2 (blue) and CaF_2:Nd/Yb synthesized by co-precipitation (green) and hydrothermal (purple) method. (b) Local magnification for the dominant peak (202).

consequence, the XRD peaks are shifted towards smaller angles [50].

The size of crystallites is inversely proportional to the peak FWHM increment. In order to determine the crystallite size of the two different materials produced, Scherrer's equation was used. Scherrer's equation can be expressed mathematically as follows:

$$D = \frac{K\lambda}{\beta cos\theta} \tag{1}$$

In the equation, K is a constant with a value of 1 based on a spherical approximation, lambda is the wavelength of the Cu-Kα radiation (0.15406 nm), beta is the full width at half maximum (FWHM), and theta is the Bragg's diffraction angle.

CaF_2:Nd/Yb phosphors synthesized by the CP method have a crystallite size of 75 nm, while phosphors synthesized by the HT method have a 55 nm crystallite size. Crystallite size is affected by the process involved in the synthesized methodologies. Particle formation and agglomeration occur rapidly in the CP method, which affect the size and characteristics of the products [48]. In contrast, HT processes utilize high temperatures and pressures,

resulting in nanomaterials with greater crystallinity and, therefore, less prone to agglomeration than those produced at low temperatures [51, 52]. Therefore, this crystallinity is reflected in the increasing intensity of NIR emission. In the subsequent analysis, only CaF_2:Nd4/Yb4 synthesized by the HT method is studied.

4.4 Scanning electron microscopy

The morphology of the CaF_2 and CaF_2:Nd/Yb particles was observed by scanning electron microscopy (SEM). The morphology in both cases is irregular (Fig. 4.2).
The morphology and size of particles do not significantly change with Nd and Yb incorporation on CaF_2. The particle size ranges from 25 nm to 280 nm for particle agglomerations.

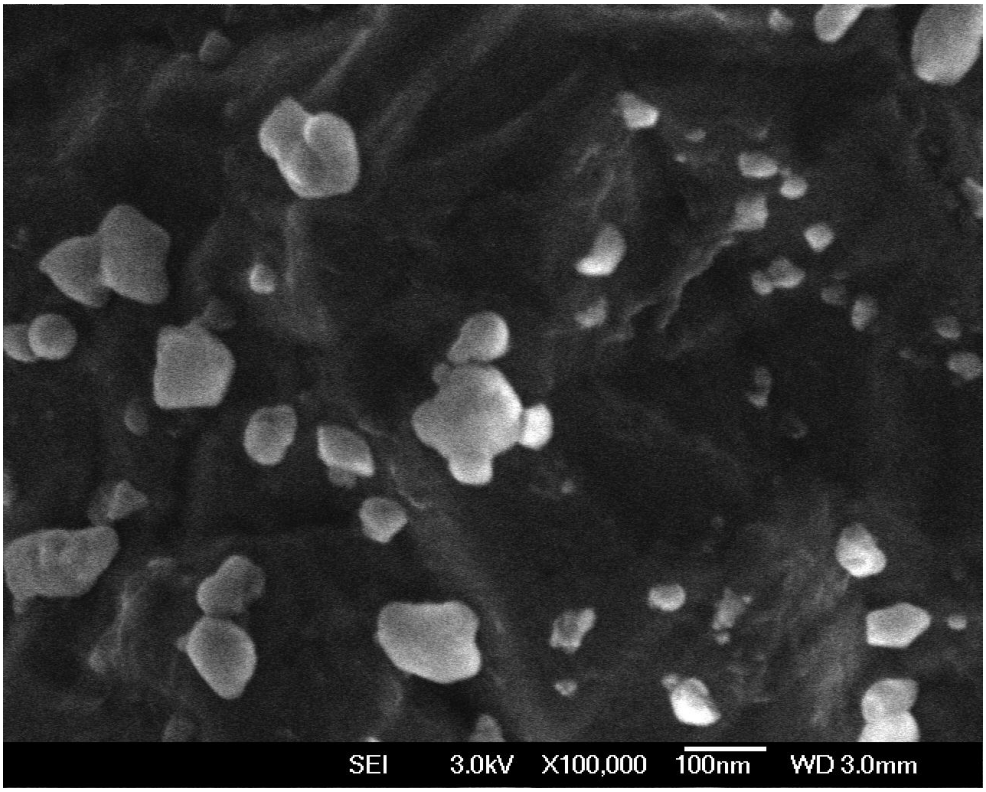

Figure 4.2: SEM image of CaF_2:Nd4/Yb4

4.5 Photoluminescence analysis

In this section, Nd and Nd/Yb codoped CaF_2 were synthesized, and luminescent spectra were analyzed and compared. The photoluminescence characteristics were obtained using an Edinburgh Instruments 980S spectrophotometer. To determine the most intense emission and excitation peaks of CaF_2:Nd4 phosphors, their emission and excitation spectra were analyzed.

The Nd excitation peaks are centered around 330, 353, 426, 460, 474, 508, 522, 572, 577, 624 and 674 nm, corresponding to the Nd^{3+} transitions from the $^4I_{9/2}$ ground state to the $^4D_{7/2}$, $^4D_{3/2}$, $^2P_{1/2}$,$^4G_{11/2}$,$^4G_{9/2}$,$^2G_{9/2}$,$^4G_{11/2}$,$^4G_{7/2}$,$^4G_{5/2}$,$^2G_{7/2}$,$^2H_{11/2}$ and $^4F_{9/2}$ excited states. The most intense peak are centered at 353 nm and 577 nm, corresponding to Nd and Nd^{3+} $^4I_{9/2} \rightarrow^4 G_{7/2}$ transition for the ultraviolet and visible region, respectively. In the UV spectrum, the maximum intensity peak occurs at 353 nm ($^{3+}$ $^4I_{9/2} \rightarrow^4 D_{3/2}$), while in the visible spectrum, the maximum intensity peak occurs at 577 nm ($^{3+}$ $^4I_{9/2} \rightarrow^4 G_{7/2}$) (Fig. 4.3). Both excitations correspond to transition energy levels of Nd. The emission intensity exhibited similar characteristics under UV (353 nm) and visible (577 nm) light, monitored at 1062 nm ($^4F_{3/2} \rightarrow^4 I_{11/2}$).

CaF_2:Nd4 presented two emission transitions on NIR region, under UV (353 nm) and visible (577 nm) wavelength excitation, corresponding to the $^4F_{3/2} \rightarrow^4 I_{9/2}$ (at 865 nm) and $^4F_{3/2} \rightarrow^4 I_{11/2}$ (at 1062 nm) of Nd^{3+}. When CaF_2:Nd4 is doped with Yb^{3+} ions, emissions transition of Nd are dissipated, prevailing, Yb transition $^2F_{5/2} \rightarrow^2 F_{7/2}$, at 975 nm over Nd transitions (Fig. fig:Lumin1), confirming the energy transfer(ET) process from Nd to Yb ions.

Additionally, photoluminescence properties of CaF_2:Nd doped with Yb^{3+} (CaF_2:Nd4/Yb4) have been examined, exciting Nd^{3+} trough UV (353 nm) and visible (577 nm) light, but

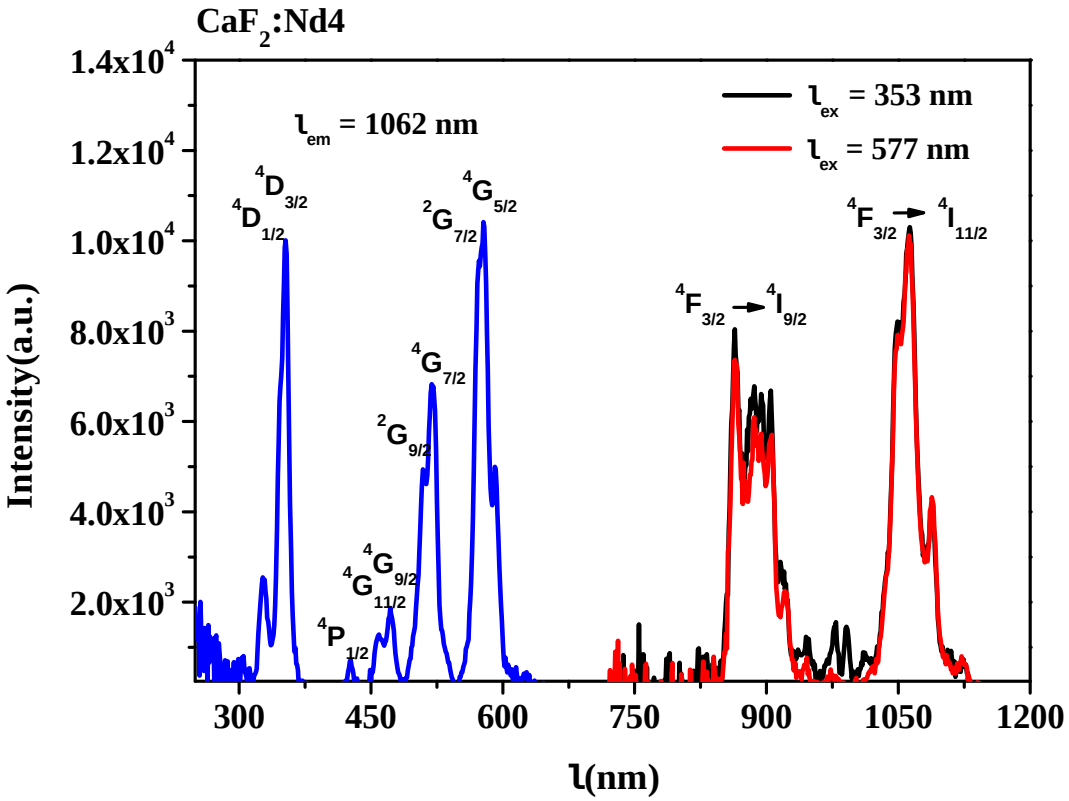

Figure 4.3: On the left side: UV and visible (blue line) excitation spectra for CaF_2:Nd4, monitoring the Nd^{3+} $^4F_{3/2} \rightarrow ^4I_{11/2}$ transition at 1062 nm. On the right side: NIR emission spectra upon 353 nm (Nd^{3+}: $^4I_{9/2} \rightarrow ^4D_{3/2}$, black line) and 577 nm (Nd^{3+}: $^4I_{9/2} \rightarrow ^4G_{5/2}$, red line) excitation.

monitoring Yb^{3+} transition at 975 nm ($^2F_{5/2} \rightarrow ^2 F_{7/2}$). CaF_2:Nd4 presented two emission transitions on NIR region, under both UV and visible light excitation, corresponding to the $^4F_{3/2} \rightarrow ^4 I_{9/2}$ (at 865 nm) and $^4F_{3/2} \rightarrow ^4 I_{11/2}$ (at 1062 nm) of Nd^{3+}. When CaF_2:Nd4 is doped with Yb^{3+} ions, emissions transition of Nd are dissipated, prevailing, Yb transition $^2F_{5/2} \rightarrow ^2 F_{7/2}$, at 975 nm over Nd transitions (Fig. 4.4), confirming the energy transfer(ET) process from Nd to Yb ions. CaF_2 emission was amplified by a factor of 15 in order to compare the emission spectra.

On the other hand the emission peak on 975 nm under 353 nm excitation light is

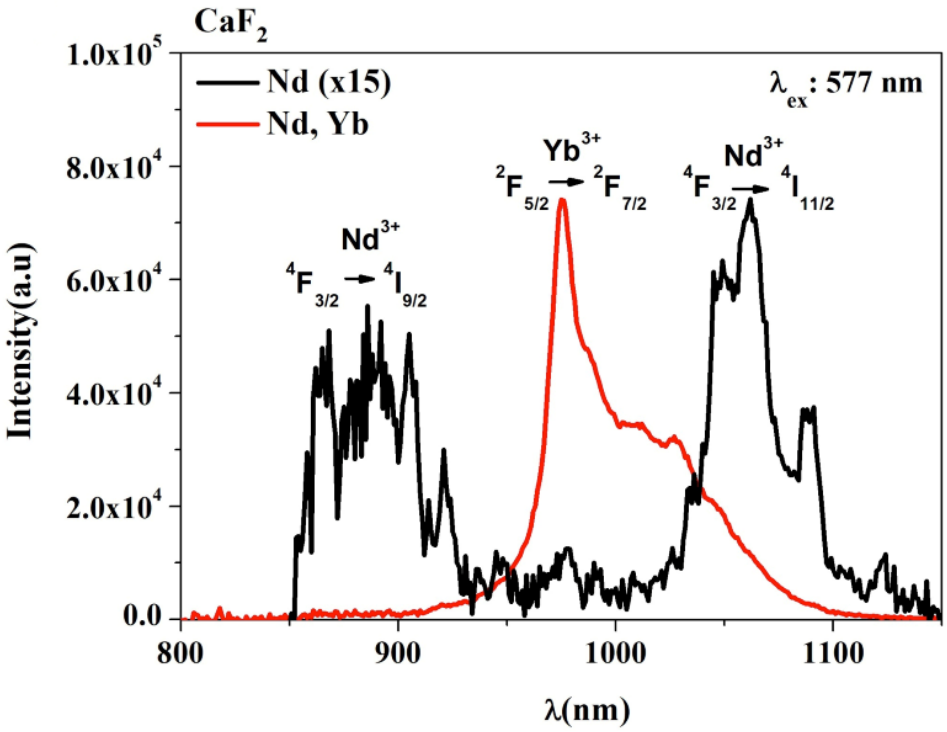

Figure 4.4: (a)CaF_2:Nd4 with (red line) and without Yb (black line) emission spectra upon excitation of Nd at 577 nm

considerably more intense than the Yb peak excited with 577 nm light, figure 4.5 which suggests a possible down-conversion process. (Fig. 4.4 (b))

4.6 Time decay analysis

A time decay analysis was performed in order to confirm the energy transfer. CaF_2:Nd4/Yb4 phosphors have been compared with CaF_2:Nd4, at the Nd transition for both, at 865 nm ($^4F_{3/2}$). There is a reduction of the lifetime of CaF_2:Nd4/Yb4 phosphors compared to CaF_2:Nd4, at 865 nm. It might be due to energy transfer efficiency. Accordingly, the

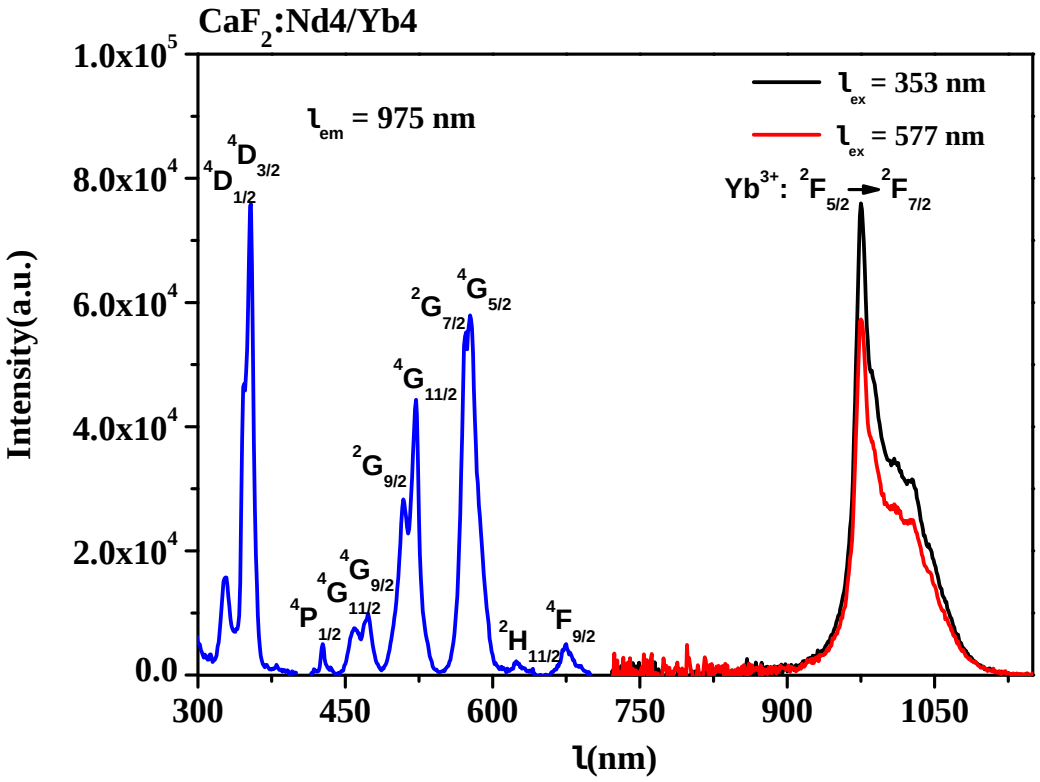

Figure 4.5: UV and visible (blue line) excitation spectra for CaF_2:Nd4/Yb4, monitoring the Yb^{3+} $^2F_{5/2}$ $\rightarrow ^2F_{7/2}$ transition at 975 nm. Further,on the right side, NIR emission spectra upon 353 nm (Nd^{3+}: $^4I_{9/2}$ $\rightarrow ^4D_{3/2}$, black line) and 577 nm (Nd^{3+}: $^4I_{9/2}$ $\rightarrow ^4G_{5/2}$, red line) excitation

following expression [53] was used to calculate the energy transfer efficiency:

$$\eta = 1 - \frac{\tau_d}{\tau_1^0} \tag{2}$$

Where τ_1^0 and τ_d are the average lifetimes of CaF_2:Nd4 in the absence and presence of Yb, respectively, in this case, the energy transfer efficiency was calculated using the Nd^3+ $^4F_{3/2}$ level decay time.

In this case, the energy transfer efficiency was calculated using the level decay time, obtaining a value of 0.17.

These phosphors exhibit two key characteristics. One is their increased emission intensity after the addition of Yb. A second feature is the intensity amplitude difference between UV and visible excitation, which can be related to a DC process. In Chapter 6, we will examine the verification of this process, but first, we will describe how Li can improve CaF_2:Nd/Yb phosphors.

Chapter 5

Improvement of CaF_2: Nd/Yb phosphors through Li addition

In the previous chapter, we discussed the optical and structural properties of CaF_2:Nd/Yb phosphors. Hence, structural modifications to the CaF matrix were found following lanthanide addition due to the extra positive charges of lanthanides (3+) when they replace the matrix's divalent cation (Ca^{2+}). In order to avoid vacances, Lithium ions were added as charge compensators. Here, we discuss the structural and luminescent changes in the properties of CaF_2: Nd/Yb phosphors synthesized by Hydrothermal due to the addition of Li^+. XRD diffractograms, Fourier-transform infrared spectroscopy (FT-IR), photoluminescence, and decay time spectroscopy were measured to determine the optical and structural changes.

5.1 Alkali metals as charge compensators

In luminescent materials based on lanthanides, alkali ions such as Na+, K+, and Li+ have been incorporated as charge compensators, improving luminescent properties [54–56]. Gupta et al. [57] have incorporated Na^+, K^+ and Li^+ ions into $SrWO_4$:Eu^{3+}. A better

luminescence emission was only achieved when Li^+ ions were incorporated.

According to some publications, this improvement is related to crystal structure changes, and increased crystal size [58–60].

5.2 CaF_2: Nd/Yb/Li phosphors Synthesis

For this study, CaF_2:Nd4/Yb4 phosphors with different Li^+ nominal concentrations, 0, 1, 2, 3, 4 mol % were synthesized by HT method.

5.2.1 Materials

In order to conduct the synthesis, the following materials were used: $CaCl_2 \cdot H_2O$ (99.0 %), $NdCl_3 \cdot 6H_2O$ (99.9 %), $YbCl_3 \cdot 6H_2O$ (99.9 %), LiCl (99.0 %) and NH_4F (98.0 %). The reagents were purchased from Sigma-Aldrich.

5.2.2 Synthesis procedure

Hydrothermal Synthesis of CaF_2: Nd/Yb/Li

Initially, stoichiometric amounts of $CaCl_2$, $YbCl_3$, $NdCl_3$, and LiCl were dissolved in 10 mL of deionized water for 10 minutes. Fluoride was incorporated into the chloride solution by adding 15 mL of a NH_4F solution (1 M). The solution was thoroughly mixed in a magnetic stirrer for 10 min at room temperature (ambient atmosphere) to be transferred to a 120 mL Teflon-lined autoclave and heated for 8 hours at 170 °C. The autoclave was allowed to cool down to room temperature. It was washed at least twice with deionized water and centrifuged at 5000 rpm for 10 minutes to remove any possible remnants. Following this, it was dried in a vacuum for 12 hours at 60°C. To increase the structural quality of the phosphors, they were gradually annealed, starting at 200 °C for 30 min, then at 400 °C for 30 min, then at 600 °C for 1 hr in an air atmosphere.

5.3 Lithium role in CaF_2: Nd/Yb phosphors

Incorporating RE3+ ions in the CaF_2 matrix results in the formation of lattice defects, mainly Ca vacancies, as a mechanism to maintain charge neutrality. Charge compensation can be explained by the following reactions [61]:

$$2Nd \overset{3CaF_2}{\longrightarrow} 2Nd^{\bullet}_{Ca} + V''_{Ca} \tag{1}$$

$$2Yb \overset{3CaF_2}{\longrightarrow} 2Yb^{\bullet}_{Ca} + V''_{Ca} \tag{2}$$

$$Nd + Yb \overset{3CaF_2}{\longrightarrow} Nd^{\bullet}_{Ca} + Yb^{\bullet}_{Ca} + V''_{Ca} \tag{3}$$

where $Nd^{\bullet}_{Ca}$ and $Yb^{\bullet}_{Ca}$ indicate a substituted Ca ion by RE (Nd or Yb) ion, while V''_{Ca} represents Ca vacancies.

In these vacancies, lattice defects are present. Furthermore, the substitution of lanthanides is not always perfectly proportional to the ratio 3:2, RE^{3+}:Ca^{2+} Hence, the excess of positive charges is compensate by fluorine ions. Fluorine ions enter in an interstitial way around the Ca vacancy. Accordingly, an increase in Nd^{3+} or Yb^{3+} ions concentration will result in a higher quantity of F^- ions required to neutralize the charge. When the quantity of F^- ions is increased, a strong charge repulsion is produced between them, causing an increase in the lattice constant [49]. Li^+ ions are introduced into the matrix to compensate the charge, as described in the following equations:

$$Nd + Li \overset{2CaF_2}{\longrightarrow} Nd^{\bullet}_{Ca} + Li'_{Ca} \tag{4}$$

$$Yb + Li \overset{2CaF_2}{\longrightarrow} Yb^{\bullet}_{Ca} + Li'_{Ca} \tag{5}$$

In this manner, the Li^+ ions would act as a charge compensator to avoid the interstitial entry of F^- ions, which result in lattice defects, promoting a higher level of crystallinity.

5.3.1 XRD analysis

The CaF_2:Nd/Yb phosphors containing different nominal Li^+ concentrations, ranging from 0 mol% to 4 mol%) were synthesized and compared to known structural changes, as shown in figure 5.1. All of the diffraction peaks correspond to the cubic phase of CaF_2, standard PDF card #96-100-0044. Thus, Li^+ ions can be introduced in concentrations up to 4 mol % without affecting the cubic phase of CaF_2. On the other hand, CaF_2:Nd/Yb doped with Li results in shifts of peaks towards higher and lower angles, as shown in Figure 5.1 (b). There is evidence to suggest that shifting of the diffraction peaks to higher angles is due to lattice contractions [62, 63]. As a consequence, the shifting observed in XRD diffractograms during the measurement of phosphors doped with Li^+ ions 1 mol % concentration can be attributed to the avoidance of interstitial F^- ions introduced to compensate for the charge in CaF_2 phosphors doped with lanthanides, which results in lattice expansion [49]. Furthermore, due to the minor ionic radius of Li ($\sim$ 0.92 Å) in comparison to Calcium ($\sim$ 1.12 Å), when Li ions replace divalent Ca ions, this led to a shrinkage of the host [58]]. It is also noted that shifting is reduced as the concentration of Li increases. The possibility arises from the fact that some Li ions are occupying interstitial spaces. Consequently, for diffractograms with up to 3 mol % Li concentration, the peaks start to shift toward smaller angles, and a distortion peak is visible for 4 mol % Li concentration.

Further, the peak width is reduced with an increase of Li concentration up to 3 mol %, which results in an increase in crystallite size. The crystallite size was calculated using Scherrer's equation. The crystallite size of CaF_2:Nd4/Yb4 with different Li concentrations is shown in 5.1

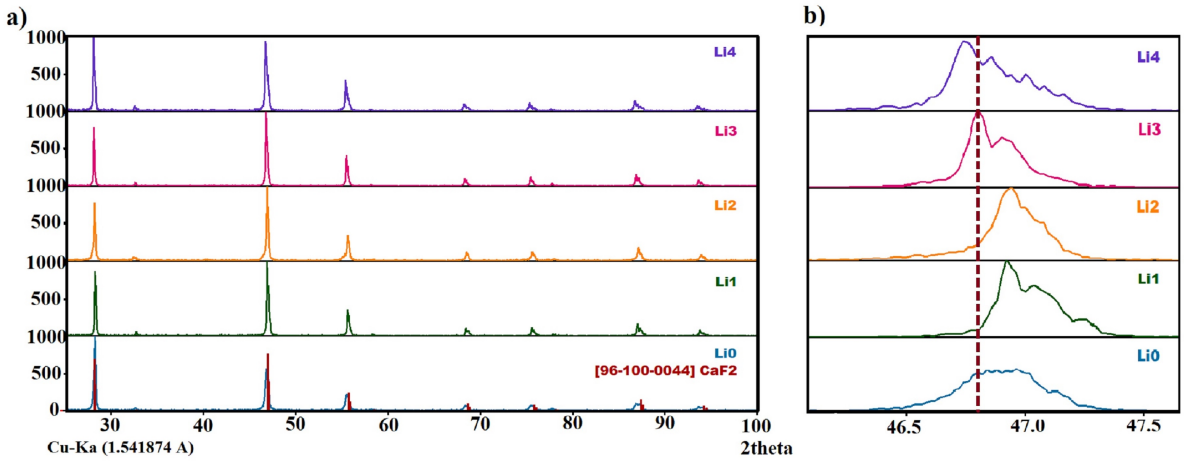

Figure 5.1: (a) XRD diffractogram of CaF_2:Nd4/Yb4 (blue), and CaF_2:Nd4,Yb4 with different Li concentrations by hydrothermal (HT) method and (b) local magnification for the dominant peaks. .

CaF_2:Nd4/Yb4/Li	Crystallite Size (nm)
0	25.04
1	35.27
2	54.90
3	93.32
4	67.31

Table 5.1: Crystallite Size of CaF_2:Nd4/Yb4 with different concentrations of Li (0, 1, 2, 3, 4)

5.4 EDS Analysis

Energy Dispersive Spectroscopy (EDS) was performed to verify the presence of Nd^{3+} and Yb^{3+} and confirming their composition in CaF_2:Nd/Yb and CaF_2:Nd/Yb/Li phosphors. EDS measurements are summarized in Table 5.2.

The at % of F^- to Ca^{2+} ratio keeps a proportion approximately of 2.3 times, for both samples, CaF_2:Nd/Yb and CaF_2:Nd/Yb/Li, while Ca^{2+} to RE^{3+} (Nd, Yb) ratio is approximately 0.043 for phosphors without Li^+ and the ratio decreases slightly to 0.035 with the Li^+ introduction. It is not possible detect Li^+ with EDS technique; however, the

Element	atomic percentage	element composition
Ca	30±1.25	29±4
F	68±1.22	69±4
Nd	1.3±0.1	1±0.1
Yb	1.3±0.1	1±0.1
Cl	0.3±0.05	0

Table 5.2: Atomic percentage composition of all elements from CaF_2:Nd/Yb and CaF_2:Nd/Yb/Li phosphors obtaining by EDS.

presence of this element was revealed through changes in crystalline nano-structure of the phosphors. Further, in the EDS spectra (Fig. 5.2) it is noticed the absence of chlorine in CaF_2:Nd/Yb/Li samples compared with low quantities of chlorine founded in samples synthetized without Li^+, suggests the introduction of Li^+ ions aid to reduce chlorides remnants.

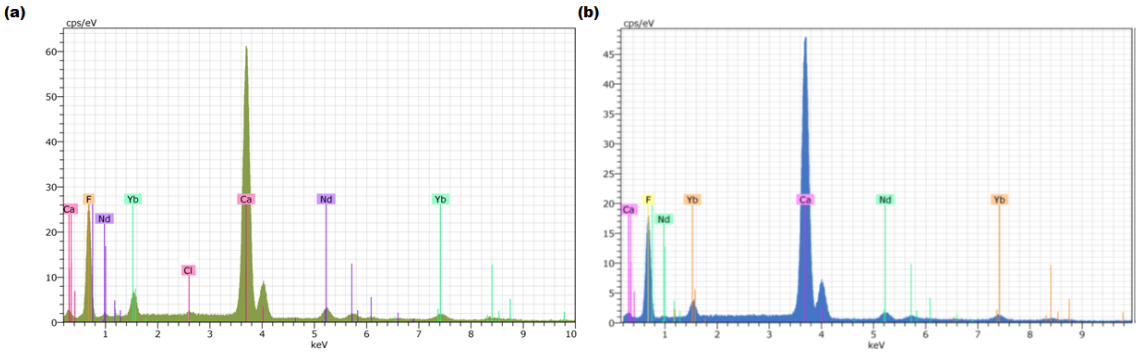

Figure 5.2: EDS spectra of (a) CaF_2:Nd/Yb and (b) CaF_2:Nd/Yb/Li phosphors synthesized by hydrothermal method.

5.5 FT-IR analysis

It is known that the reduction of quenching bonds, such as the O-H and N-O bonds, avoids non radiative transitions. A consequent increase in luminescence emission can be observed. FT-IR analysis was performed in order to investigate the variation of quenching groups

(with high-frequency vibrational modes) in the samples with and without Li. The FT-IR spectra of CaF_2:Nd4/Yb4 phosphors (black line) and CaF_2:Nd4/Yb4 with Li^+ phosphors (red line) are shown in Fig. 5.3. The FT-IR analysis reveals that Li^+ is able to reduce the number of quenching bonds in CaF_2:Nd4/Yb4 when it is introduced during the synthesis process. Ca-F absorption band is located around 448 cm^{-1} [64], while 2828 cm^{-1} is associated with C-H vibration modes [65]. Absorption water bands are around 1622 cm^{-1} and 3434 cm^{-1}, associated to O-H bonds of surface adsorbed water [59, 66]. These bands are reduced significantly when Li ions are introduced. Furthermore, bands around 1415 cm^{-1}, ascribed to stretching vibrations of N-O [64]. These two quenching bonds are reduced upon the Li^+ presence. Therefore, we can conclude that Li^+ ions avoid the entry of hydroxyl and other quenching groups [59]. Finally, the band at 2347 cm^{-1} is present due to KBr pellets used for recording FT-IR spectrum [48].

5.6 Luminescent analysis

The presence of Li^+ added to phosphors (2 mol/ %) does not affect the emission and excitation spectra (Fig. **??**fig:LuminLi]). However, the emission intensity is enhanced by approximately a factor of 5.

Thus, Li does not contribute to the energy transfer levels of CaF_2 phosphors. Li ions can compensate part of the local charge imbalance, which will help alleviate the generated lattice defects. This is consistent with the x-ray analysis discussed above, where Li ions incorporation affects both the crystal structure and the average crystal size. Li also avoids quenching groups, which promotes radiative transitions, as confirmed by FT-IR spectra. In general, all of the above is reflected by increased emission intensity.

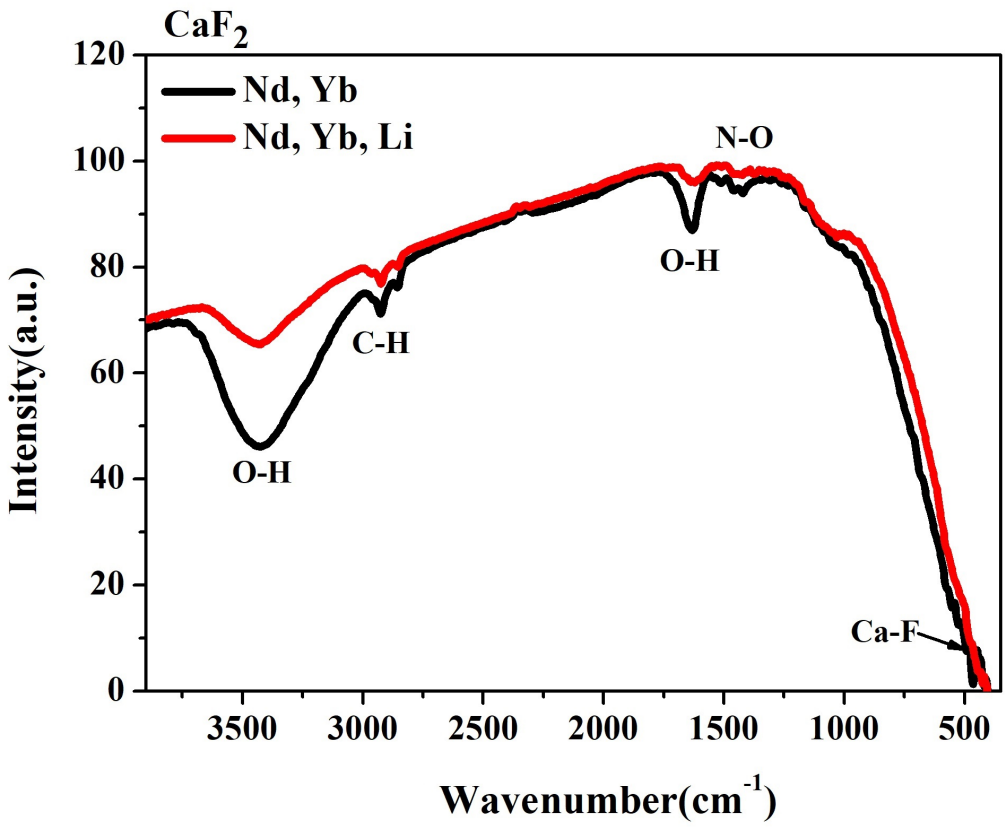

Figure 5.3: FT-IR spectrum of CaF_2:Nd4/Yb4 (black) and CaF_2:Nd4/Yb4/Li2 (red) phosphors, synthesized by hydrothermal method

5.7 Time Decay analysis

A time decay analysis was performed to understand the transfer energy mechanism and the possible role of Li as a phosphor. In the figure 5.5, semi-log plots of the normalized decay times for the Nd transition at 865 nm of the CaF_2:Nd4, CaF_2:Nd4/Yb4 and CaF_2:Nd4/Yb4/Li3 phosphors are shown.

Also, decay times measurements of CaF_2:Nd4/Yb4 and CaF_2:Nd4/Yb4/Li3 phosphors for Yb transition at 975 nm are shown.

All decay curves can be described by a double exponential decay time. No single exponential decay time is representative of the distribution of Yb^{3+} ions around Nd^{3+} ions

865	Samples	$\tau_1(\mu s)$	$\tau_2(\mu s)$	$\tau_{avg}(\mu s)$
	CaF_2:Nd4	646.51	14.26	612.80
	CaF_2:Nd4/Yb4	578.63	62.40	507.76
	CaF_2:Nd4/Yb4/Li2	646.77	25.19	622.24

Table 5.3: The fitted τ_1 and τ_2 values and the average lifetime τ at 865 nm for CaF_2:Nd4, CaF_2:Nd4/Yb4, CaF_2:Nd4/Yb4/Li2

975	Samples	$\tau_1(\mu s)$	$\tau_2(\mu s)$	$\tau_{avg}(\mu s)$
	CaF_2:Nd4/Yb4	500.02	14.26	612.80
	CaF_2:Nd4/Yb4/Li2	1011.73	466.75	812.62

Table 5.4: The fitted τ_1 and τ_2 values and the average lifetime τ at 975 nm for CaF_2:Nd4/Yb4, CaF_2:Nd4/Yb4/Li2

[67].

The following equation was used to determine an accurate average lifetime using a double exponential fitting:

$$I(t) = I_0 + A_1 e^{t/t_1} + A_2 e^{t/t_2} \tag{6}$$

where ***I(t)*** is the emission intensity at $\boldsymbol{t}$, I_0 is a constant related to the background, A_1 and A_2 are amplitude constants and τ_1 and τ_2, are the fast and slow lifetime components, respectively. Based on the following equation [68] it was determined that the average lifetime value of $< \tau >$ is as follows:

$$< \tau >= \frac{A_1\tau_1^2 + A_1\tau_1^2}{A_1\tau_1 + A_1\tau_1} \tag{7}$$

These data are showed in Tables 5.3 and 5.4

The average lifetimes of CaF_2:Nd4/Yb4 and CaF_2:Nd4/Yb4/Li2 phosphors were compared at 865 nm and 976 nm. There are longer average lifetimes observed for CaF_2:Nd4/Yb4/Li2, indicating the presence of additional radiative recombination pathways, which could be associated with the improvement of the crystallinity and the reduction of quenching groups.

The Burshtein Model [43, 69] was used in order to understand the transfer energy mechanism.

$$I(t) = I_0 \cdot exp(-\frac{t}{t_0} - \gamma_s t^{3/S} - w_m t) \tag{8}$$

where I_0 is the intensity at t=0, tau_0 is the average lifetime of Nd^3+ at 865 nm emission in absence of Yb^3+, γ_s is related with the direct energy transfer, w_s is the migration rate and $\boldsymbol{S}$, which can be take 6, 8 or 10 constant values depending on electric interaction, 6 for dipole-dipole (d-d), 8 for dipole-quadrupole (d-q) and 10 for quadrupole-quadrupole (q-q). In this case, the dipole-dipole electric interaction presented the best fit. The value found for the migration parameter w_s was negligible ($\approx 10^{-14} s^{-1}$) for phosphors with and without Li^+, discarding the donor-donor energy migration via diffusion or the hopping process [69], suggesting a direct donor-acceptor energy transfer. Through the Inokuti-Hirayama model, direct energy transfer can be calculated [43, 44]:

$$\gamma_s = \frac{4\pi}{3}\Gamma(1 - \frac{3}{S})N_A(\frac{R_0}{\tau_0^{1/S}})^3 \tag{9}$$

where N_A is the acceptor concentration and where R_0 is the critical transfer distance. Using the 4 mol % Yb concentration $N_A \approx 2.44x10^{20}$ ions/cm^3, values calculated for γ_s were 48.07 $s^{-1/2}$ for CaF_2:Nd4/Yb4 phosphors and 4.07 $s^{-1/2}$ adding to these Li (CaF_2:Nd4/Yb4/Li2). While for R_0 8.68 Å and 3.81 Å are critical distances for CaF_2:Nd4/Yb4 and CaF_2:Nd4/Yb4/Li2 phosphors, respectively. Therefore, the addition of Li results in a reduction in the critical distance between the sensitizer and the activator. These properties imply the formation of more Nd-Yb pairs, preventing quenching for Nd-Nd and Yb-Yb concentration, and promoting more radiative transitions, thereby increasing luminescence intensity, as shown in the Luminescence analysis section.

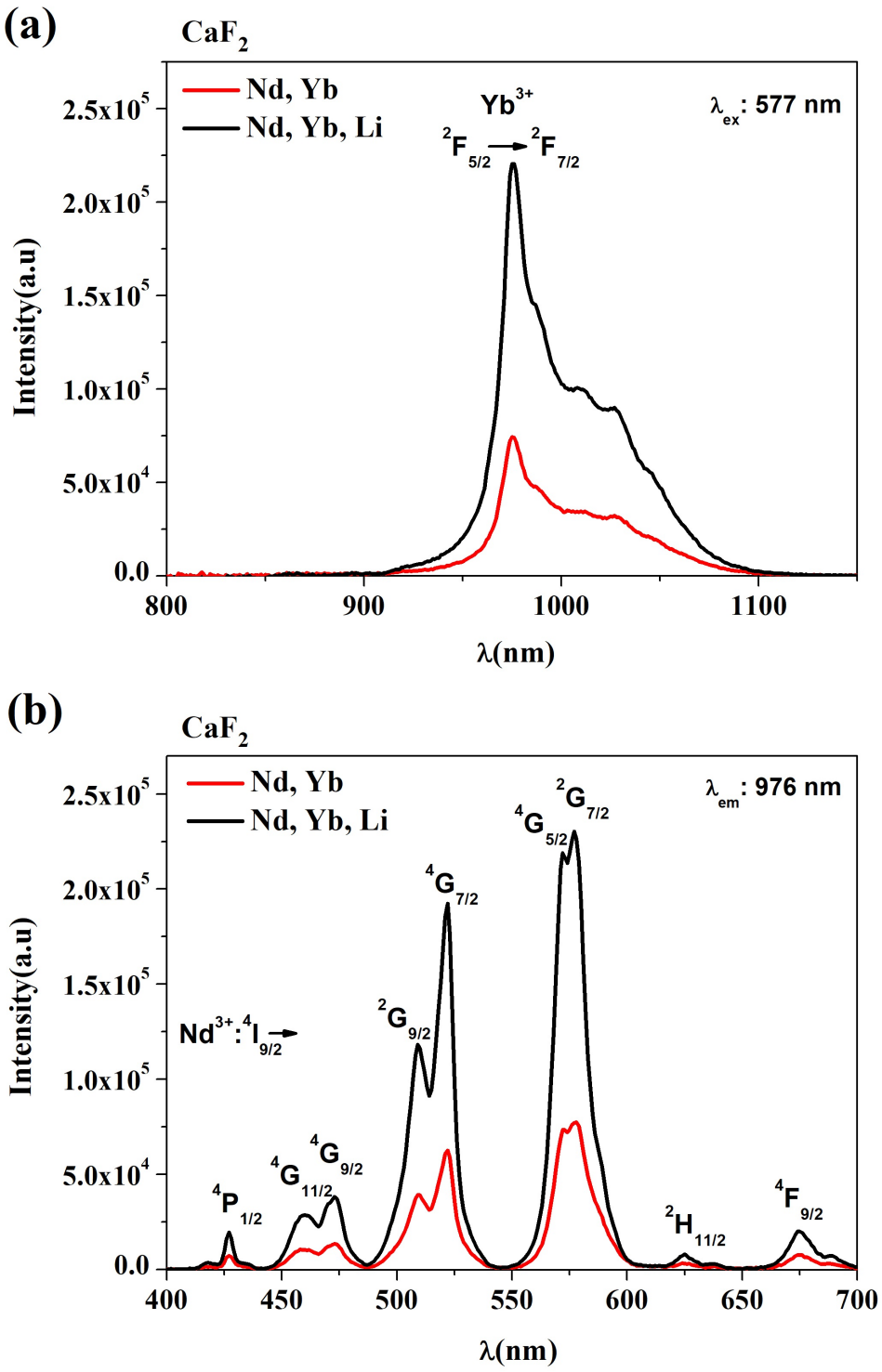

Figure 5.4: (a)CaF_2:Nd4/Yb4 (red line) and CaF_2:Nd4/Yb4/Li (black line) emission spectra upon excitation of Nd at 577 nm and (b) excitation spectra, monitoring the emission of Nd at 1062 nm.

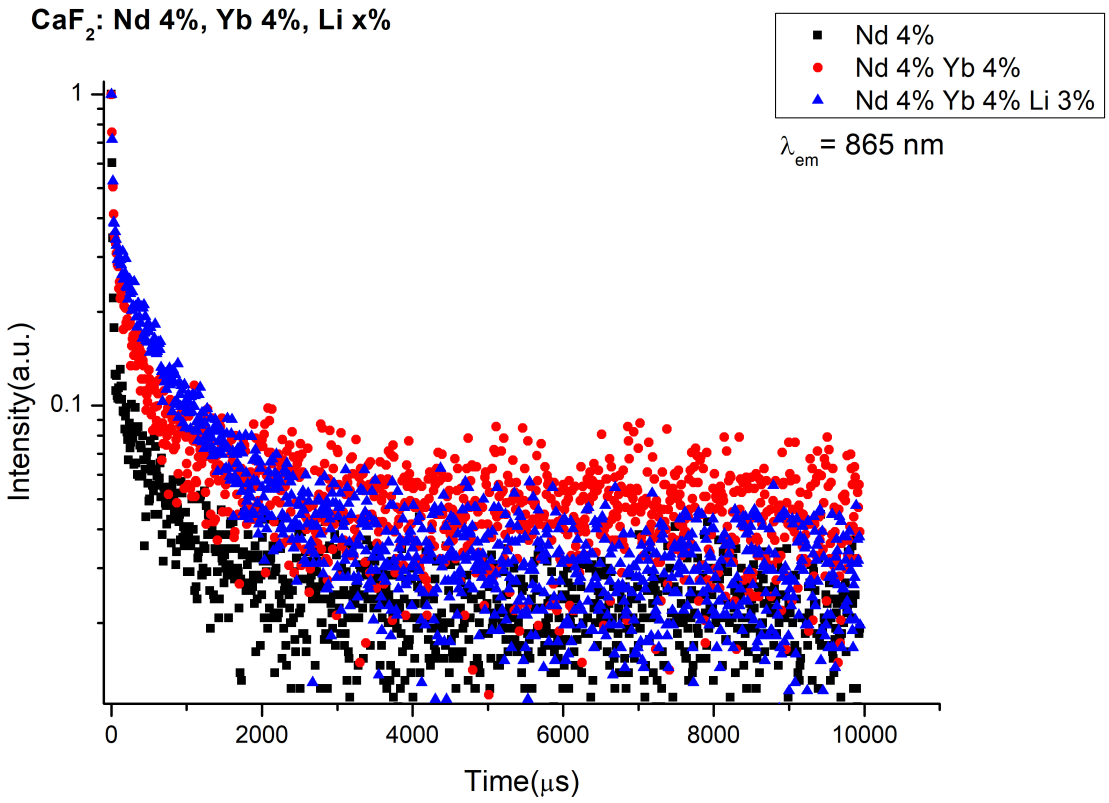

Figure 5.5: Decay times spectra of CaF_2:Nd4 (black squares), CaF_2:Nd4/Yb4 (red circles) and CaF_2:Nd4/Yb4/Li (blue triangles) emission spectra upon excitation of Nd at 353 nm and monitoring 865 nm.

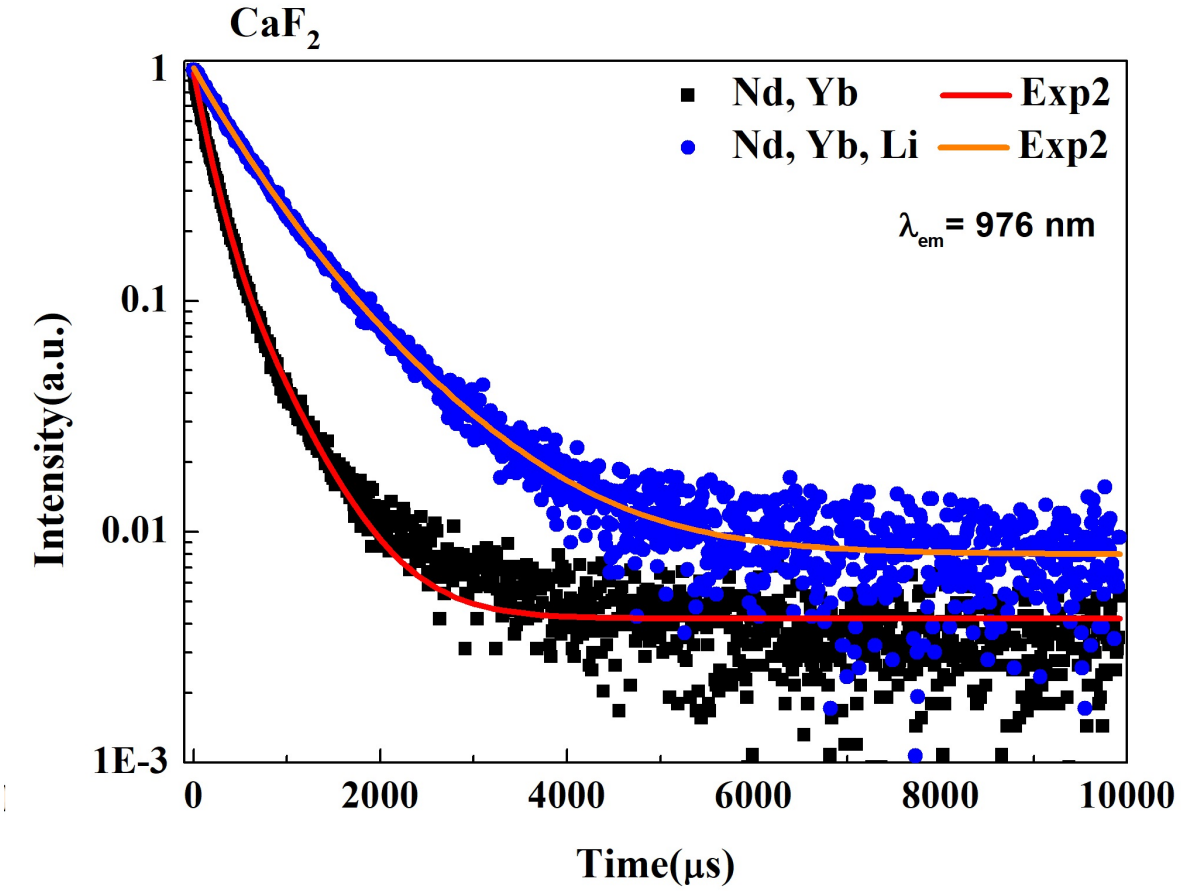

Figure 5.6: Decay times spectra of CaF_2:Nd4/Yb4 (black squares) and CaF_2:Nd4/Yb4/Li (blue circles) emission spectra upon excitation of Nd at 353 nm and monitoring 975 nm, Yb transition.

Chapter 6

Down-conversion in CaF_2:Nd/Yb/Li

A down-conversion process involves the absorption of one high energy photon and the emission of two low energy photons. Dexter proposed the idea in 1957, considering a mechanism in which energy is transferred from a donor to two acceptors, with each acceptor receiving half the energy from a donor who is excited. A quantum yield greater than unity was first observed in 1974 in a matrix doped with Pr^{3+} [70, 71], but not in the exact manner suggested by Dexter, but involving two sequential steps from $^1S_0$ level of Pr^3 to $^1I_6$, followed by relaxation to $^3P_0$ level and emission of a second visible photon from $^3P_0$. Quantum cutting via two sequential energy transfer steps was found for the first time through Gd^3-Eu^3 in a $LiGdF_4$ matrix in 1999 by Mijerink et al. [72].

DC process between Nd^{3+} and Yb^{3+} was confirmed for in 2010 by J. M. Meijer et al. [73] in a YF_3 matrix. The DC process confirmation was done through a comparison between the intensities of excitation spectra of Nd for the $^4F_{3/2} \rightarrow^4 I_{9/2}$ transition (at 865 nm) and of Yb for $^4F_{5/2} \rightarrow^4 F_{7/2}$ transition (at 975 nm).

As was shown in chapter 4, the introduction of Yb^{3+} in CaF_2:Nd4 phosphors allows the energy transfer between energy levels of Nd and Yb, increasing the intensity emission on NIR

under 353 nm (Nd^{3+} $^4D_3/2$ level) of excitation light. Further, UV light excitation causes a higher emission on NIR than visible light emission, which suggests a down-conversion process. Thus, a similar photoluminescence analysis to that performed by Meijer et al. has been conducted in order to demonstrate the existence of DC processes in these phosphors. First, it is necessary to describe the energy transfer between levels so that possible paths can be identified.

6.1 Energy Transfer path

The DC process for energy transfer from Nd to Yb is shown in figure 6.1. In the first step, Nd is excited through $^4D_{3/2}$ level (with 353 nm light), then it decays by non-radiative relaxation to the $^2G_{9/2}$ level. In this point, part of the energy is transferred to Yb via cross-relaxation $^2G_{9/2} \rightarrow ^4F_{3/2}$ to Yb $^2F_{5/2} \rightarrow ^2F_{7/2}$, which is followed by a second energy transfer step Nd^{3+}: $^4F_{3/2} \rightarrow ^4I_{9/2}$ (865 nm) to Yb^{3+}: $^2F_{7/2} \rightarrow ^2F_{5/2}$ (975 nm) populating $^2F_{5/2}$ level of Yb^{3+}.

Hence, if there is only one path, the quantity of emitted photons at 975 nm (Yb^{3+}: $^2F_{7/2} \rightarrow ^2F_{5/2}$) and at 865 nm ($Nd^{3+}$: $^4F_{3/2} \rightarrow ^4I_{9/2}$) under UV excitation light must be the same, before of populated $^2F_{5/2}$ level of Yb^{3+}.

6.2 Photoluminescence analysis

To confirm DC process, two emissions at 975 nm of Yb and at 865 nm of Nd were monitoring upon 353 nm excitation; Nd transition. It was necessary to normalize both emission spectra in relation to their 577 nm excitation peaks to obtain the correct proportion. The level of intensity was expected to be similar. Therefore, intensities normalized for three Yb concentrations (4, 5, 6 mol %) were integrated and are shown in the figure 6.2, a notable difference between 865 nm and 975 nm emission is noticed. These results indicate that there is another energy pathway from Nd to Yb.

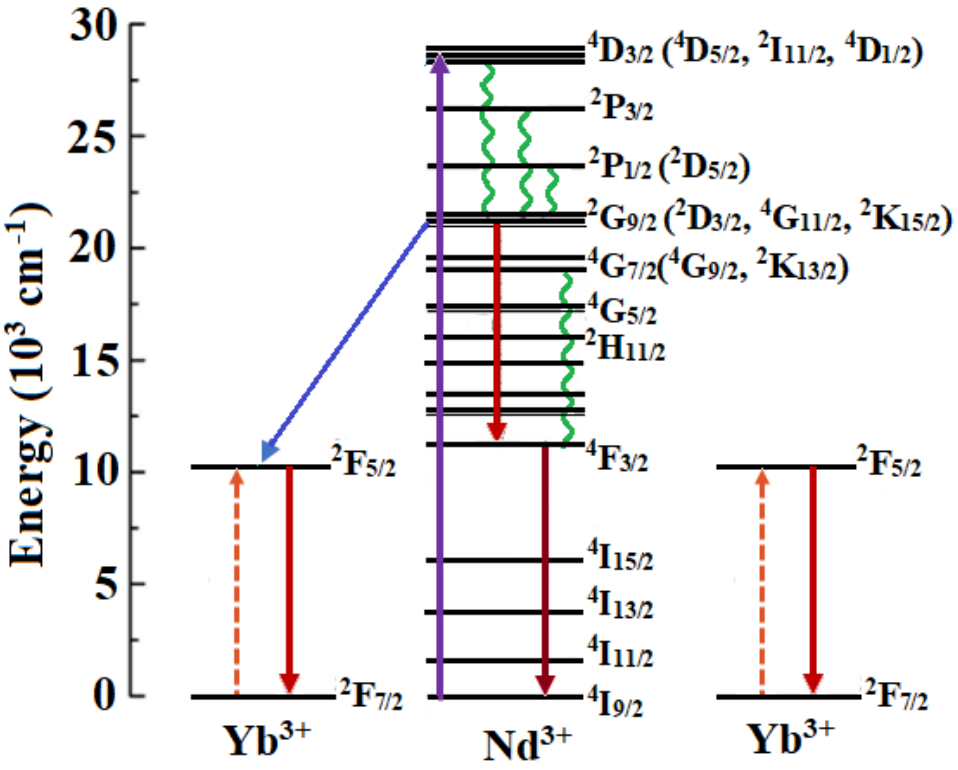

Figure 6.1: Energy levels of Nd^{3+} and Yb^{3+} ions and possible down-conversion mechanism between Nd^{3+} and Yb^{3+} in CaF_2:Li^+ matrix.

Table 6.1 summarizes the concentration variation ratio. Moreover, the ratio increases with an increase in Yb concentration. The reason is that major Yb quantities ensure Yb close neighbors for each Nd ion and ensure the distance required to have a successful transfer of energy between these ions. In this analysis, CaF_2:Nd4/Yb6/Li3 achieved the highest DC conversion efficiency.

The introduction of Li improves the luminescence intensity of CaF_2 phosphors doped with Nd and Yb as explained in the above section. In order to determine whether Li plays any role in the DC process, an analysis of the integrated intensities ratio between Nd (865 nm) and Yb (975 nm) transitions was also conducted on CaF_2:Nd4/Yb4/Li3 phosphors. Comparison between CaF_2:Nd4/Yb4 and CaF_2:Nd4/Yb4/Li3 intensities are shown in the figure 6.2 and ratios are described in the table 6.1. There is a slight variation in the ratios.

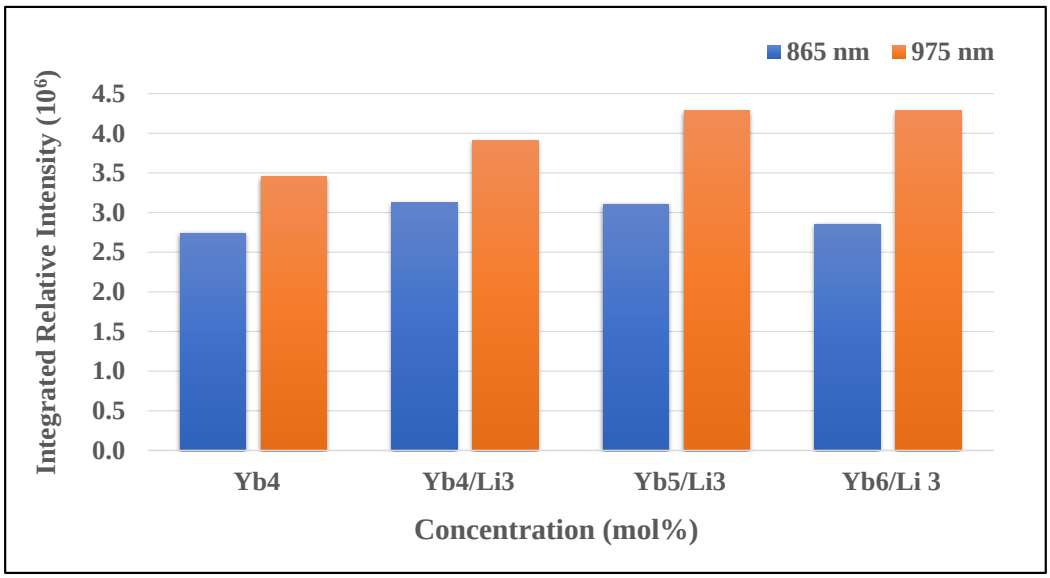

Figure 6.2: Comparison of 353 nm integrated excitation intensities of CaF_2:Nd4/Yb4 and CaF_2:Nd4/Li3 with 4, 5, 6 mol % of Yb phosphors monitoring $^4F_{3/2} \rightarrow ^4I_{9/2}$transition (865 nm) of Nd^{3+} and $^2F_{5/2} \rightarrow ^2F_{7/2}$ transition (975 nm) of Yb^{3+}. The excitation spectra were normalized at 577 nm ($^4G_{5/2}$) peak.

This ratio has a value of 1.25 for CaF_2:Nd4/Yb4 and a value of 1.26 for CaF_2:Nd4/Yb4/Li3. In this regard, Li does not play a direct role in DC.

To analyzed the Yb role in the DC process, different Yb concentrations, were carried out. Three different concentrations, 4, 5, 6 mol % of Yb were added to CaF_2:Nd4/Li3, obtaining the best luminescent intensity for Yb 5 mol % sample, as shown figure 6.3

The sample with the best luminescent characteristics CaF_2:Nd4/Yb5/Li3 does not match that with the highest DC efficiency, CaF_2:Nd4/Yb6/Li3. It may be due to ex-

Sample	Ratio
CaF_2:Nd4/Yb4	1.25
CaF_2:Nd4/Yb4/Li3	1.26
CaF_2:Nd4/Yb5/Li3	1.38
CaF_2:Nd4/Yb6/Li3	1.50

Table 6.1: Ratio between normalized intensities of Nd at 865 nm and Yb at 975 nm for CaF_2:Nd4/Yb4, CaF_2:Nd4/Yb4/Li3, CaF_2:Nd4/Yb5/Li3, CaF_2:Nd4/Yb6/Li3

cess Yb which causes quenching by concentration, which is reflected in a reduction in luminescence intensity 6.3.

6.3 Luminescence effective quantum yield

Measurement of the external (effective) quantum yield (QY_{eff}) was done using an integrating sphere. It was determined from the ratio of the number of photons emitted to the number of photons absorbed by the sample. The number of photons emitted is represented by the area under the spectrally corrected emission peak for a sample: A_{em}. The number of photons absorbed is determined by the difference between the Rayleigh scattering peak areas of a reference sample and a study sample: $A_{scatref} - A_{scatsample}$. When two different detectors are used to measure scattering spikes and the emission spectrum of a sample, differences in sensitivity should also be considered, and the equation can be written as follows:

$$Q_{eff} = \frac{A_{em}}{(A_{scatref} - A_{scatsample})k_{Red-PMT/NIR-PMT}} \quad (1)$$

Where $k_{Red-PMT/NIR-PMT}$ is the ratio between sensitivities of the two detectors. In the present study, a neutral density filter was placed in front of the path of excitation light. In order to determine the ratio of sensitivity between the two detectors, a known signal in the 750 to 800 nm range was measured with both detectors. The measurement for the

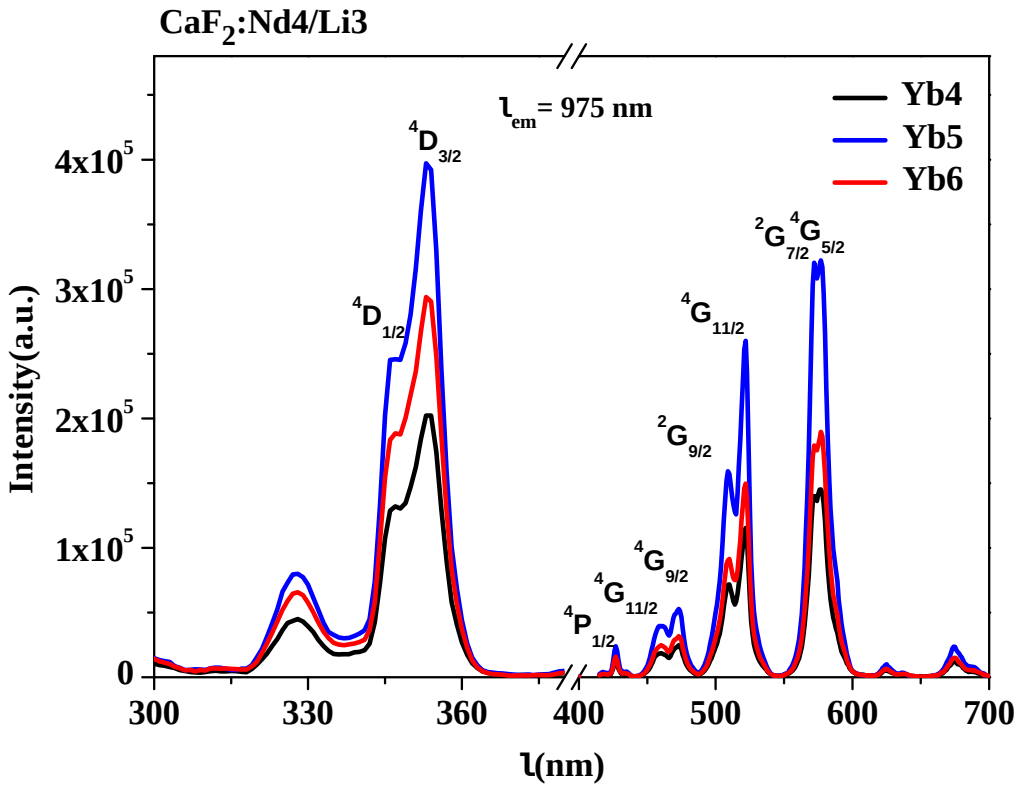

Figure 6.3: Excitation spectra of CaF_2:Nd4/Li3 phosphors with 4, 5, 6 mol % Yb monitoring $^2F_{5/2} \rightarrow ^2F_{7/2}$ transition of Yb^{3+} at 975 nm.

sample with the highest photoluminescence signal (CaF_2:Nd4/Yb5/Li3) was 81±10 % for UV (353 nm) and 37±5 % for visible (577nm) excitation. Considering that the 577nm is associated with downshifting processes (one to one photon process), the measurement is lower than that of the 353nm (about half as much when considering the experimental error bars). Therefore, results confirm the existence of DC processes upon UV excitation (353 nm) in CaF_2:Nd/Yb/Li phosphors.

Conclusion

Nd^{3+} and Yb^{3+} codoped CaF_2 phosphors, synthezised by either coprecipitation or hydrothermal method, show a photoluminescence emission dominated by NIR, Yb emission at 975 nm under UV (at 353 nm) and Vis (at 577 nm) light excitation The excitation spectra for the Yb^3+ emission at 975 nm, is associated in general to interelectronic energy level of Nd^3+, which indicate a energy transfer process from the excited Nd^3+ ions to the Yb^3+ ions. Because of the high temperatures and pressures in HT synthesis, these phosphors exhibit better structural and optical characteristics than CP.

Li^+ incorporation in CaF_2:Nd/Yb phosphors has a positive impact on their structural and luminescent properties. This is because Li ions act as charge compensators. Li^+ ions also reduce hydroxyl and other high vibrational groups that act as non-radiative channels. Furthermore, promote the formation of Nd-Yb pairs within the host. Consequently, the intensity of emission and crystallinity are improving. The NIR emission intensity increased 3.75 fold when comparing CaF_2:Nd/Yb/Li to CaF_2:Nd/Yb phosphors.

Downconversion (DC) processes were confirmed in CaF_2:Nd/Yb/Li phosphors upon Ultraviolet excitation (at 353 nm). In the DC process, energy is transferred from the Nd energy level excited at 353 nm to Yb energy level through two path. First, the material absorbs UV photons, which decay nonradiative to the intermediate Nd^3+ level (474 nm); at this point, the photons can go directly to the Yb^3+ transition, and then the other part of the energy is transferred via cross-relaxation to a level closer to Yb^3+ so that it can decay radiatively. Values up to 150% of DC efficiency were determined in the photoluminescence

excitation-emission spectra. For CaF_2:Nd/Yb/Li phosphors, synthesized by HT method, the optimal nominal concentrations of dopants are Yb 5 mol%, Nd 4 mol%, and Li 3 mol%. Higher Yb concentrations of up to 5 mol% result in a higher DC efficiency. Nevertheless, the luminescent intensity decreases because of quenching Yb concentrations. On optimal phosphors, values of 81±10 and 37±15 were obtained from UV (at 353 nm) and Vis (at 577 nm) excitation to NIR (975 nm) emission for effective quantum yield measurements. Therefore, the spectral conversion capability exhibited by these phosphors could improve Si solar cell efficiency.

Future work and perspectives

The following are some perspectives and future work related to this work:

- Create CaF_2:Nd/Yb/Li phosphors films to be use Silicon solar cells for improve their efficiency.
  - Embedding CaF_2:Nd/Yb/Li phosphors in polymers.
  - Embedding CaF_2:Nd/Yb/Li phosphors in SiO_2.
- Organic ligands could be paired with CaF_2:Nd/Yb/Li phosphors to improve their NIR emission.
- Incorporation of CaF_2:Nd/Yb/Li phosphors in organic and inorganic matrix for future energy harvesting applications.

Ceramics International 47 (2021) 4694–4701

Contents lists available at ScienceDirect

Ceramics International

journal homepage: www.elsevier.com/locate/ceramint

The effect of Li^+ incorporation in Yb^{3+}-Nd^{3+} co-doped CaF_2 phosphors over the NIR photoluminescence emission excited under visible light

J. De Anda [a,*], E.F. Huerta [b], J.U. Balderas [c], G.C. Righini [d], C. Falcony [c]

[a] Centro de Investigación y Estudios Avanzados del IPN, Programa de Doctorado en Nanociencias y Nanotecnología, Av. IPN 2508, CDMX, México, 07360, Mexico
[b] Universidad Autónoma Metropolitana-Iztapalapa, Departamento de Física, P.O. Box 55-534, CDMX, México, 09340, Mexico
[c] Centro de Investigación y Estudios Avanzados del IPN, Departamento de Física, Av. IPN 2508, CDMX, México, 07360, Mexico
[d] Nello Carrara Institute of Applied Physics (IFAC CNR), Via Madonna del Piano 10, 50019, Sesto Fiorentino, Firenze, Italy

ARTICLE INFO

Keywords:
Lanthanide-based phosphors
Li^+ incorporation effect
NIR emission
Luminescence enhancement

ABSTRACT

The structural and optical characteristics of Nd^{3+}-Yb^{3+} doped CaF_2 phosphors with and without the addition of Li^+ ions are described in this work. The phosphors synthetized by hydrothermal and co-precipitation methods showed near-infrared (NIR) luminescence emission associated with inter-electronic transition of the Yb^{3+} ion in the range of 900–1050 nm via energy transfer process from Nd^{3+} ions under visible light excitation. The addition of Li^+ to these phosphors resulted in an improvement of the NIR luminescence intensity by a factor up to 5. The effect of the incorporation of Li^+ ions into the CaF_2 crystallite structure, the reduction of luminescence quenching states, as well as the energy transfer mechanism involved are discussed.

1. Introduction

Internet of things (IoT) connects billions of devices to the internet, collecting and sharing information to make life easier. Although IoT are expected to be low-power devices, the analysts of International Data Corporation (IDC) predict a total of 41.6 billion of devices connected by 2025 [1], which means a strong growth in the energy consumption. Photovoltaic (PV) conversion of indoor illumination visible light could help to face this challenge. However, most commercially available PV cells have a large spectral mismatch that limits their efficiency with today's indoor illumination. This weakness, that limits the indoor use of PV devices, could be overcome by the development of downshifting materials designed to harvest visible light and convert it to NIR emission (up to 1127 nm), where the performance and efficiency could be better for specific types of PV cells, such as crystalline silicon (c-Si) cells.

Lanthanides-based phosphors and films have been proposed as good candidates to enhance photovoltaic cells efficiency through frequency conversion processes [2–5], because of their multiple intra-band transitions ($4f^n$-$4f^n$) with different energy levels and long stokes shift [6] that absorb and emit in a wide variety of wavelength lines. Besides, lanthanides optical spectra are not modified when they are introduced into most of wide bandgap host materials, because 4f electrons are partially filled and well shielded from immediate $5s^2$ and $5p^2$ orbitals. The introduction of multiple lanthanides elements, carefully chosen, in a host allows to generate an efficient spectral conversion from ultraviolet and/or visible to the infrared region. Trivalent neodymium ions have electronic energy levels with absorption bands ranging from the UV to the NIR spectral region, while ytterbium has a unique energy level that emits in the NIR region (900–1100 nm) that can be absorbed by c-Si and other materials used in PV technology [7]. Co-doping of Nd^{3+} and Yb^{3+}, as sensitizer and emitter, respectively, has been investigated in different host lattices, showing an efficient energy transfer among them and a strong near-infrared emission [8–16]. On the other hand, the most common materials used as host for lanthanide-based phosphors are metal oxides [17,18] and fluorides [9,19–21]. In particular, CaF_2 has been used as host [22–25] in phosphor materials because of its chemical stability, low phonon energy, and optical transparency over a large range of wavelengths, from the UV to Visible and NIR [12,17–24]. Nevertheless, when trivalent ions are introduced in a CaF_2 host lattice, replacing Ca^{2+} ions, lattice defects (mainly Ca-vacancies) are formed to maintain charge neutrality in the system, inducing localized energy states that degrade the luminescence performance of the phosphor. To solve this problem, alkali ions, such as Na^+, K^+ and Li^+ ions, have been incorporated, as charge compensators, improving the luminescent properties of these phosphors [26–28]. Although, depending on the specific case, some of these alkali ions might not work as expected,

* Corresponding author.
E-mail address: jessica.deanda@cinvestav.mx (J. De Anda).

https://doi.org/10.1016/j.ceramint.2020.10.037
Received 21 July 2020; Accepted 8 October 2020
Available online 9 October 2020

Gupta et al. [29], for instance, reported an emission enhancement of $SrWO_4:Eu^{3+}$ phosphors with the incorporation of Li^+ ions, but not for Na^+ and K^+ ions. Other authors have also reported an enhanced emission due to the Li^+ ions incorporation in different lanthanide based phosphors, attributing this phenomenon to changes in the crystal structure and a crystallite size increment [11,30,31]. In this work, the effect of Li^+ incorporation in Yb^{3+} and Nd^{3+} co-doped CaF_2 phosphors on the NIR luminescence emission is reported. Moreover, the possible role that Li^+ plays in the Nd^{3+} to Yb^{3+} energy transfer mechanism and its effect on the structural characteristics of the phosphor are discussed.

2. Materials and methods

2.1. Materials

$CaCl_2{\cdot}H_2O$ (99.0%), $NdCl_3\cdot 6H_2O$ (99.9%), $YbCl_3{\cdot}6H_2O$ (99.9%), LiCl (99.0%) and NH_4F (98.0%) were purchased from Sigma-Aldrich and used without further purification.

2.2. Synthesis of the $CaF_2:Nd^{3}$, Yb^{3+}, Li^+ nanostructured phosphors

CaF_2 doped with 4 mol% Nd^{3+} (denoted as CaF_2:Nd), co-doped with 4 mol% Nd^{3+} + 4 mol% Yb^{3+} (denoted as CaF_2:Nd,Yb) and co-doped with 4 mol% Nd^{3+} + 4 mol% Yb^{3+} + 2 mol% of Li^+ (denoted as CaF_2:Nd,Yb,Li) phosphors were synthesized by co-precipitation and hydrothermal methods. Stoichiometric amounts of $CaCl_2$, $YbCl_3$, $NdCl_3$, and LiCl were dissolved on 10 mL of deionized water for 10 min to form a chloride salts solution (1 M). Then, a 15 mL aqueous solution (1 M) containing NH_4F was added to chloride solution.

2.2.1. Co-precipitation synthesis

For co-precipitation (CP) synthesis, the solution was thoroughly mixed in a magnetic stirrer for 1 h at room temperature in ambient atmosphere to transform the transparent reaction into opaque white suspension. The suspension was washed, at least two times, with deionized water to remove any possible remnants and centrifuged (5000 rpm, 10 min). After this process, it was dried in vacuum at 60 °C for 12 h. The phosphors were gradually annealed, starting at 200 °C for 30 min, then at 400 °C for 30 min, and finally 600 °C for 1 h in air to improve their structural quality.

2.2.2. Hydrothermal synthesis

For hydrothermal (HT) synthesis, the solution was thoroughly mixed in a magnetic stirrer for 10 min at room temperature in ambient atmosphere. Then, the solution was transferred to a 120 mL Teflon-lined autoclave and heated for 8 h at 170 °C. The autoclave was left to cool down to room temperature. Finally, the phosphors were washed, dried, and annealed using the same procedure as for the CP method.

2.3. Instruments and measurements

XRD measurements were performed by Siemens D-500 diffractometer with CuKα (α = 1.54 Å), to know the crystalline structure. The photoluminescence characteristics were obtained using an Edinburgh Instruments 980S spectrophotometer. FT-IR spectroscopy was made using a 6700 FT-IR NICOLET Equipment. All measurements were carried out at room temperature.

3. Results and discussion

3.1. X-ray diffraction analysis

XRD diffractograms for CaF_2:Nd, Yb and CaF_2:Nd,Yb,Li, synthesized by either co-precipitation (CP) or hydrothermal (HT) method, are shown in Figs. 1 and 2, respectively. All observed diffraction peaks correspond to the CaF_2 cubic phase (standard PDF card #95-500-0223), suggesting that RE^{3+} and Li^+ ions incorporation as dopants do not change the cubic phase of CaF_2. However, there is a slight shift of the peaks with lanthanides incorporation in the host matrix, and a partial recovery when Li^+ ions are added. The incorporated RE^{3+}, as they substitute the Ca^{2+} ions in the CaF_2 matrix, generate lattice defects, mainly Ca vacancies, as a mechanism for preserving charge neutrality. This charge compensation can be explained by the following defect reactions [32]:

$$2Nd \xrightarrow{3CaF_2} 2Nd^{\bullet}_{Ca} + V''_{Ca} \quad (1)$$

$$2Yb \xrightarrow{3CaF_2} 2Yb^{\bullet}_{Ca} + V''_{Ca} \quad (2)$$

$$Nd + Yb \xrightarrow{3CaF_2} Nd^{\bullet}_{Ca} + Yb^{\bullet}_{Ca} + V''_{Ca} \quad (3)$$

where $Nd^{\bullet}_{Ca}$ and $Yb^{\bullet}_{Ca}$ indicate a substituted Ca ion by RE (Nd or Yb) ion, while V''_{Ca} represents Ca vacancies.

The excess of positive charges is regularly compensated by interstitial fluorine ions around the Ca vacancy. Therefore, the increase of Nd^{3+} or Yb^{3+} concentration requires more F^- ions to neutralize the charge, producing a strong charge repulsion between F^- ions, increasing both the lattice constant [12] and disorder extent, reflected on the observed shift of the peaks towards lower angles and an increment of their full width at half-maximum (FWHM) [22].

Addition of Li^+ ions to the RE^{3+} ions helps the charge compensation process as described by the following equations:

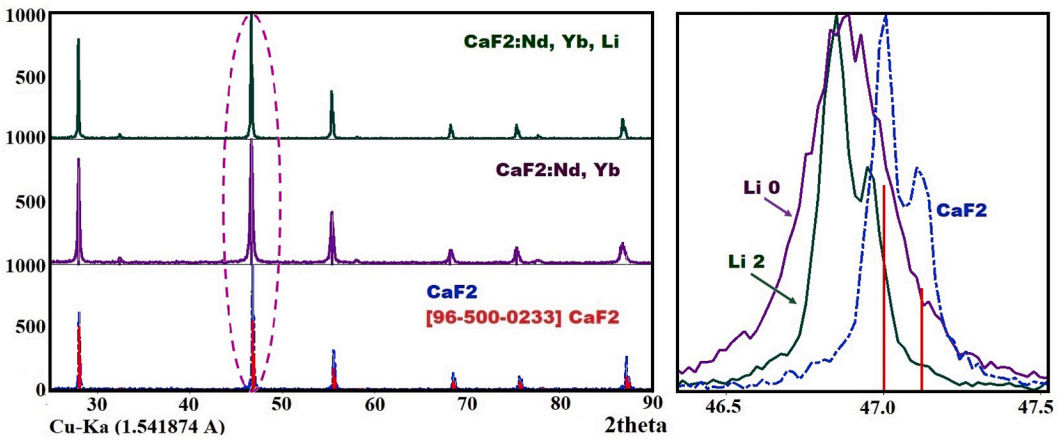

Fig. 1. (a) XRD diffractogram of host CaF_2 (blue), CaF_2:Nd, Yb (purple) and CaF_2:Nd,Yb, Li (green) by co-precipitation (CP) method and (b) local magnification for the dominant peak. (For interpretation of the references to colour in this figure legend, the reader is referred to the Web version of this article.)

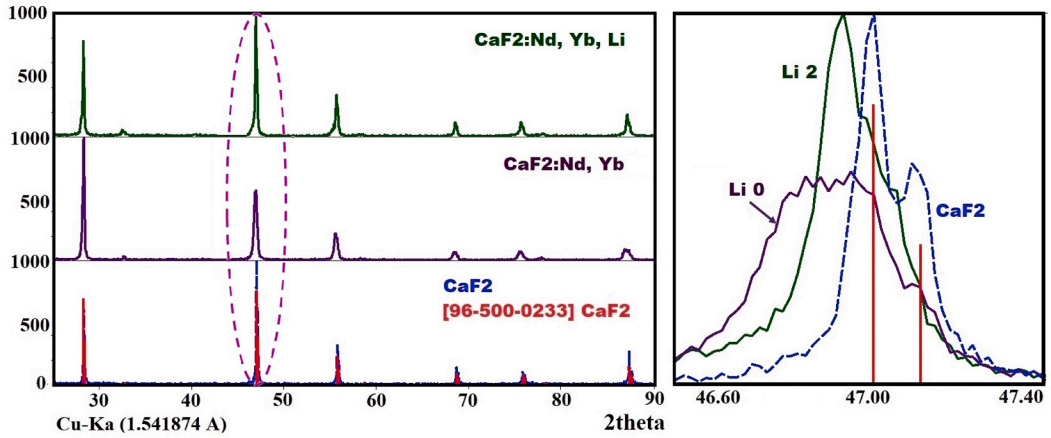

Fig. 2. (a) XRD diffractogram of host CaF_2 (blue), CaF_2:Nd, Yb (purple) and CaF_2:Nd,Yb, Li (green) by hydrothermal (HT) method and (b) local magnification for the dominant peak. (For interpretation of the references to colour in this figure legend, the reader is referred to the Web version of this article.)

$$Nd + Li \xrightarrow{3CaF_2} Nd^{\bullet}_{Ca} Li^{'}_{Ca} \quad (4)$$

$$Yb + Li \xrightarrow{3CaF_2} Yb^{\bullet}_{Ca} Li^{'}_{Ca} \quad (5)$$

Li^+ ions occupying interstitial sites result in the expansion of host lattice [33], whereas location of the alkaline ions in substitutional sites would lead a shrink in the host lattice [11]. It is suggested that interstitial CaF_2:Nd, Yb sites occupied by F^- are reduced by the introduction of the Li^+ ions at some of the Ca^{2+} vacancies. The new RE^{3+} - Li^+ pair at neighboring lattice sites replaces two Ca^{2+} ions, partially reducing the lattice distortion, which in turn decreases the peaks shift in the XRD diffractograms, as depicted in the local magnification shown in Fig. 1 (b) and 2 (b). Moreover, narrowed FWHMs are observed when Li^+ ions are introduced, indicating an improvement in the crystallinity of the material (along with an increase of the crystallite size) [32] (Table 1). The crystallite size (D) was calculated using the well know Scherrer's equation:

$$D = \frac{K\lambda}{\beta cos\theta} \quad (6)$$

where K is a constant, with a value of 1 for the cubic CaF_2 [34], λ is the wavelength of Cu-Kα radiation (0.15406 nm), β the full width at half maximum (FWHM) and θ the Bragg's diffraction angle. Table 1 lists the calculated crystallite sizes for the samples studied.

In general, the crystallite size is larger for the samples synthesized by CP method compared to those obtained by HT method. It is known that CP synthesis can involve rapid particle formation and agglomeration process which affect the size and properties of the products [35]. Hence, the larger crystallite size of the CP samples compared to HT samples could indicate lower agglomeration of particles during the HT synthesis [36]. Moreover, Fig. 3 shows that the peak shifting is lower for the HT sample compared with CP sample, which suggests a higher crystallinity structure for the HT synthesized phosphors. This could be due to the high-temperature and high-pressure reaction conditions in HT synthesis that usually produce nanomaterials with higher crystallinity compared with nanomaterials synthesized at "low-temperatures" by CP methods

Table 1
Crystalline size of CaF_2:Nd, Yb and CaF_2:Nd,Yb, Li synthesized by co-precipitation and Hydrothermal methods.

Samples	Crystallite size (nm)
CaF_2:Nd, Yb (CP)	35
CaF_2:Nd,Yb, Li (CP)	75
CaF_2:Nd, Yb (HT)	25
CaF_2:Nd,Yb, Li (HT)	55

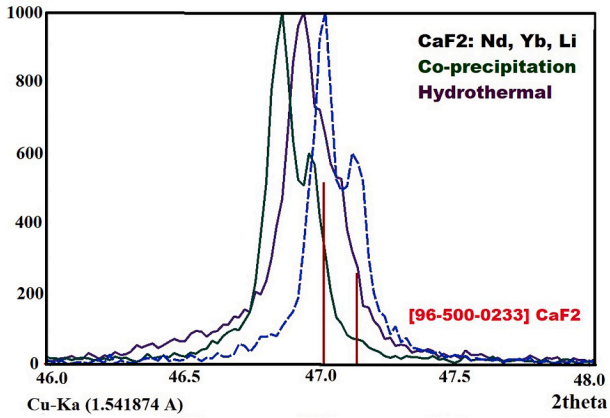

Fig. 3. XRD diffractogram of co-doped CaF_2:Nd,Yb, Li by hydrothermal (purple) and co-precipitation (green) method. (For interpretation of the references to colour in this figure legend, the reader is referred to the Web version of this article.)

[37,38]. Further, the increase of the crystallite size by more than two times and the reduction of the shifting peaks when Li^+ ions are introduced, for both synthesis methods, suggest an improved crystallinity of the co-doped CaF_2:Nd, Yb phosphors.

3.2. FT-IR analysis

FT-IR transmittance spectra for the CaF_2:Nd, Yb and CaF_2:Nd,Yb, Li phosphors are shown in Fig. 4 for hydrothermal synthesized samples (similar behavior is displayed by the CP samples). The absorption band around at 448 cm^{-1} is assigned to Ca–F bonds [34], while the band at 2928 cm^{-1} is associated with C–H vibration modes [39]. Water bands at 1622 cm^{-1} and around 3424 cm^{-1} are assigned with O–H bonds of surface adsorbed water [30,40]. It can be noted that bands of O–H bonds are significatively reduced upon Li^+ incorporation. Additionally, the bands around 1415 cm^{-1} related to stretching vibrations of N–O [34], are also suppressed in presence of Li^+, reflecting the fact that Li^+ ions neutralize hydroxyl and other groups that are introduced during the phosphors synthesis [30]. Finally, the band at 2347 cm^{-1} is present due to KBr pellets used for recording the FT-IR spectrum [36].

3.3. Photoluminescence analysis

The excitation and emission luminescence spectral response of the

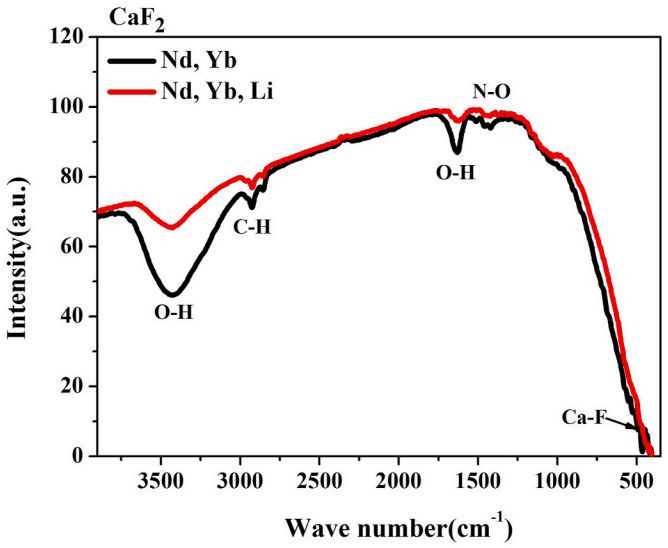

Fig. 4. FT-IR spectrum of CaF_2:Nd, Yb (black) and CaF_2:Nd,Yb, Li (red) phosphors, synthetized by hydrothermal method. (For interpretation of the references to colour in this figure legend, the reader is referred to the Web version of this article.)

phosphors synthesized by both CP and HT methods showed similar features, the differences being limited to the intensity variation associated with differences in the structural characteristics described in the previous sections and with the luminescence enhancement induced by the incorporation of the Li^+ ions (a factor of 2 or 5). Therefore, from this point on, the data presented, unless otherwise indicated, will be for phosphors synthetized by the hydrothermal method.

The emission spectra of CaF_2:Nd, under 577 nm excitation (see Fig. 5 (a)) is composed by two peaks corresponding to the $^4F_{3/2} \rightarrow {}^4I_{9/2}$ and $^4F_{3/2} \rightarrow {}^4I_{11/2}$ radiative transitions of Nd^{3+} doped sample. When Yb^{3+} ions are incorporated, the $^2F_{5/2} \rightarrow {}^2F_{7/2}$ radiative transition (peaked at 976 nm) prevails over the Nd^{3+} ion emissions, evidencing the energy transfer (ET) process from Nd^{3+} to Yb^{3+}ions. Some of the tail-like emissions observed at wavelengths longer than 976 nm could be due to the random distributions of Yb^{3+} ions around Nd^{3+} ions [15,16] and/or multiple energy transfer processes from Yb^{3+} to other Yb^{3+} ions [16].

Fig. 5 (b) shows the luminescence excitation spectra for the CaF_2:Nd and CaF_2:Nd, Yb phosphors monitoring 1062 nm and 976 nm emissions wavelength, respectively. The spectra of Nd^{3+} doped phosphors were amplified by a factor of 15 for comparison and clarity purposes. Both excitation spectra (recorded from 400 to 700 nm) show the same peaks, confirming the energy transfer (ET) mechanism from Nd^{3+} to the Yb^{3+} ions in the CaF_2:Nd, Yb system. The aforementioned excitation peaks are centered around 426, 460, 474, 508, 522, 572, 577, 624 and 674 nm, corresponding to the Nd^{3+} transitions from the $^4I_{9/2}$ ground state to the $^2P_{1/2}$, $^4G_{11/2}$, $^2G_{9/2}$, $^4G_{9/2}$, $^4G_{7/2}$, $^2G_{7/2}$, $^4G_{5/2}$, $^2H_{11/2}$ and $^4F_{9/2}$ excited states of this ion, respectively. The most intense excitation peak is centered at 577 nm, which corresponds to the Nd^{3+} $^4I_{9/2} \rightarrow {}^4G_{5/2}$ transition; thus, a multi-phonon relaxation mechanism is proposed to occur from the Nd^{3+} $^4G_{5/2}$ to $^4F_{3/2}$ state, followed by an ET process to the Yb^{3+} ion to the $^2F_{5/2}$ followed by a $^2F_{5/2} \rightarrow {}^2F_{7/2}$ radiative transition at 976 nm. This recombination path has been suggested to be the most likely to occur in Nd^{3+}- Yb^{3+} doped phosphors [13].

The addition of Li^+ ions (2%) to the Nd^{3+}- Yb^{3+} co-doped phosphors does not change neither emission nor excitation spectra characteristics, but it does enhance the emission intensity by a factor of 5 (a factor of 2 for the CP synthetized phosphors), as it is depicted in Fig. 6. It has been reported that phosphors in which trivalent lanthanide ions substitute divalent ions in the host matrix exhibit many lattice defects and the

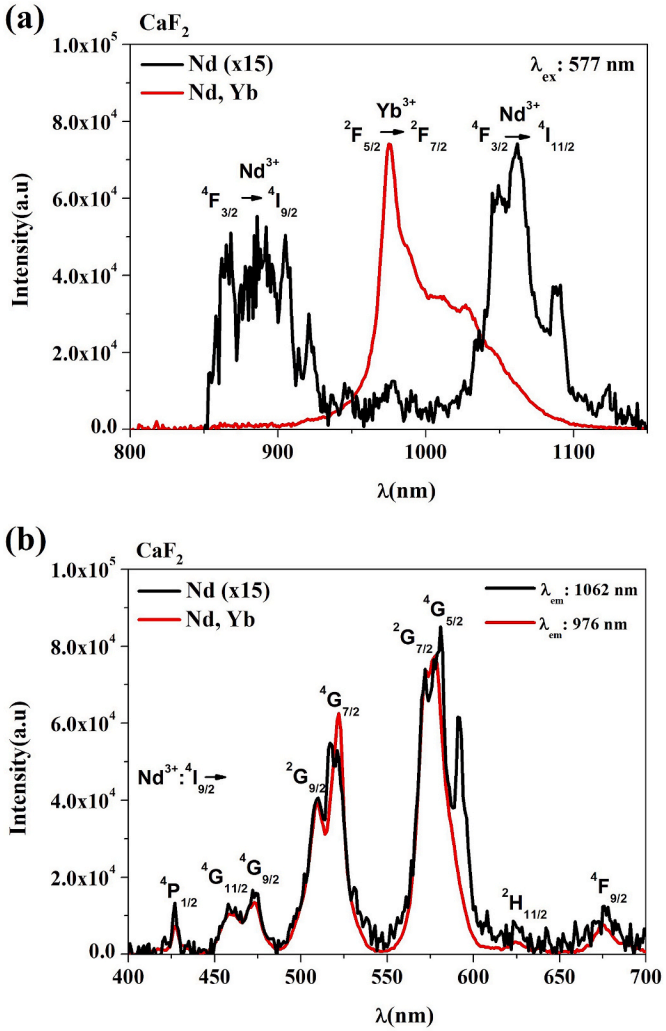

Fig. 5. (a) Emission spectra upon the excitation of Nd^{3+} at 577 nm and (b) excitation spectra, monitoring the emission of Nd^{3+} at 1062 nm for the CaF_2:Nd (black line) and Yb^{3+} at 976 nm for CaF_2:Nd, Yb (red line). (For interpretation of the references to colour in this figure legend, the reader is referred to the Web version of this article.)

formation of Ln^{3+} clusters to balance the local charge in the host [41]. The role that Li^+ ions play in these materials is to provide alternative mechanisms to compensate the local charge unbalance and thus alleviate the generated lattice defects, which is consistent with the above discussed x-rays analysis where Li^+ ions incorporation is found to induce changes on the crystal structure and on the average crystallite size.

3.4. Time decay analysis

To assess the energy transfer mechanisms from Nd^{3+} to Yb^{3+}ions, the time decay behavior of the luminescence emission was studied. Semi-log plots of the normalized decay times for Nd^{3+} (865 nm, $^4F_{3/2} \rightarrow {}^4I_{9/2}$) and Yb^{3+} (976 nm, $^2F_{5/2} \rightarrow {}^2F_{7/2}$) emission, upon excitation of Nd^{3+} $^4G_{5/2}$ (577 nm) state, for Nd^{3+} doped and Nd^{3+}- Yb^{3+} co-doped phosphors, with and without Li^+, are depicted in Fig. 7. All decay curves could be described by double exponential decay time. The non-exponential decay of Nd^{3+}- Yb^{3+} doped samples reflects the random distributions of Yb^{3+} ions around Nd^{3+} ions [15,16]. To obtain an accurate average lifetime, a double exponential fitting was performed using the following equation:

$$I(t) = I_0 + A_1 e^{-\frac{t}{\tau_1}} + A_2 e^{-\frac{t}{\tau_2}} \quad (7)$$

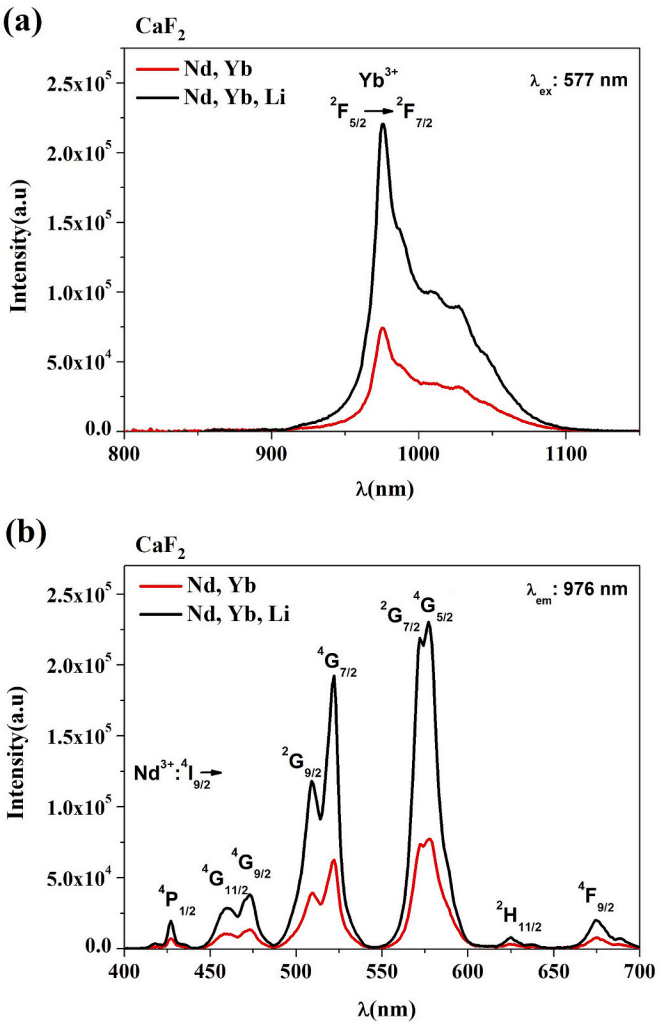

Fig. 6. (a) Emission spectra upon the excitation of Nd^{3+} at 577 nm and (b) excitation spectra monitoring the emission of Yb^{3+} at 976 nm, for the CaF_2:Nd, Yb (red line) and CaF_2:Nd,Yb, Li (black line). (For interpretation of the references to colour in this figure legend, the reader is referred to the Web version of this article.)

where $I(t)$ is the emission intensity at a time t, I_0 is a constant related to the background, A_1 and A_2 are amplitude constants, and τ_1 and τ_2 are the fast and slow lifetime components, respectively. Using the fitted values for τ_1 and τ_2, an accurate average lifetime $< \tau >$ was calculated by the following equation [42]:

$$\tau = \frac{A_1\tau_1^2 + A_2\tau_2^2}{A_1\tau_1 + A_2\tau_2} \tag{8}$$

The average calculated lifetime values for doped CaF_2 samples are listed in Tables 2 and 3. A reduction of the lifetime value measured for the Nd @ 865 nm is observed when Yb^{3+} ion is present for samples with no Li^+ (CaF_2:Nd,Yb), as expected for an energy transfer mediated process. The energy transfer efficiency of Nd^{3+} to Yb^{3+} was estimated through the following expression [43]:

$$\eta = 1 - \frac{\tau_d}{\tau_d^0} \tag{9}$$

where τ_d^0 and τ_d are the average lifetimes of CaF_2:Nd in absence and presence of Yb^{3+}, respectively, calculated by using the Nd^{3+} $^4F_{3/2}$ level decay time data; it gives as a result an energy transfer efficiency of 0.17.

Analyzing average lifetimes of Yb^{3+} and Nd^{3+} emissions, in CaF_2:Nd, Yb sample one can note a smaller average lifetime for Yb @ 976 nm than for Nd @ 865 nm, which could corroborate the possible energy transfer path from Nd^{3+} $^4G5_{/2}$ to Yb^{3+} ($^2F_{5/2} \rightarrow {}^2F_{7/2}$). The sample with Li^+ (CaF_2:Nd,Yb,Li), on the contrary, presents longer lifetimes for both the Nd @ 865 nm and the Yb @ 976 nm emissions. The observed increment of the average lifetime for both Nd^{3+} and Yb^{3+} ions emissions with respect to those of Li^+ free samples may indicate that additional radiative recombination paths are introduced by the Li^+ ions through the generation of localized energy states that favors the observed increment of Yb^{3+} related luminescence: it can be attributed to (i) improvement of the crystallinity and (ii) reductionof surface defects by the increased particle size [30].

The non-exponential decay of the Nd^{3+} ion $^4F_{3/2}$ state for the co-doped Nd^{3+}-Yb^{3+} samples was analyzed to know more about the transfer energy mechanism with the Burshtein Model [44,45]:

$$I(t) = I_0 exp\left(-\frac{t}{\tau_0} - \gamma_s t^{3/S} - w_m t\right) \tag{10}$$

where I_0 is the intensity at $t = 0$, τ_0 is the average lifetime of Nd^{3+} at 865 nm emission in absence of Yb^{3+}, γ_s is related with the direct energy transfer, w_m is the migration rate and S can take constant values depending on electric interaction, namely 6 for dipole-dipole (d-d), 8 for dipole-quadrupole (d-q) and 10 for quadrupole-quadrupole (q-q). The best fit obtained for the data corresponds to S = 6, thus the energy transfer mechanism between Nd^{3+} and Yb^{3+} is assumed to be a dipole-dipole interaction. The migration parameter w_m was negligible ($\sim 10^{-14}$ s^{-1}) for phosphors with and without Li^+, discarding the donor-donor energy migration by diffusion or the hopping process [44], suggesting a direct donor-acceptor energy transfer. Therefore, γ_s (equation taken from the Inokuti-Hirayama model [45,46]) is given by:

$$\gamma_s = \frac{4\pi}{3}\Gamma\left(1 - \frac{3}{S}\right) N_A \left(\frac{R_0}{\tau_0^{1/S}}\right)^3 \tag{11}$$

where N_A is the acceptor concentration and R_0 is the critical transfer distance. From the fitting (S = 6) of the decay curve to expression (9), a γ_s value of 4.07 $s^{-1/2}$ and 48.07 $s^{-1/2}$ is obtained for Nd^{3+}- Yb^{3+} doped CaF_2 with and without Li^+ ions, respectively. Using the Yb^{3+} ion concentration (4% mol) $N_A \approx 2.44 \times 10^{20}$ $ions/cm^3$, the values calculated for R_0 are 3.81 Å and 8.68 Å for samples with and without Li^+ ions, respectively, implying a decrease of the sensitizer-activator critical distance induced by Li^+ ions incorporation [47]. Since also the luminescence intensity increases with Li^+ ions, it suggests that, together with the charge compensation action of Li^+ ions, changes in the host matrix structure are induced that result in a reduction on the formation of Nd^{3+}-Nd^{3+} and/or Yb^{3+}- Yb^{3+} clusters, favoring the formation of Nd^{3+}- Yb^{3+} pairs in the host and decreasing non-radiative recombination processes [11,32,48].

3.5. Energy transfer processes

The energy level diagram of Nd^{3+} and Yb^{3+} ions and the energy transfer processes between them are presented in Fig. 8. Upon Nd^{3+} $^4G_{5/2}$ state excitation at 577 nm in Nd^{3+}- Yb^{3+} co-doped samples, two possible energy transfer paths could happen. The first possible energy transfer path is from Nd^{3+} $^4G_{5/2}$ to Yb^{3+} ($^2F_{5/2} \rightarrow {}^2F_{7/2}$). The second energy transfer path, which is proposed in some literature [13,15,45], is Nd^{3+} ($^4G_{5/2} \rightarrow {}^4F_{3/2}$) and Yb^{3+} (976 nm, $^2F_{5/2} \rightarrow {}^2F_{7/2}$). In the case of introduction of Li^+ into the matrix, similar possible energy transfer and radiative recombination paths are proposed, but they are affected by the reduction of separate clustering of Nd^{3+}- Nd^{3+} and/or Yb^{3+}- Yb^{3+} and by the formation of Nd^{3+}- Yb^{3+} pairs, as described above, which would reduce non-radiative recombination paths.

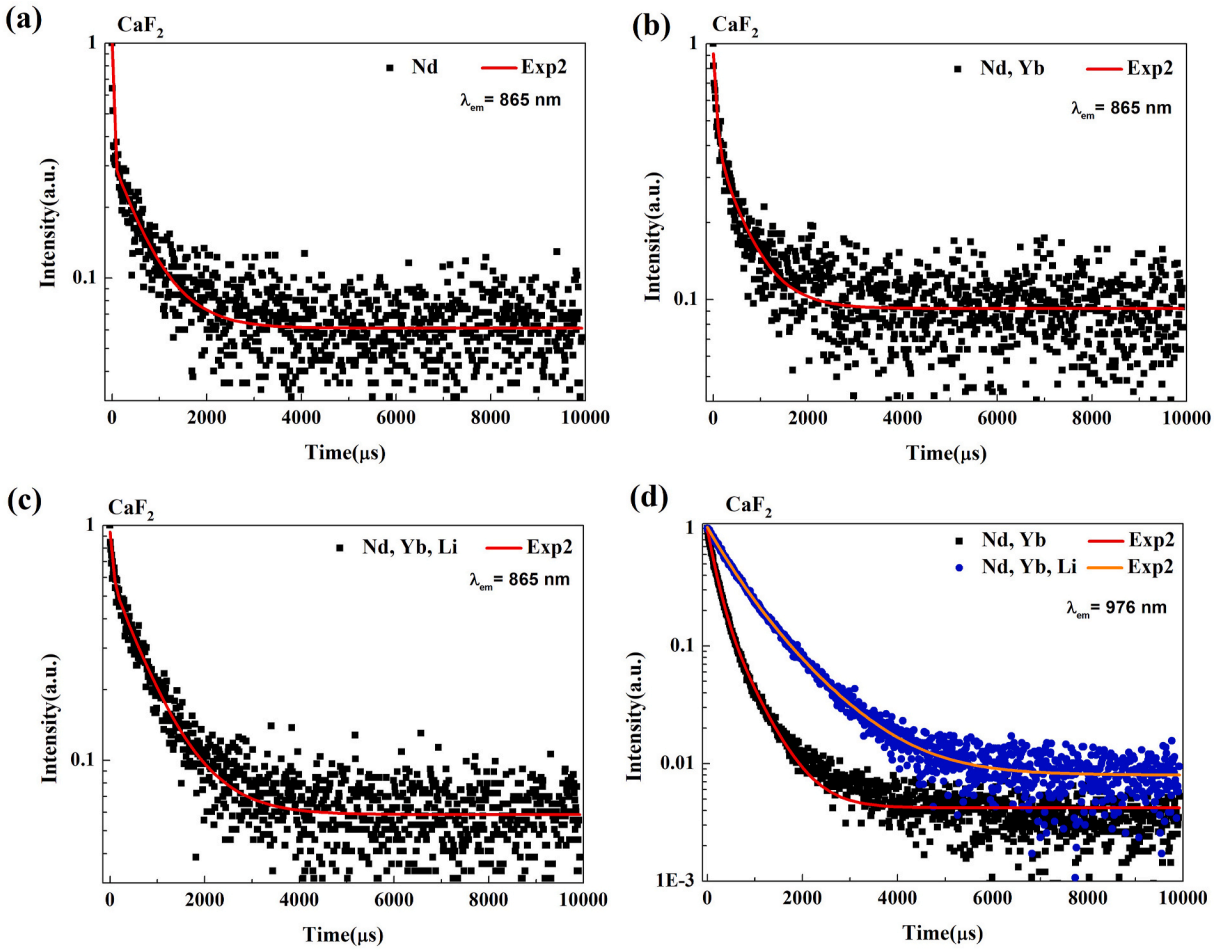

Fig. 7. Decay curves of Nd^{3+} $^4F_{3/2}$ (865 nm) in samples of (a) CaF_2:Nd, (b) CaF_2:Nd, Yb (c) and CaF_2:Nd,Yb, Li and decay curves of (d) Yb^{3+} $^2F_{5/2}$ (976 nm) state emission upon Nd^{3+} $^4G_{5/2}$ state excitation at 577 nm.

Table 2
The fitted τ_1 and τ_2 values and the average lifetime τ at 865 nm for CaF_2:Nd, CaF_2:Nd, Yb and CaF_2:Nd,Yb,Li.

865 nm	Samples	τ_1 (μs)	τ_2 (μs)	τ_{avg} (μs)
	CaF_2:Nd	646.51	14.26	612.80
	CaF_2:Nd,Yb	578.63	62.40	507.76
	CaF_2:Nd,Yb,Li	646.77	25.19	622.24

Table 3
The fitted τ_1 and τ_2 values and the average lifetime τ and at 976 nm for CaF_2: Nd, Yb and CaF_2:Nd,Yb,Li.

976 nm	Samples	τ_1 (μs)	τ_2 (μs)	τ_{avg} (μs)
	CaF_2:Nd,Yb	500.02	166.67	348.60
	CaF_2:Nd,Yb,Li	1011.73	466.75	812.62

4. Conclusion

Nano-structured CaF_2:Nd, Yb and CaF_2:Nd,Yb, Li phosphors were synthesized successfully by co-precipitation and hydrothermal method. The introduction of Li^+ ions as charge compensators in CaF_2:Nd, Yb samples improves the crystallinity of the phosphors, reduces hydroxyl and other groups that work as non-radiative channels and decreases the formation of Nd^{3+}- Nd^{3+} and/or Yb^{3+}- Yb^{3+} clusters, favoring the formation of Nd^{3+}- Yb^{3+} pairs in the host, decreasing non-radiative recombination processes. This is reflected in the visible-light excited NIR luminescence emission, which is enhanced by factor of 2 and 5 times

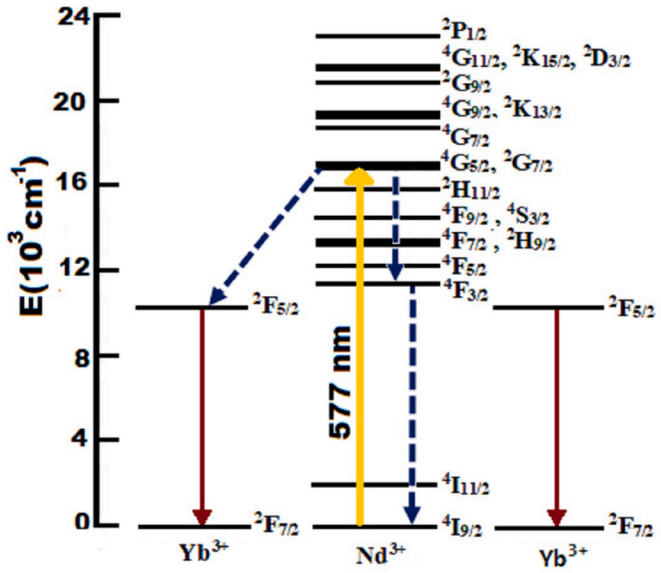

Fig. 8. Energy level diagram Nd^{3+} and Yb^{3+} ions and energy transfer process between them in CaF_2 host.

for phosphors synthesized by the co-precipitation and hydrothermal method, respectively. The present results suggest the potential use of CaF_2:Nd,Yb, Li phosphors for indoor visible light harvesting in

photovoltaic cells for IoT powering applications.

Declaration of competing interest

The authors declare that they have no known competing financial interests or personal relationships that could have appeared to influence the work reported in this paper.

Acknowledgments

The authors acknowledge the technical assistance of Z. Rivera, M. Guerrero, A. Soto from physics department and M. A. Leyva from chemistry department of CINVESTAV-IPN. We also thank CONACyT for the financial support (Project A1-S-26432 and Scholarship 640301).

References

[1] The growth in connected IoT devices is expected to generate 79.4ZB of data in 2025, according to a new IDC forecast. https://www.idc.com/getdoc.jsp?containerId=prUS45213219, 2019. (Accessed 13 July 2020).

[2] S.V. Kuznetsov, O.A. Morozov, V.G. Gorieva, M.N. Mayakova, M.A. Marisov, V. V. Voronov, A.D. Yapryntsev, V.K. Ivanov, A.S. Nizamutdinov, V.V. Semashko, P. P. Fedorov, Synthesis and luminescence studies of CaF_2:Yb:Pr solid solutions powders for photonics, J. Fluor. Chem. 211 (2018) 70–75, https://doi.org/10.1016/j.jfluchem.2018.04.008.

[3] M.B. De Mora, B.M. Monroy, J.E. Lugo, Solar energy materials & solar cells materials for downconversion in solar cells : perspectives and challenges, Sol. Energy Mater. Sol. Cells 165 (2017) 59–71, https://doi.org/10.1016/j.solmat.2017.02.016.

[4] P. Kumar, S. Singh, R. Lahon, A. Gundimeda, G. Gupta, A strategy to design lanthanide doped dual-mode phosphor mediated spectral convertor for solar cell applications, J. Lumin. 196 (2018) 207–213, https://doi.org/10.1016/j.jlumin.2017.12.035.

[5] S. V Kuznetsov, O.A. Morozov, V.G. Gorieva, M.N. Mayakova, M.A. Marisov, V. V Voronov, $Ca_{1-x-y}Yb_xPr_yF_{2+x+y}$ solid solution powders as a promising materials for crystalline silicon solar energetics, Nanosyst. Physics, Chem. Math. 9 (2018) 259–265, https://doi.org/10.17586/2220-8054-2018-9-2-259-265.

[6] C. Falcony, J.U. Balderas, On the use of organic ligands to sensitize inorganic phosphors for ultraviolet, visible, and infrared light harvesting, J. Vac. Sci. Technol. B. 37 (2019) 28501, https://doi.org/10.1116/1.5084283.

[7] M.A. Green, S.P. Bremner, Energy conversion approaches and materials for high-efficiency photovoltaics, Nat. Mater. 16 (2016) 23–34, https://doi.org/10.1038/nmat4676.

[8] M. Guan, L. Mei, Z. Huang, C. Yang, Q. Guo, Z. Xia, Infrared physics & technology synthesis and near-infrared luminescence properties of LaOCl :Nd^{3+}/Yb^{3+}, Infrared Phys. Technol. 60 (2013) 98–102, https://doi.org/10.1016/j.infrared.2013.03.014.

[9] X. Bian, Q. Shi, C. Cui, L. Wang, Y. Tian, B. Xu, Z.K. Mamytbekov, P. Huang, Near-infrared luminescence and energy transfer mechanism in K_2YF_5:Nd^{3+}, Mater. Res. Bull. J. 110 (2019) 102–106, https://doi.org/10.1016/j.materresbull.2018.10.024.

[10] S. Li, Q. Huang, Y. Jiang, Min Hu, Near-infrared quantum cutting for solar cells in Ce^{3+}-Yb^{3+} Co-doped CaF_2 nanoparticles, J. Nanosci. Nanotechnol. 16 (2016) 3679–3683, https://doi.org/10.1166/jnn.2016.11823.

[11] W. Xu, Y. Hu, L. Zheng, Z. Zhang, W. Cao, H. Liu, Enhanced NIR-NIR luminescence from $CaWO_4$:Nd^{3+}/Yb^{3+} phosphors by Li^+ codoping for thermometry and optical heating, J. Lumin. J. 208 (2019) 415–423, https://doi.org/10.1016/j.jlumin.2019.01.005.

[12] X. Zhao, Z. Yang, X. Yang, R. Wang, M. Yuan, K. Han, Z. Jiang, H. Wang, X. Xu, Controlling the multicolor upconversion luminescence in CaF_2 nanocrystals doped with Yb^{3+}, Er^{3+} and Nd^{3+} ions under the excitation of a 808 nm laser, Opt. Mater. Express 9 (2019) 4578, https://doi.org/10.1364/ome.9.004578.

[13] S. Shi, Q. Shi, C. Cui, L. Wang, Y. Tian, P. Huang, Near-infrared luminescence and energy transfer processes in LaOF:Nd^{3+}, Yb^{3+}, RSC Adv. 6 (2016) 92127–92132, https://doi.org/10.1039/c6ra19953d.

[14] A. Vyas, C.P. Joshi, S.V. Moharil, Sensitization of nir emission by tetravalent cerium in K_2CeO_3:Nd,Yb, J. Alloys Compd. 763 (2018) 159–163, https://doi.org/10.1016/j.jallcom.2018.05.285.

[15] X. Bian, Q. Shi, C. Cui, L. Wang, Y. Tian, B. Xu, Z.K. Mamytbekov, P. Huang, Near-infrared luminescence and energy transfer mechanism in K_2YF_5:Nd^{3+}, Yb^{3+}, Mater. Res. Bull. 110 (2019) 102–106, https://doi.org/10.1016/j.materresbull.2018.10.024.

[16] J.M. Meijer, L. Aarts, B.M. Van Der Ende, T.J.H. Vlugt, A. Meijerink, Downconversion for solar cells in YF_3: Nd^{3+}, Yb^{3+}, Phys. Rev. B Condens. Matter 81 (2010) 1–9, https://doi.org/10.1103/PhysRevB.81.035107.

[17] C. Falcony, M.A. Aguilar-Frutis, M. García-Hipólito, Spray pyrolysis technique; High-K dielectric films and luminescent materials: a review, Micromachines 9 (2018) 1–33, https://doi.org/10.3390/mi9080414.

[18] K. Grzeszkiewicz, L. Marciniak, W. Stręk, D. Hreniak, Downconversion in $Y_2Si_2O_7$: Pr^{3+}, Yb^{3+} polymorphs for its possible application as luminescent concentrators in photovoltaic solar-cells, J. Lumin. 177 (2016) 172–177, https://doi.org/10.1016/j.jlumin.2016.04.007.

[19] J. Hu, Y. Zhao, B. Chen, H. Xia, Y. Zhang, H. Ye, Efficient near-infrared downconversion and energy transfer mechanism in Pr^{3+}/Yb^{3+} co-doped $Na_5Y_9F_{32}$ single crystals, J. Lumin. 205 (2019) 500–507, https://doi.org/10.1016/j.jlumin.2018.10.002.

[20] M.S. Pudovkin, D.A. Koryakovtseva, E.V. Lukinova, S.L. Korableva, R. S. Khusnutdinova, A.G. Kiiamov, A.S. Nizamutdinov, V.V. Semashko, Characterization of Pr-doped LaF_3 nanoparticles synthesized by different variations of coprecipitation method, J. Nanomater. 2019 (2019) 1–17, https://doi.org/10.1155/2019/7549325.

[21] M. Runowski, S. Lis, Nanocrystalline rare earth fluorides doped with Pr^{3+} ions, J. Rare Earths 34 (2016) 802–807, https://doi.org/10.1016/S1002-0721(16)60097-2.

[22] D. Yuan, W. Li, B. Mei, J. Song, Synthesis and characterization of Nd^{3+}-doped CaF_2 nanoparticles, J. Nanosci. Nanotechnol. 15 (2015) 9741–9745, https://doi.org/10.1166/jnn.2015.10345.

[23] J. Tan, X. Jin, Monodisperse, colloidal and luminescent calcium fluoride nanoparticles via a citrate-assisted hydrothermal route, J. Colloid Interface Sci. 531 (2018) 444–450, https://doi.org/10.1016/j.jcis.2018.07.081.

[24] P. Cortelletti, C. Facciotti, I.X. Cantarelli, P. Canton, M. Quintanilla, F. Vetrone, A. Speghini, M. Pedroni, Nd^{3+} activated CaF_2 NPs as colloidal nanothermometers in the biological window, Opt. Mater. 68 (2017) 29–34, https://doi.org/10.1016/j.optmat.2016.11.019.

[25] V.S. Singh, C.P. Joshi, S.V. Moharil, P.L. Muthal, S.M. Dhopte, Modification of luminescence spectra of CaF_2: Eu^{2+}, Luminescence 30 (2015) 1101–1105, https://doi.org/10.1002/bio.2865.

[26] T. Xu, N. Ding, X. Yang, Q. Liu, L. Wang, L. Zhang, Q. Zhang, Influence of charge compensators Li^+/Na^+/K^+ on luminescence properties of Sr_2CeO_4:Eu^{3+}, J. Mater. Sci. Mater. Electron. 27 (2016) 10207–10212, https://doi.org/10.1007/s10854-016-5098-9.

[27] P. Cortelletti, M. Pedroni, F. Boschi, S. Pin, P. Ghigna, P. Canton, F. Vetrone, A. Speghini, Luminescence of Eu^{3+} activated CaF_2 and SrF_2 nanoparticles: effect of the particle size and codoping with alkaline ions, Cryst. Growth Des. 18 (2018) 686–694, https://doi.org/10.1021/acs.cgd.7b01050.

[28] B. Xu, D. Li, Z. Huang, C. Tang, W. Mo, Y. Ma, Alleviating luminescence concentration quenching in lanthanide doped CaF_2 based nanoparticles through Na^+ ion doping, Dalton Trans. 47 (2018) 7534–7540, https://doi.org/10.1039/c8dt00519b.

[29] S.K. Gupta, K. Sudarshan, A.K. Yadav, R. Gupta, D. Bhattacharyya, S.N. Jha, R. M. Kadam, Deciphering the role of charge compensator in optical properties of $SrWO_4$:Eu^{3+}:A (A = Li^+, Na^+, K^+): spectroscopic insight using photoluminescence, positron annihilation, and X-ray absorption, Inorg. Chem. 57 (2018) 821–832, https://doi.org/10.1021/acs.inorgchem.7b02780.

[30] A.K. Singh, S.K. Singh, S.B. Rai, Role of Li+ ion in the luminescence enhancement of lanthanide ions: favorable modifications in host matrices, RSC Adv. 4 (2014) 27039–27061, https://doi.org/10.1039/c4ra01055h.

[31] E.F. Huerta, S. Carmona-Téllez, J.G. Cabañas-Moreno, C. Falcony, Visible and near infrared upconversion photoluminescence from Y_2O_3:Er^{3+}, Yb^{3+}, Li+ phosphors under 1532 nm excitation light, J. Alloys Compd. 732 (2018) 422–428, https://doi.org/10.1016/j.jallcom.2017.10.182.

[32] T. Wang, Y. Yu, X. Ji, W. Xu, Y. Fu, H. Cao, Q. He, J. Cheng, A new method to synthesize Sub-10 nm CaF_2 : Nd^{3+} nanoparticles and fluorescent enhancement via Li^+ ions or Ce^{3+} ions doping, Dyes Pigments 175 (2020) 108129, https://doi.org/10.1016/j.dyepig.2019.108129.

[33] S.K. Ranjan, A.K. Soni, V.K. Rai, Nd^{3+}-Yb^{3+}/Nd^{3+}-Yb^{3+}-Li+ co-doped Gd2O3 phosphors for up and down conversion luminescence, Luminescence 33 (2018) 647–653, https://doi.org/10.1002/bio.3458.

[34] N. Omolfajr, S. Nasser, R. Mahmood, A. Kompany, Synthesis and characterization of CaF_2 NPs with co-precipitation and hydrothermal methods, J. Nanomed. Nanotechnol. 2 (2011) 10–13, https://doi.org/10.4172/2157-7439.1000116.

[35] A.V. Rane, K. Kanny, V.K. Abitha, S. Thomas, Methods for synthesis of nanoparticles and fabrication of nanocomposites, in: Synth. Inorg. Nanomater, Elsevier Ltd., 2018, pp. 121–139, https://doi.org/10.1016/b978-0-08-101975-7.00005-1.

[36] C. Pandurangappa, B.N. Lakshminarasappa, B.M. Nagabhushana, Synthesis and characterization of CaF_2 nanocrystals, J. Alloys Compd. 489 (2010) 592–595, https://doi.org/10.1016/j.jallcom.2009.09.118.

[37] G. Salas, R. Costo, M. del Puerto Morales, Synthesis of inorganic nanoparticles, in: Front. Nanosci, 2012, pp. 35–79, https://doi.org/10.1016/B978-0-12-415769-9.00002-9.

[38] G. Huang, C.H. Lu, H.H. Yang, Magnetic Nanomaterials for Magnetic Bioanalysis, Elsevier Inc., 2018, https://doi.org/10.1016/B978-0-12-814497-8.00003-5.

[39] L. He, X. Zou, X. He, F. Lei, N. Jiang, Q. Zheng, C. Xu, Y. Liu, D. Lin, Reducing grain size and enhancing luminescence of $NaYF_4$:Yb^{3+}, Er^{3+} upconversion materials, Cryst. Growth Des. 18 (2018) 808–817, https://doi.org/10.1021/acs.cgd.7b01274.

[40] B. Sn, N. Yb, Photoluminescence , structural , morphology and dielectric properties of, J. Sci. Res. Sci. 36 (2019) 248–268.

[41] B. Xu, H. He, Z. Gu, S. Jin, Y. Ma, T. Zhai, Improving 800 nm triggered upconversion emission for lanthanide-doped CaF_2 nanoparticles through sodium ion doping, J. Phys. Chem. C 121 (2017) 18280–18287, https://doi.org/10.1021/acs.jpcc.7b05639.

[42] O. Soriano-Romero, R.L. Flores-Cruz, R. Lozada-Morales, U. Caldiño, C. Falcony, S. Cármona-Téllez, I. Camarillo, A. Méndez-Blas, A.N. Meza-Rocha, Tunable white light emission in zinc phosphate glasses activated with Ag_m^{n+} clusters and Sm^{3+}, J. Lumin. 222 (2020) 1–9, https://doi.org/10.1016/j.jlumin.2020.117104.

[43] E.F. Huerta, A.N. Meza-Rocha, R. Lozada-Morales, A. Speghini, S. Bordignon, U. Caldiño, White, Yellow and reddish-orange light generation in lithium-

aluminum-zinc phosphate glasses co-doped with Dy^{3+}/Tb^{3+} and tri-doped with Dy^{3+}/Tb^{3+}/Eu^{3+}, J. Lumin. 219 (2020) 116882, https://doi.org/10.1016/j.jlumin.2019.116882.

[44] A.D. Sontakke, K. Biswas, A.K. Mandal, K. Annapurna, Concentration quenched luminescence and energy transfer analysis of Nd^{3+} ion doped Ba-Al-metaphosphate laser glasses, Appl. Phys. B Laser Optic. 101 (2010) 235–244, https://doi.org/10.1007/s00340-010-4010-1.

[45] U. Caldiño, D. Jaque, E. Martín-Rodríguez, M.O. Ramírez, J. García Solé, A. Speghini, M. Bettinelli, $Nd^{3+} \rightarrow Yb^{3+}$ resonant energy transfer in the ferroelectric $Sr_{0.6}Ba_{0.4}Nb_2O_6$ laser crystal, Phys. Rev. B Condens. Matter 77 (2008) 6–13, https://doi.org/10.1103/PhysRevB.77.075121.

[46] M. Rathaiah, A.D. Lozano-Gorrín, P. Babu, C.K. Jayasankar, V. Lavín, V. Venkatramu, Efficient Nd^{3+} sensitized Yb^{3+} emission and infrared-to-visible energy conversion in gallium nano-garnets, RSC Adv. 6 (2016) 78669–78677, https://doi.org/10.1039/c6ra13729f.

[47] M. Ding, Y. Ni, Y. Song, X. Liu, T. Cui, D. Chen, Z. Ji, F. Xu, C. Lu, Z. Xu, Li^{+} ions doping core-shell nanostructures: an approach to significantly enhance upconversion luminescence of lanthanide-doped nanocrystals, J. Alloys Compd. 623 (2015) 42–48, https://doi.org/10.1016/j.jallcom.2014.10.089.

[48] E.F. Huerta, J. De Anda, I. Martínez-Merlin, U. Caldiño, C. Falcony, Near-infrared luminescence spectroscopy in yttrium oxide phosphor activated with Er^{3+}, Li^{+} and Yb^{3+} ions for application in photovoltaic systems, J. Lumin. 224 (2020) 117271, https://doi.org/10.1016/j.jlumin.2020.117271.

Journal of Luminescence 238 (2021) 118241

Contents lists available at ScienceDirect

Journal of Luminescence

journal homepage: www.elsevier.com/locate/jlumin

Ultraviolet to near infrared down-conversion in CaF_2:Nd^{3+}/Yb^{3+}/Li^{+} phosphors

J. De Anda [a,*], F. Enrichi [b,c], G.C. Righini [d], C. Falcony [e]

[a] Centro de Investigación y Estudios Avanzados Del IPN, Programa de Doctorado en Nanociencias y Nanotecnología, Av. IPN 2508, 07360, CDMX, Mexico
[b] Institute of Polar Sciences - National Research Council (ISP-CNR), Via Torino 155, 30172, Mestre-Venezia, Italy
[c] Department of Molecular Sciences and Nanosystems, Ca' Foscari University of Venice, Via Torino 155, 30172, Mestre-Venezia, Italy
[d] Nello Carrara Institute of Applied Physics - National Research Council (IFAC-CNR), Via Madonna Del Piano 10, 50019, Sesto Fiorentino, Firenze, Italy
[e] Centro de Investigación y Estudios Avanzados Del IPN, Departamento de Física, Av. IPN 2508, 07360, CDMX, Mexico

ARTICLE INFO

Keywords:
Down-conversion
CaF2:Nd-Yb
Luminiscence
Li effect

ABSTRACT

Down conversion (DC) in rare-earth-doped optical materials is a process of great interest for the possibility of a substantial increase of the efficiency of silicon solar cells. Here we report the structural and photoluminescence properties of co-doped CaF_2 phosphors obtained by hydrothermal synthesis. In particular, the DC photoluminescence characteristics for UV (353 nm) excitation of Nd^{3+}/Yb^{3+} co-doped CaF_2 phosphors are discussed, underlining the effects due to the co-doping with Li^{+}. The photoluminescence emission is dominated by the near-infrared (NIR) Yb^{3+} emission peaked at 975 nm, although the excitation spectrum corresponds to the characteristic peaks associated with Nd^{3+} excitation at both the UV and visible wavelength ranges. The Nd^{3+} to Yb^{3+} energy transfer mechanisms were determined from a detailed analysis of the excitation spectra characteristics of Nd^{3+} and Nd^{3+}/Yb^{3+}/Li^{+} doped CaF_2 phosphors. DC photoluminescence for UV excitation was confirmed by both the analysis of DC quantum yield efficiency and effective quantum yield measurements. In the first case, an efficiency up to 150% was found, while the effective quantum yield measurements, carried out for the UV (DC) and visible (downshift) excitation and NIR photoluminescence emission, give values of 81 ± 10% and 37 ± 5% for excitation with 353 nm and 577 nm light, respectively.

1. Introduction

Down conversion materials have been widely studied and developed [1–9] because capacity to transform one higher energy photon into two or more lower energy photons. Photovoltaic technology is one of the areas that could take advantage of these materials. It is known that maximum theoretical efficiency for a single-junction (c-Si) solar cell is 30%, which is determined by the Shockley-Queisser limit [10]. The main reason for this low efficiency is the mismatch of the solar light spectrum with the silicon absorption spectrum, determined by the bandgap. Thermalization of the charge carriers with energy larger than the Si bandgap (Eg = 1.12 eV) [11] is the main responsible for the energy loss through non-radiative mechanisms. Thus, there are two spectrum modification strategies to overcome the Shockley-Queisser limit: the up-conversion and the down conversion (quantum cutting) approaches [12]. The up-conversion transforms two or more low-energy photons (lower than the Si gap) into one higher energy photon (equal or higher than 1.1 eV) that can be efficiently absorbed by the c-Si solar cell. This approach has a low quantum yield by nature, requiring high intensity light sources to operate. The down conversion approach (DC), on the other hand, converts a high energy photon into two lower-energy photons (this mechanism is also called quantum cutting, because the energy of a given photon is split into two photons whose sum of energies is equal to or slightly less than the original energy). Hence, luminescent layers based on lanthanides were proposed as an alternative to improve solar cells efficiency through down conversion mechanism [13,14].

The first possible application of sunlight DC in solar cells was studied theoretically by Trupke et al., in 2002 [15]. They demonstrated that a Si solar cell with an ideal DC layer can achieve a maximum energy conversion efficiency of 38.6% with unconcentrated sunlight. The first realization of the quantum cutting luminescence of lanthanide ions was based on the Tb^{3+}–Yb^{3+} pair [16]. Trivalent ytterbium is one of the lanthanides most used in this approach because it has a single excited state $^2F_{5/2}$, with an energy difference around 10,000 cm^{-1} (1000 nm)

* Corresponding author.
E-mail address: jessica.deanda@cinvestav.mx (J. De Anda).

https://doi.org/10.1016/j.jlumin.2021.118241
Received 17 February 2021; Received in revised form 19 April 2021; Accepted 27 May 2021
Available online 31 May 2021

with respect to the ground state $^2F_{7/2}$: the emitted photons at ~ 1000 nm can be efficiently absorbed by c-Si solar cells. Therefore, the RE/Yb^{3+} co-doped material systems (RE = Pr^{3+} [17–19], Tb^{3+} [20–24], Tm^{3+} [6,25], Ce^{3+} [26,27], Ho^{3+} [28], Er^{3+} [29,30], Eu^{2+} [21,31,32], Nd^{3+} [18,33,34]) have attracted much attention in recent years. In these cases, an effective energy transfer (ET) between lanthanide ions is an important factor to have high quantum yields (QY); hence, the lanthanide selection is made to have the less spaced energy levels between RE ions. In this sense, the best potential pairs for this purpose are Er^{3+}/Yb^{3+}, Nd^{3+}/Yb^{3+}, and Pr^{3+}/Yb^{3+} [4]. Another important issue to obtain efficient DC materials is the choice of the proper host material, which must have a large band gap and low phonon energy to minimize multiphonon relaxation processes between the closely spaced RE^{3+} energy levels. Metal fluorides have wide-band gaps and low phonon energy in general, which make them appropriate hosts for DC materials [5]. Among them, CaF_2 has been widely studied and co-doped with different lanthanides, Eu^{2+}/Yb^{3+} [35], Tb^{3+}/Yb^{3+} [24,36], Ce^{3+}/Tb^{3+} [22,26], Eu^{2+}/Tb^{3+} [21,37], Eu^{3+}/Tb^{3+} [38], Er^{3+}/Yb^{3+} [39], Ce^{3+}/Yb^{3+} [40,41], and Nd^{3+}/Yb^{3+} [42–44]. Last pair has been studied also in different host materials [33,34,45–49] and it was selected in this work. In 2006 CaF_2:Nd^{3+}/Yb^{3+} single crystal was firstly reported by V. Petit et *al.* for laser applications [42] but the DC mechanism was not analyzed. In 2017 B. Xu et al. studied up-conversion luminescence of CaF_2:Nd^{3+} and CaF_2:Nd^{3+}/Yb^{3+} phosphors co-doped with Na^+ as charge compensator, improving the energy transfer between Nd^{3+} and Yb^{3+} ions upon 800 nm excitation, in the latter case [43]. In a previous paper we have shown that the incorporation of Li^+ as charge compensator in CaF_2:Nd^{3+}/Yb^{3+} phosphors leads to an enhancement of the NIR photoluminescence excited by visible light [44]. Thus, we considered it could be worthwhile to extend the characterization of Li-compensated Nd^{3+}/Yb^{3+} co-doped CaF_2 phosphors to the case of down-conversion. It has also to be noted that, whereas there is an increasing number of papers in the literature concerning the effect of Li^+ addition on the luminescence enhancement, at our knowledge there have been very few studying the downconversion.

Even though, as noted above, there is a large number of works reporting DC mechanism in different types of lanthanide co-doped hosts with high energy transfer yields, only few of them report experimental effective QY measurements for UV–Vis–NIR DC luminescence. Some of the experimental effective QY reported at NIR emission trough an integrating sphere are: 11.5% for SF_2:0.3Tb-2.7 Yb [50], 9.21% for CaF_2:30Nd/Na@CaF_2 [51], up to 18.7% for $NaErF_4$@$NaYbF_4$@$NaYF_4$ [52], 35 ± 5% for Gd_2O_3:1Bi, 4 Yb [27], 5.6% for CaF_2:0.1Ce:10 Yb [41]. In the present work, optimization RE^{3+} doping concentrations was done to boost the QY efficiency with respect to these literature studies. Additionally, the energy transfer mechanism between Nd^{3+} and Yb^{3+} is investigated when these phosphors are excited by UV light (353 nm). The contribution of Li^+ ions on the luminescence intensity enhancement and the DC processes is also analyzed considering the time-resolved PL emission and the excitation/emission spectral characteristics of $Nd^{3+}/Yb^{3+}/Li^+$ co-doped CaF_2 phosphors.

2. Materials and methods

2.1. Materials

$CaCl_2{\cdot}H_2O$ (99.0%), $NdCl_3{\cdot}6H_2O$ (99.9%), $YbCl_3{\cdot}6H_2O$ (99.9%), LiCl (99.0%) and NH_4F (98.0%) powders were purchased from Sigma-Aldrich and used without further purification.

2.2. Synthesis of the CaF_2:Nd^{3+}, CaF_2:Nd^{3+}/Yb^{3+} and CaF_2:$Nd^{3+}/Yb^{3+}/Li^+$ nanostructured phosphors

Co-doped CaF_2 phosphors were synthesized by hydrothermal method. The compositions synthetized were: (a) CaF_2 doped with 4 mol % Nd^{3+} (denoted as CaF_2:Nd4); (b) co-doped with 4 mol% Nd^{3+} and 4 mol% Yb^{3+} (denoted as CaF_2:Nd4/Yb4); and (c) co-doped with 4 mol% Nd^{3+}, X mol% Yb^{3+} and Z mol% Li^+ concentrations (denoted as CaF_2:Nd4/YbX/LiZ), where X = 4, 5, 6 and Z = 1, 2, 3, 4. RE^{3+} and Li^+ concentrations were decided from preliminary trials and following previous studies [44]. The synthesis was carried out with the same procedure described for CaF_2:Nd^{3+}:Yb^{3+}:Li^+ in a previous article [44]. Stoichiometric amounts of $CaCl_2$, $YbCl_3$, $NdCl_3$, and LiCl were dissolved in 10 mL of deionized water for 10 min. A 1 M of NH_4F aqueous solution was added to chloride solution, mixed for 10 min and transferred to a Teflon/Lined autoclave. After 8 h heating at 170 °C, the autoclave was cooled down at room temperature. Then, the suspension was washed, dried and finally gradually annealed (200 °C for 30 min, 400 °C for 30 min and 600 °C for 2 h).

2.3. Instruments and measurements

XRD measurements were performed by Siemens D-500 diffractometer with CuKα source (α = 1.54 Å). The photoluminescence characteristics, DC and downshifted near-infrared photoluminescence and time-resolved fluorescence measurements were carried out using an Edinburgh Instruments 980 S spectrophotometer. The measurements of the external (effective) quantum yield (QY_{eff}) were performed with an integrating sphere in the same Edinburgh instrument. All measurements were carried out at room temperature.

3. Results and discussion

3.1. X-ray diffraction analysis

XRD diffractograms for CaF_2:Nd4/Yb4 with different Li^+ ions concentration are depicted in Fig. 1. All observed diffraction peaks correspond to the CaF_2 cubic phase (standard PDF card #96-100-0044), hence the incorporation of RE^{3+} and Li^+ ions as dopants does not change the CaF_2 cubic phase. However, shifts towards higher angles due to the introduction of Li^+ ions up to a 2% concentration are noticed, as shown in Fig. 1(b) for the peak at ~47°. At higher Li^+ concentrations (3 and 4%) this peak shifts back towards lower angles. The incorporation of RE^{3+} in CaF_2, substituting Ca^{2+} ions, is known to generate an excess of positive charges which is regularly compensated by interstitial fluorine ions around a Ca vacancy. The charge repulsion between F^- ions and the difference in size with replacing ions finally produces lattice defects. When Li^+ ions are introduced into CaF_2:Nd/Yb phosphors as charge compensators, they can occupy, due to their small ionic radius (~0.92 Å), Ca^{2+} (ionic radius ~ 1.12 Å) substitutional or interstitial sites in the lattice, leading to a shrinkage or an expansion of the host, respectively [18,53,54]. Therefore, reducing lattice effects generated by interstitial F^- ions. The above described behavior of the CaF_2:Nd/Yb x-ray diffractograms (Fig. 1(b)) indicates that for Li^+ concentrations up to 3 mol %, Li^+ ions substitute Ca^{2+} vacancies sites, while a higher Li^+ concentration starts filling interstitial sites as well. Furthermore, the intensity's second peak (highest XRD peak for CaF_2 compound) is recovered with the Li^+ addition (Fig. 1(a)) and the lower FWHM for Li 1,2,3 mol% concentrations, suggesting a crystallinity improvement. Crystallite size, calculated through Scherrer equation, increases from 25 up to 92 nm approximately for Li^+ from 1 to 3 mol%, and then decreases to 76 nm for 4 mol% Li^+ concentration. Therefore, for most of this work, CaF_2:Nd/Yb phosphors with Li^+ concentration up to 3 mol% are considered, unless stated otherwise.

3.2. Photoluminescence analysis

Fig. 2 shows, in the left part, the UV and visible, excitation spectra for CaF_2:Nd4, monitoring the NIR emission spectra of Nd^{3+} $^4F_{3/2} \rightarrow {}^4I_{11/2}$ transition at 1062 nm. On the right side, NIR emission spectra upon 353 nm (black line) and 577 nm (red line) excitation.The intensities of Nd^{3+} emission peaks at 1062 and 865 nm are similar for both, UV and visible

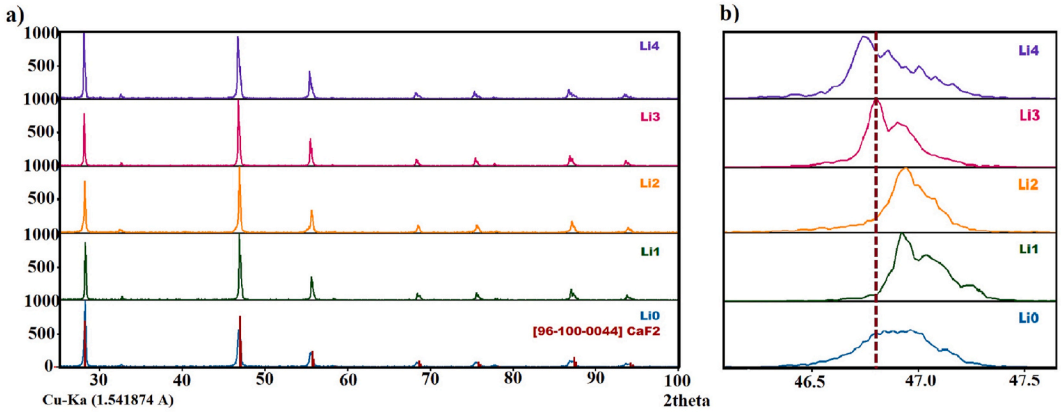

Fig. 1. (a) XRD diffractogram of CaF_2:Nd4/Yb4 with different Li^+ ion concentrations. (b) Dominant peak local magnification.

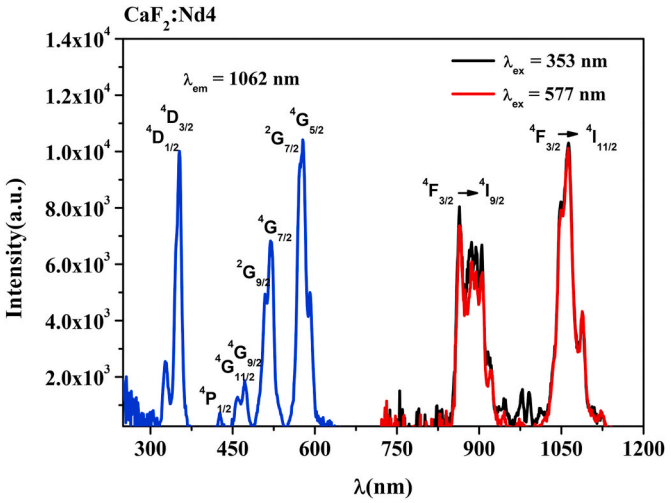

Fig. 2. UV and visible (blue line) excitation spectra for CaF_2:Nd4, monitoring the Nd^{3+} $^4F_{3/2} \rightarrow {}^4I_{11/2}$ transition at 1062 nm. On the right side: NIR emission spectra upon 353 nm (Nd^{3+}: $^4I_{9/2} \rightarrow {}^4D_{3/2}$, black line) and 577 nm (Nd^{3+}: $^4I_{9/2} \rightarrow {}^4G_{5/2}$, red line) excitation.

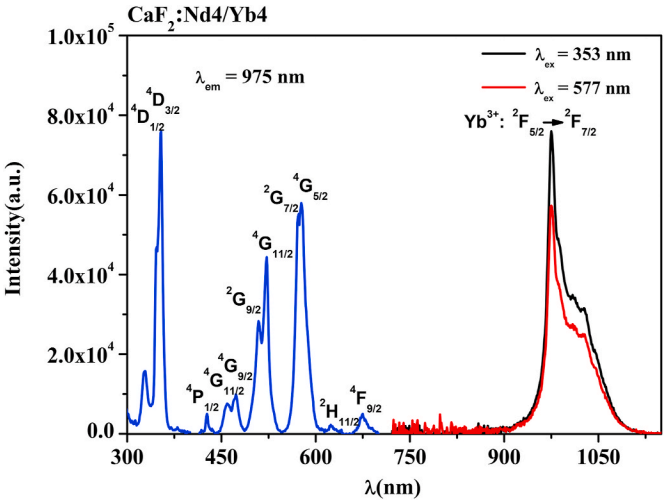

Fig. 3. UV and visible (blue line) excitation spectra for CaF_2:Nd4/Yb4, monitoring $^2F_{5/2} \rightarrow {}^2F_{7/2}$ transition of Yb^{3+} at 975 nm. On the right side: NIR emission spectra upon 353 nm (Nd^{3+}: $^4I_{9/2} \rightarrow {}^4D_{3/2}$, black line) and 577 nm (Nd^{3+}: $^4I_{9/2} \rightarrow {}^4G_{5/2}$, red line) excitation.

excitation wavelengths.

Fig. 3 shows similar data for CaF_2:Nd4/Yb4 phosphors; in this case, the dominant NIR emission corresponds to Yb^{3+} $^4F_{5/2} \rightarrow {}^4F_{7/2}$ transition at 975 nm, while the Nd^{3+} emission peaks ($^4F_{3/2} \rightarrow {}^4I_{9/2}$ at 865 nm and $^4F_{3/2} \rightarrow {}^4I_{11/2}$ at 1062 nm) are drastically reduced. The excitation peaks for the 975 nm Yb emission are basically those associated with the electronic energy levels transitions of Nd^{3+} ion, which confirms the presence of an energy transfer process from the Nd^{3+} ions to the Yb^{3+} ions. When the CaF_2:Nd4/Yb4 phosphors are co-doped with Li^+ ions (Fig. 4), a luminescence intensity increase is observed. Li^+ concentrations from 0 to 4 mol% were introduced in these phosphors, giving as a result that the phosphor with Li^+ 3 mol% concentration presented the highest luminescent intensity, also the XRD analysis show the best crystallite characteristics for this Li^+ concentration. The effect of Li^+ addition to these phosphors has been described in detail in a previous article [44] and it is related to reduction of localized defects and improvement of the crystallinity induced by the Li^+ ions in the Nd, Yb doped CaF_2 crystallites. The incorporation of RE^{3+} in CaF_2, substituting Ca^{2+} ions, is known to generate an excess of positive charges which is regularly compensated by interstitial fluorine ions around a Ca vacancy site. The charge repulsion between F^- ions and the difference in size with replacing ions finally produces lattice defects, which are evidenced by the observed XRD peaks shifting and shape broadening when no Li is

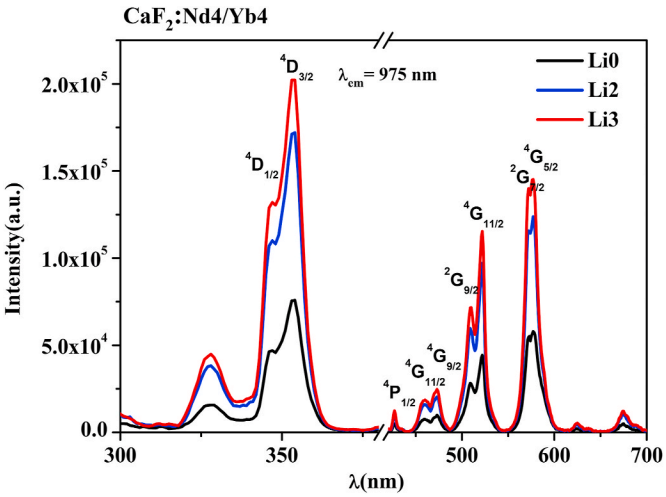

Fig. 4. Excitation spectra of CaF_2:Nd4/Yb4 (black line), CaF_2:Nd4/Yb/Li2 (blue line) and CaF_2:Nd4/Yb/Li3 (red line), at $^4D_{3/2}$ level (353 nm) and $^4G_{5/2}$ level (577 nm), monitoring $^2F_{5/2} \rightarrow {}^2F_{7/2}$ transition of Yb^{3+} at 975 nm.

added (Fig. 2 in ref. 44 for XRD of hydrothermal synthesized CaF_2 phosphors). Co-doping with Li^+ results in a partial recovery of the peaks position and broadness, indicating the reduction of the localized defects induced by the Ln dopants and the consequent crystallinity improvement.

There are two aspects to point out from these results: the first one is the enhancement of the photoluminescence intensity due to the introduction of Li^+ ions (Fig. 4), whereas the second one refers to the intensity ratio of the 353 nm to the 577 nm excitation peaks (Fig. 3). The 353 nm excitation of Nd^{3+} in a Yb^{3+} co-doped phosphor has the capability of a DC energy transfer to Yb^{3+} ions (see Fig. 5), while the excitation with 577 nm can only result in a down-shift energy transfer process. Thus, the comparison of the ratio of these excitation peaks with that of a sample only doped with Nd^{3+} (Fig. 2) can be used as an indicator for the DC process occurrence in these phosphors when excited with 353 nm light. The difference in the excitation peaks ratio, in this case, suggests a down-conversion process presence for the 353 nm excitation [34,48,49,55]. The DC mechanism, through a Nd^{3+} to Yb^{3+} two-step energy transfer path, is depicted in Fig. 5. After Nd^{3+} $^4D_{3/2}$ level is excited (with 353 nm light), it decays by non-radiative relaxation to the $^2G_{9/2}$ level. Then, part of the energy is transferred to Yb^{3+} via cross relaxation $^2G_{9/2} \rightarrow {}^4F_{3/2}$ to Yb^{3+}:$^2F_{5/2} \rightarrow {}^2F_{7/2}$ followed by a second energy transfer step Nd^{3+}:$^4F_{3/2} \rightarrow {}^4I_{9/2}$ to Yb^{3+}:$^2F_{7/2} \rightarrow {}^2F_{5/2}$, populating $^2F_{5/2}$ level of Yb^{3+}.

A confirmation for the DC process occurrence in Nd^{3+}/Yb^{3+} co-doped materials has been proposed earlier by J.M. Meijer et al. in the case of YF_3:Nd/Yb phosphors [34], through the comparison between the intensity of the excitation spectra of Nd^{3+} for the $^4F_{3/2} \rightarrow {}^4I_{9/2}$ transition (at 865 nm) and that for Yb^{3+} $^4F_{5/2} \rightarrow {}^4F_{7/2}$ transition (at 975 nm), as described above. Since the emission intensity for these two peaks is different, both spectra are normalized at the $^4G_{5/2}$ level excitation peak at 577 nm, where a down-shift process occurs. If a DC process is present at any other level that has the requirements to produce this process, then the ratio of the excitation peak for these two emission wavelengths (975 and 865 nm) corresponding to this transition should be larger than 1 (up to 2), as two instead of one IR photons are generated in this process (the factor associated with absorption is cancel out by taking the ratio of the excitation peak for the two emission wavelengths). The down-conversion efficiency is calculated using the excitation peak ratio.

Fig. 6 shows the excitation spectra for CaF_2:Nd4 monitoring the $^4F_{3/2} \rightarrow {}^4I_{11/2}$ transition of Nd^{3+} at 1062 nm and for CaF_2:Nd4/Yb4/LiZ (Z = 0, 2, 3), monitoring $^2F_{5/2} \rightarrow {}^2F_{7/2}$ transition of Yb^{3+} at 975 nm; all spectra are normalized at the 577 nm ($^4G_{5/2}$) peak intensity. The relative

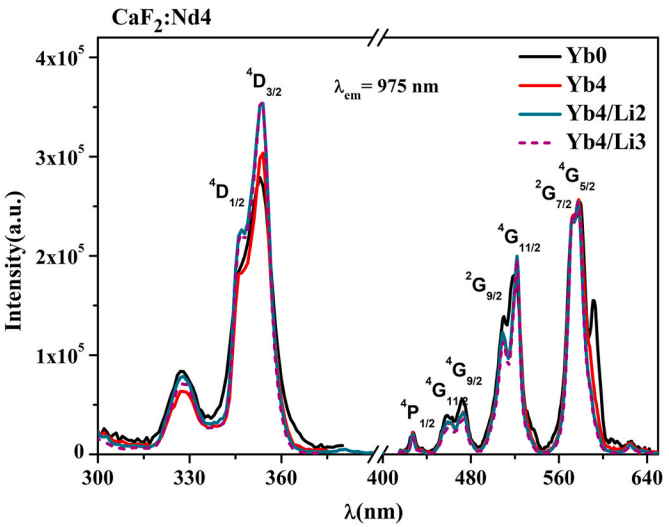

Fig. 6. Excitation spectra normalized at 577 nm ($^4G_{5/2}$) of CaF_2:Nd4/Yb4/LiZ (Z = 0, 2, 3) monitoring $^2F_{5/2} \rightarrow {}^2F_{7/2}$ transition of Yb^{3+} at 975 nm and of CaF_2: Nd4 monitoring $^4F_{3/2} \rightarrow {}^4I_{11/2}$ transition of Nd^{3+} at 1062 nm.

intensity of the excitation peak at 353 nm (Nd^{3+} $^4D_{3/2}$ level) increases in all the CaF_2:Nd4/Yb4/LiZ (Z = 0, 2, 3) phosphors, as expected from a DC photoluminescent process, and the maximum ratio is found for the sample with CaF_2:Nd4/Yb4 with Li^+ ions. As mentioned above, Li^+ ions, working as charge-compensators, not only reduce the Ca^{2+} vacancies generated by the introduction of lanthanides (RE^{3+}) in CaF_2, but also reduce the interstitial F^- ions, which generate lattice distortion. The reduction of lattice distortion improves the phosphors crystallinity and promotes the formation of Nd^{3+}/Yb^{3+} pairs [44]. Further, flux properties [22,56] and reduction of quenching groups are attributed to Li^+ ions [44]. All characteristics mentioned are reflected in the increase of intensity emission of CaF_2: Nd, Yb with Li^+ ions addition.

A Yb^{3+} concentration variation was also carried out to determine the Yb^{3+} contribution to the photoluminescence emission. Three different Yb^{3+} concentrations were analyzed (Fig. 7): CaF_2:Nd4/YbX/Li3 (X = 4, 5, 6). For each Li concentration, the 353 nm–577 nm excitation peaks ratio was similar while the overall luminescence intensity was significantly affected, being maximum for X = 5. To pin down the contribution of Li^+ and Yb^{3+} concentrations in the DC mechanism and to estimate the DC efficiency, the excitation peak intensities at 353 nm were measured

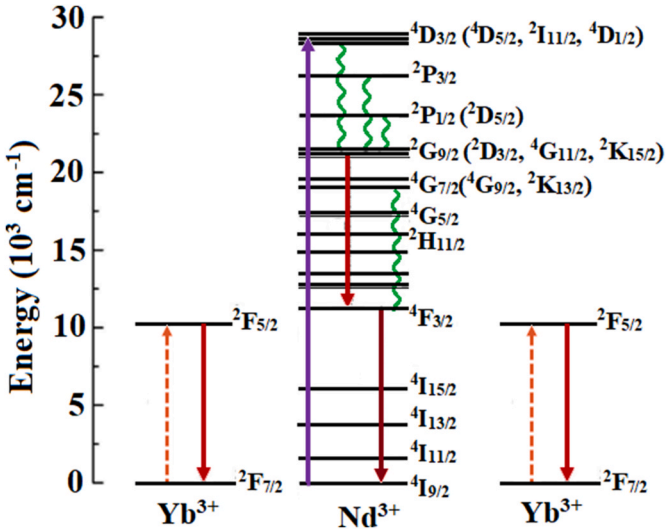

Fig. 5. Energy levels of Nd^{3+} and Yb^{3+} ions and possible down-conversion mechanism between Nd^{3+} and Yb^{3+} in CaF_2:Li^+ matrix.

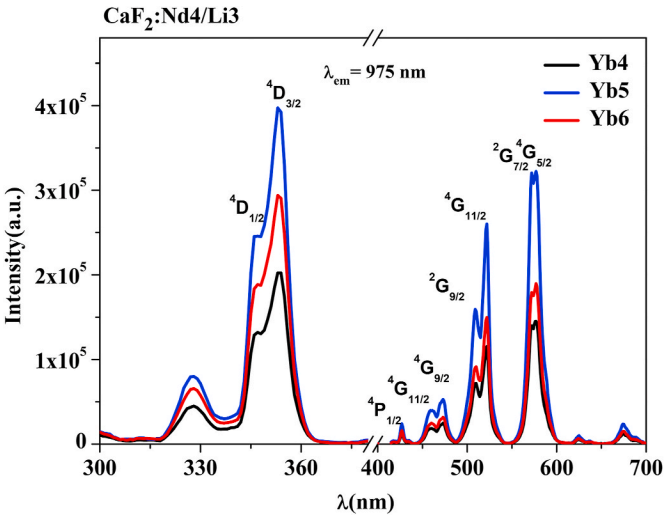

Fig. 7. Excitation spectra of CaF_2:Nd4/YbX/Li3 phosphors (X = 4, 5, 6), monitoring $^2F_{5/2} \rightarrow {}^2F_{7/2}$ transition of Yb^{3+} at 975 nm.

for each sample, monitoring the Nd^{3+} $^4F_{3/2} \rightarrow {}^4I_{9/2}$ transition (865 nm) and the Yb^{3+} $^2F_{5/2} \rightarrow {}^2F_{7/2}$ transition (975 nm). These peak intensities were compared after normalizing the spectra to the excitation peak at 577 nm ($^4G_{5/2}$ level) [34]. Fig. 8 shows, in a bar diagram, the integrated excitation intensities of the $^4D_{3/2}$ state of Nd^{3+} (353 nm) of CaF_2:Nd4/YbX/LiZ (X = 4, 5, 6, and Z = 0, 3) phosphors for λ_{em} = 865 nm (Nd^{3+} $^4F_{3/2} \rightarrow {}^4I_{9/2}$ transition) and for λ_{em} = 975 nm (Yb^{3+} $^2F_{5/2} \rightarrow {}^2F_{7/2}$ transition), both normalized at 577 nm ($^4G_{5/2}$) excitation peak. The integrated intensity ratio for 975 nm and 865 nm emission upon $^4D_{3/2}$ level (353 nm) excitation wavelength is 1.25 for CaF_2:Nd4/Yb4 and 1.26, 1.38 and 1.50 for CaF_2:Nd4/YbX/Li3 where X = 4, 5 and 6, respectively. Hence, a DC luminescence efficiency up to 150% is obtained for the phosphor with the largest amount of Yb^{3+} (6 mol%). The intensity ratio for the phosphor with 4 mol% Yb remains practically unchanged with and without Li^+ (1.25 and 1.26, respectively), indicating that there is no direct contribution of Li^+ to the DC mechanism, as it is observed in Fig. 6. The increase of intensity with increasing Yb^{3+} ions content indicates the presence of more Yb^{3+} ions as close neighbors for each Nd^{3+} ion at a distance appropriated for efficient transfer of energy, hence, more emitting Yb^{3+} ions. However, competing non-radiative processes, such as a concentration quenching for Yb^{3+} ions, could result in an eventual reduction on the external emission intensity, as the maximum external luminescence intensity is observed for Yb = 5 mol% rather than with Yb = 6 mol% (see Fig. 7).

3.3. Time decay

Fig. 9 illustrates the behavior of the normalized time decay curves, in a semilogarithmic scale, for the Nd^{3+} 865 nm emission excited with 353 nm for the CaF_2:Nd4/YbX/Li3 (X = 0, 4) samples. These curves show a fast initial decay τ_1, shorter than 20 μs, followed by a slower decay part with τ_2 constant. The resolution of the experimental arrangement used for this work was 10 μs; thus, the adjusted value for τ_1 indicates only the upper limit for this time constant, its real value being surely shorter than the fitted one. Table 1 lists the fitted τ_1 and τ_2 values for CaF_2:Nd4/YbX/Li3 (X = 0, 4, 5, 6) phosphors according to the following double exponential fitting equation [57]:

$$I(t) = I_0 + A_1 e^{-\frac{t}{\tau_1}} + A_2 e^{-\frac{t}{\tau_2}} \quad (1)$$

where $I(t)$ is the normalized emission intensity as a function of time t, I_0 is a constant related to background, A_1 and A_2 are amplitude constants, and τ_1 and τ_2 are the fast and slow lifetime constants, respectively. The average lifetime τ_{avg}, also listed in Table 1, is calculated through the following equation [57]:

$$\tau = \frac{A_1\tau_1^2 + A_2\tau_2^2}{A_1\tau_1 + A_2\tau_2} \quad (2)$$

Most of the information regarding the energy transfer from Nd^{3+} ($^4F_{3/2}$ level) to Yb^{3+} is contained in the variations of the rapid decay with and without Yb^{3+} co-doping; unfortunately, this information is not resolved with the instrumentation used, therefore future work regarding this particular aspect is needed. The slow part of the time decay shows a

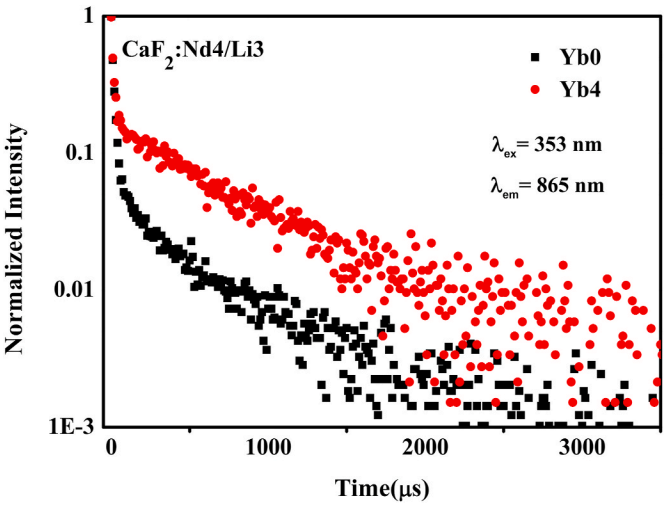

Fig. 9. Lifetime measurements of CaF_2:Nd4/YbX/Li3 (X = 0, 4), for Nd^{3+} $^4F_{3/2}$ emission (865 nm) emission upon $^4D_{3/2}$ level excitation of Nd^{3+} (353 nm).

Table 1
Fitted τ_1, τ_2 and τ_{avg} for Nd^{3+} emission at 865 nm ($^4F_{3/2}$ level) in CaF_2:Nd4/Li3, with different Yb^{3+} concentrations, upon excitation of Nd^{3+} at 353 nm ($^4D_{3/2}$ level).

	Yb0/Li3	Yb4/Li3	Yb5/Li3	Yb6/Li3
A_1	0.93	0.82	0.79	0.78
$\tau_1(\mu s)$	13.93	12.45	12.87	12.68
A_2	0.06	0.16	0.19	0.19
$\tau_2(\mu s)$	425.05	674.79	744.15	662.81
$\tau_{avg}(\mu s)$	279.07	617.80	693.77	615.17

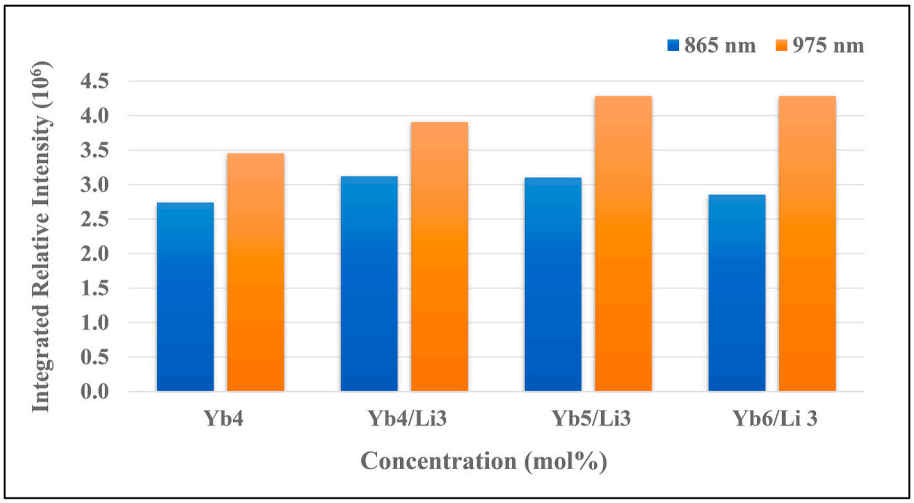

Fig. 8. Comparison of 353 nm integrated excitation intensities of CaF_2:Nd4/Yb4 and CaF_2:Nd4/YbX/Li3 phosphors (X = 4, 5, 6) monitoring $^4F_{3/2} \rightarrow {}^4I_{9/2}$ transition (865 nm) of Nd^{3+} and $^2F_{5/2} \rightarrow {}^2F_{7/2}$ transition (975 nm) of Yb^{3+}. The excitation spectra were normalized at 577 nm ($^4G_{5/2}$) peak.

time constant increment with the introduction of the Yb^{3+} ions, which tends to be higher for the sample with 5 mol% Yb^{3+} content, which is also the most luminescent phosphor.

Fig. 10 shows the time decay plot for the Yb^{3+} emission at 975 nm ($^2F_{5/2}$ level) following the excitation of Nd^{3+} at 353 nm ($^4D_{3/2}$ level) for CaF_2:Nd4/Yb4 and for CaF_2:Nd4/YbX/Li3 phosphors (X = 4, 5, 6). In this case, two exponentials are also needed to fit the data, although the time constants are well defined, and the dominant decay corresponds to the larger average time constant for the samples containing Li 3 mol% (Table 2). In particular, an evident increase in the time constant is observed for the sample with Li^+, CaF_2:Nd4/Yb4/Li3, compared with the one without Li^+. Longer average lifetimes could indicate more favorable Yb^{3+} -Nd^{3+} pairs formation due to Li^+ introduction; hence, larger Nd^{3+} concentrations are required to start seeing concentration quenching effects. Therefore, almost all Nd^{3+} ions have a two-step DC emission as depicted in Fig. 4, with a successful second step energy transfer process from $^4F_{3/2}$ level of Nd^{3+} to $^2F_{7/2}$ level of Yb^{3+}. The decrease of average lifetime for the sample with 6 mol% Yb could be attributed to a concentration quenching effect for Yb^{3+} ions.

3.4. Luminescence effective quantum yield

An integrating sphere was used to measure the external (effective) quantum yield (QY_{eff}), which was obtained from the ratio of the number of photons emitted to the number of photons absorbed by the sample. The number of emitted photons is given by the area under the spectrally corrected emission peak of a sample: A_{em}. The number of absorbed photons is given by the difference of areas under the Rayleigh scattering peaks of a reference sample and a sample under study: $A_{scatref} - A_{scatsample}$. When two different detectors are used for measuring scattering spikes and emission spectrum of a sample, the difference in sensitivity of used detectors should also be considered and the QY_{eff} equation can be written as:

$$QY_{eff} = \frac{A_{em}}{(A_{scatref} - A_{scatsample})k_{Red-PMT/NIR-PMT}} \quad (3)$$

where $k_{Red-PMT/NIR-PMT}$ is the ratio between sensitivities of the two detectors. In the present work, a neutral density filter was placed on the excitation light path, and the ratio of sensitivity between the two detectors was determined by measuring a known signal in the 750–800 nm range with both detectors. The QY_{eff} measured for the sample with the highest photoluminescence signal (CaF_2:Nd4/Yb5/Li3) was 81 ± 10% for UV (353 nm) and 37 ± 5% for visible (577 nm) excitation. Since excitation with 577 nm is associated with a down shift process (one to one photon process) has a measured QY_{eff} lower than that for the 353 nm (about half as much, considering the experimental error bars), these results confirm the occurrence of a DC processes upon UV excitation (353 nm) in CaF2: Nd/Yb/Li phosphors.

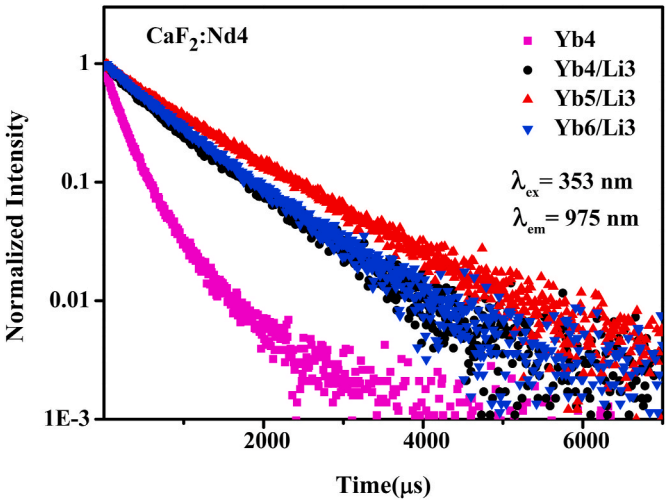

Fig. 10. Lifetime measurements of CaF_2:Nd4/Yb4 and CaF_2:Nd4/YbX/Li3 (X = 4, 5 and 6) for Yb^{3+} $^2F_{5/2}$ emission (975 nm) upon $^4D_{3/2}$ level excitation of Nd^{3+} (353 nm).

Table 2
Fitted τ_1, τ_2 and τ_{avg} for Yb^{3+} emission at 975 nm ($^2F_{5/2}$ level) in CaF_2:Nd4- Yb4 and CaF_2:Nd4/Li3 co-doped with different Yb^{3+} concentrations, upon excitation of Nd^{3+} at 353 nm ($^4D_{3/2}$ level).

	Yb4	Yb4/Li	Yb5/Li3	Yb6/Li3
A_1	0.68	0.39	0.34	0.36
$\tau_1(\mu s)$ 157.05	400.34	612.39	514.73	
A_2	0.29	0.61	0.65	0.64
$\tau_2(\mu s)$	453.96	964.87	1231.91	972.16
$\tau_{avg}(\mu s)$	321.43	845.86	1103.85	867.04

4. Conclusion

The effect of Li^+ addition to rare-earth doped calcium fluoride on down-conversion processes has been studied in hydrothermally synthetized CaF_2 powders containing Nd^{3+} and Yb^{3+}. Down-conversion (DC) mechanism is confirmed to occur in these phosphors upon UV (at 353 nm) excitation, through analysis of DC efficiency and effective quantum yield measurements. Nd^{3+}, Yb^{3+} and Li^+ co-doped CaF_2 phosphors show a photoluminescence emission dominated by the NIR Yb^{3+} emission peaked at 975 nm, upon UV Nd^{3+} excitation. This energy transfer is performed from Nd^{3+} to Yb^{3+} through two paths which allow the DC process. Values up 150% were obtained by means of the analysis of DC efficiency, which is determined from the photoluminescence excitation-emission spectra. CaF_2:Nd4/Yb5/Li3 phosphors showed the highest emission intensity. Effective quantum yield measurements on this sample were carried out for the UV (355 nm) and visible (577 nm) to NIR DC, and the obtained values were 81 ± 10% and 37 ± 5, respectively. They confirm a DC processes upon UV excitation in these phosphors. We found, however, that Li^+ introduction does not play any direct role in the DC process, although Li^+ presence has proven to increase considerably the photoluminescence intensity of the samples [39]. In spite of it, Li^+ introduction impacts positively on the structure of this material (improving crystallinity, reducing defects, promoting Nd^{3+}/Yb^{3+} pairs), as confirmed by excitation-emission spectra and time decay analysis. Therefore, the spectral conversion capability exhibited by these phosphors is attractive to enhance the energy conversion efficiency of commercial crystalline-silicon (c-Si) based solar cells beyond the theoretical limits imposed by their mismatch with the solar spectrum.

Author statement

J. De Anda: Investigation, Writing – original draft, synthesis of samples, analysis and interpreting results. F. Enrichi: Theoretical and experimental analysis discussion, review, and editing. G. C. Righini: Theoretical and experimental analysis discussion, review and editing. C. Falcony: Investigation, worked on the manuscript, experimental measurements, analysis and data interpretation. All authors discussed the results and commented on the manuscript.

Declaration of competing interest

The authors declare that they have no known competing financial interests or personal relationships that could have appeared to influence the work reported in this paper.

Acknowledgments

The authors acknowledge the technical assistance of Z. Rivera, M. Guerrero from physics department of CINVESTAV-IPN. We also thank CONACyT for the financial support (Project A1-S-26432 and Scholarship 640301).

References

[1] R.T. Wegh, H. Donker, K.D. Oskam, A. Meijerink, Visible quantum cutting in $LiGdF_4:Eu^{3+}$ through downconversion, Science 283 (80) (1999) 663–666, https://doi.org/10.1126/science.283.5402.663.

[2] R.T. Wegh, H. Donker, E.V.D. Van Loef, K.D. Oskam, A. Meijerink, Quantum cutting through downconversion in rare-earth compounds, J. Lumin. 87 (2000) 1017–1019, https://doi.org/10.1016/S0022-2313(99)00514-1.

[3] S. Ye, B. Zhu, J. Chen, J. Luo, J.R. Qiu, Infrared quantum cutting in Tb^{3+}, Yb^{3+} codoped transparent glass ceramics containing CaF_2 nanocrystals, Appl. Phys. Lett. 92 (2008) 90–93, https://doi.org/10.1063/1.2907496.

[4] B.M. Van Der Ende, L. Aarts, A. Meijerink, Near-infrared quantum cutting for photovoltaics, Adv. Mater. 21 (2009) 3073–3077, https://doi.org/10.1002/adma.200802220.

[5] Q.Y. Zhang, X.Y. Huang, Recent progress in quantum cutting phosphors, Prog. Mater. Sci. 55 (2010) 353–427, https://doi.org/10.1016/j.pmatsci.2009.10.001.

[6] Z. Liu, J. Li, L. Yang, Q. Chen, Y. Chu, N. Dai, Efficient near-infrared quantum cutting in Ce^{3+}-Yb^{3+} codoped glass for solar photovoltaic, Sol. Energy Mater. Sol. Cells 122 (2014) 46–50, https://doi.org/10.1016/j.solmat.2013.10.030.

[7] K. Grzeszkiewicz, L. Marciniak, W. Stręk, D. Hreniak, Downconversion in $Y_2Si_2O_7$: Pr^{3+}, Yb^{3+} polymorphs for its possible application as luminescent concentrators in photovoltaic solar-cells, J. Lumin. 177 (2016) 172–177, https://doi.org/10.1016/j.jlumin.2016.04.007.

[8] J. Hu, Y. Zhao, B. Chen, H. Xia, Y. Zhang, H. Ye, Efficient near-infrared downconversion and energy transfer mechanism in Pr^{3+}/Yb^{3+} co-doped $Na_5Y_9F_{32}$ single crystals, J. Lumin. 205 (2019) 500–507, https://doi.org/10.1016/j.jlumin.2018.10.002.

[9] L. Huang, Y. Wang, R. He, X. Kong, S. Lei, Y. Liu, B. Wang, H. Jiang, H. Liu, K. Liu, X. Hu, Solar-driven co-generation of electricity and water by evaporation cooling, Desalination 488 (2020) 114533, https://doi.org/10.1016/j.desal.2020.114533.

[10] W. Shockley, H.J. Queisser, Detailed balance limit of efficiency of p-n junction solar cells, J. Appl. Phys. 32 (1961) 510–519, https://doi.org/10.1063/1.1736034.

[11] A. Shalav, B.S. Richards, M.A. Green, Luminescent layers for enhanced silicon solar cell performance: up-conversion, Sol. Energy Mater. Sol. Cells 91 (2007) 829–842, https://doi.org/10.1016/j.solmat.2007.02.007.

[12] F. Enrichi, G.C. Righini, Solar cells and light management: materials, strategies and sustainability. https://doi.org/10.1016/C2017-0-04229-5, 2019.

[13] B.S. Richards, Luminescent layers for enhanced silicon solar cell performance: down-conversion, Sol. Energy Mater. Sol. Cells 90 (2006) 1189–1207, https://doi.org/10.1016/j.solmat.2005.07.001.

[14] B.M. Van Der Ende, L. Aarts, A. Meijerink, Lanthanide ions as spectral converters for solar cells, Phys. Chem. Chem. Phys. 11 (2009) 11081–11095, https://doi.org/10.1039/b913877c.

[15] T. Trupke, M.A. Green, P. Würfel, Improving solar cell efficiencies by down-conversion of high-energy photons, J. Appl. Phys. 92 (2002) 1668–1674, https://doi.org/10.1063/1.1492021.

[16] P. Vergeer, T.J.H. Vlugt, M.H.F. Kox, M.I. Den Hertog, J.P.J.M. Van Der Herden, A. Meijerink, Quantum cutting by cooperative energy transfer in $Yb_xY_{1-x}PO_4:Tb^{3+}$, Phys. Rev. B Condens. Matter 71 (2005) 1–11, https://doi.org/10.1103/PhysRevB.71.014119.

[17] S.V. Kuznetsov, O.A. Morozov, V.G. Gorieva, M.N. Mayakova, M.A. Marisov, V. V. Voronov, A.D. Yapryntsev, V.K. Ivanov, A.S. Nizamutdinov, V.V. Semashko, P. P. Fedorov, Synthesis and luminescence studies of CaF_2:Yb:Pr solid solutions powders for photonics, J. Fluor. Chem. 211 (2018) 70–75, https://doi.org/10.1016/j.jfluchem.2018.04.008.

[18] W. Xu, Y. Hu, L. Zheng, Z. Zhang, W. Cao, H. Liu, Enhanced NIR-NIR luminescence from $CaWO_4$:Nd^{3+}/Yb^{3+} phosphors by Li^+ codoping for thermometry and optical heating, J. Lumin. J. 208 (2019) 415–423, https://doi.org/10.1016/j.jlumin.2019.01.005.

[19] N.A.M. Saeed, E. Coetsee, H.C. Swart, Down-conversion of YOF: Pr^{3+}, Yb^{3+} phosphor, Opt. Mater. (Amst). 110 (2020) 110516, https://doi.org/10.1016/j.optmat.2020.110516.

[20] L. de A. Florêncio, L.A. Gómez-Malagón, B.C. Lima, A.S.L. Gomes, J.A.M. Garcia, L. R.P. Kassab, Efficiency enhancement in solar cells using photon down-conversion in Tb/Yb-doped tellurite glass, Sol. Energy Mater. Sol. Cells 157 (2016) 468–475, https://doi.org/10.1016/j.solmat.2016.07.024.

[21] L. Wang, Z. Yang, Y.F. Li, R. Yang, Z. Dai, S. Hu, L. Sun, Y. Tong, Fluorescence resonance energy transfer of CaF_2: Eu^{2+}, Tb^{3+} applied to dye-sensitized solar cells, Spectrochim. Acta Part A Mol. Biomol. Spectrosc. 202 (2018) 76–80, https://doi.org/10.1016/j.saa.2018.05.015.

[22] N.P. Singh, N. Kumam, L.P. Singh, N.R. Singh, S.K. Srivastava, Luminescent enhancement study of 3Tb,5Ce,5Li:CaF_2: effect of Li^+ ion concentration and hyperthermia applications of 3Tb:CaF_2/Fe_3O_4 nanocomposite, New J. Chem. 43 (2019) 1328–1339, https://doi.org/10.1039/c8nj04057e.

[23] L. Zur, C. Armellini, S. Belmokhtar, A. Bouajaj, E. Cattaruzza, A. Chiappini, F. Coccetti, M. Ferrari, F. Gonella, G.C. Righini, E. Trave, A. Vomiero, F. Enrichi, Comparison between glass and glass-ceramic silica-hafnia matrices on the down-conversion efficiency of Tb^{3+}/Yb^{3+} rare earth ions, Opt. Mater. (Amst). 87 (2019) 102–106, https://doi.org/10.1016/j.optmat.2018.05.008.

[24] F. Enrichi, C. Armellini, S. Belmokhtar, A. Bouajaj, A. Chiappini, M. Ferrari, A. Quandt, G.C. Righini, A. Vomiero, L. Zur, Visible to NIR downconversion process in Tb^{3+}-Yb^{3+} codoped silica-hafnia glass and glass-ceramic sol-gel waveguides for solar cells, J. Lumin. 193 (2018) 44–50, https://doi.org/10.1016/j.jlumin.2017.08.027.

[25] D.Y. Shi, S. bao Lin, X. xia Zhao, A. ling Feng, Q. Xu, Near-infrared quantum cutting in Tm^{3+}/Yb^{3+}-doped phosphate glasses, Results Phys. 19 (2020) 103411, https://doi.org/10.1016/j.rinp.2020.103411.

[26] M.Y.A. Yagoub, H.C. Swart, E. Coetsee, Energy transfer study between Ce^{3+} and Tb^{3+} ions in a calcium fluoride crystal for solar cell applications, J. Lumin. 187 (2017) 96–101, https://doi.org/10.1016/j.jlumin.2017.02.066.

[27] Y. Zhydachevskyy, I.I. Syvorotka, V. Tsiumra, M. Baran, L. Lipińska, A. Wierzbicka, A. Suchocki, Quantum efficiency of the down-conversion process in Bi^{3+}–Yb^{3+} and Ce^{3+}–Yb^{3+} co-doped garnets, Sol. Energy Mater. Sol. Cells 185 (2018) 240–251, https://doi.org/10.1016/j.solmat.2018.05.037.

[28] K. Deng, T. Gong, L. Hu, X. Wei, Y. Chen, M. Yin, Efficient near-infrared quantum cutting in $NaYF_4$: Ho^{3+}, Yb^{3+} for solar photovoltaics, Opt Express 19 (2011) 1749, https://doi.org/10.1364/oe.19.001749.

[29] A. Verma, S.K. Sharma, Down-conversion from Er^{3+}-Yb^{3+} codoped CaMoO4 phosphor: a spectral conversion to improve solar cell efficiency, Ceram. Int. 43 (2017) 8879–8885, https://doi.org/10.1016/j.ceramint.2017.04.023.

[30] X. Chen, Y. Zhu, D. Zhou, W. Xu, J. Zhu, G. Pan, Z. Yin, H. Wang, S. Cui, H. Song, Size-dependent downconversion near-infrared emission of $NaYF_4$:Yb^{3+},Er^{3+} nanoparticles, J. Mater. Chem. C. 5 (2017) 2451–2458, https://doi.org/10.1039/c7tc00267j.

[31] V.S. Singh, C.P. Joshi, S.V. Moharil, P.L. Muthal, S.M. Dhopte, Modification of luminescence spectra of CaF2: Eu^{2+}, Luminescence 30 (2015) 1101–1105, https://doi.org/10.1002/bio.2865.

[32] N.D. Alharbi, Size controlled CaFnanocubes and their dosimetric properties using photoluminescence technique, J. Nanomater. 2015 (2015), https://doi.org/10.1155/2015/136957.

[33] D. Chen, Y. Yu, H. Lin, P. Huang, Z. Shan, Y. Wang, Ultraviolet-blue to near-infrared downconversion of Nd^{3+}-Yb^{3+} couple, Opt. Lett. 35 (2010) 220, https://doi.org/10.1364/ol.35.000220.

[34] J.M. Meijer, L. Aarts, B.M. Van Der Ende, T.J.H. Vlugt, A. Meijerink, Downconversion for solar cells in YF_3: Nd^{3+}, Yb^{3+}, Phys. Rev. B Condens. Matter 81 (2010) 1–9, https://doi.org/10.1103/PhysRevB.81.035107.

[35] H. Lin, D. Chen, Y. Yu, Z. Shan, P. Huang, A. Yang, Y. Wang, Broadband UV excitable near-infrared downconversion luminescence in Eu^{2+}/Yb^{3+}:CaF_2 nanocrystals embedded glass ceramics, J. Alloys Compd. 509 (2011) 3363–3366, https://doi.org/10.1016/j.jallcom.2010.12.066.

[36] J. Hu, Y. Zhang, H. Xia, H. Ye, B. Chen, Y. Zhu, NIR downconversion and energy transfer mechanisms in Tb^{3+}/Yb^{3+} codoped $Na_5Lu_9F_{32}$ single crystals, Cite This Inorg. Chem. 57 (2018) 7792–7796, https://doi.org/10.1021/acs.inorgchem.8b00867.

[37] B. Ritter, T. Krahl, K. Rurack, E. Kemnitz, Nanoscale CaF_2 doped with Eu^{3+} and Tb^{3+}through fluorolytic sol-gel synthesis, J. Mater. Chem. C. 2 (2014) 8607–8613, https://doi.org/10.1039/c4tc01073f.

[38] M. Back, R. Marin, M. Franceschin, N. Sfar Hancha, F. Enrichi, E. Trave, S. Polizzi, Energy transfer in color-tunable water-dispersible Tb-Eu codoped CaF_2 nanocrystals, J. Mater. Chem. C. 4 (2016) 1906–1913, https://doi.org/10.1039/c5tc03355a.

[39] J. Zhao, Y. Zhu, J. Wu, F. Chen, Journal of Colloid and Interface Science Microwave-assisted solvothermal synthesis and upconversion luminescence of CaF_2:Yb^{3+}/Er^{3+} nanocrystals, J. Colloid Interface Sci. 440 (2015) 39–45, https://doi.org/10.1016/j.jcis.2014.10.031.

[40] S. Li, Q. Huang, Y. Jiang, M. Hu, Near-infrared quantum cutting for solar cells in Ce^{3+}-Yb^{3+} Co-doped CaF2 nanoparticles, J. Nanosci. Nanotechnol. 16 (2016) 3679–3683, https://doi.org/10.1166/jnn.2016.11823.

[41] S.V. Kuznetsov, A.S. Nizamutdinov, M.N. Mayakova, E.I. Madirov, A.R. Khadiev, V. G. Gorieva, V.V. Voronov, A.D. Yapryntsev, V.K. Ivanov, V.V. Semashko, P. P. Fedorov, Synthesis and down-conversion luminescence investigation of CaF_2:Yb:Ce powders for photonics, J. Fluor. Chem. 222–223 (2019) 46–50, https://doi.org/10.1016/j.jfluchem.2019.04.010.

[42] V. Petit, P. Camy, J.L. Doualan, R. Moncorǵ, Cw and tunable laser operation of Yb^{3+} in Nd:Yb: CaF_2, Appl, Phys. Lett. 88 (2006) 1–3, https://doi.org/10.1063/1.2169887.

[43] B. Xu, H. He, Z. Gu, S. Jin, Y. Ma, T. Zhai, Improving 800 nm triggered upconversion emission for lanthanide-doped CaF_2 nanoparticles through sodium ion doping, J. Phys. Chem. C 121 (2017) 18280–18287, https://doi.org/10.1021/acs.jpcc.7b05639.

[44] J. De Anda, E.F. Huerta, J.U. Balderas, G.C. Righini, C. Falcony, The effect of Li+ incorporation in Yb^{3+}-Nd^{3+} co-doped CaF_2 phosphors over the NIR photoluminescence emission excited under visible light, Ceram. Int. 47 (2021) 4694–4701, https://doi.org/10.1016/j.ceramint.2020.10.037.

[45] U. Caldiño, D. Jaque, E. Martín-Rodríguez, M.O. Ramírez, J. García Solé, A. Speghini, M. Bettinelli, $Nd^{3+} \rightarrow Yb^{3+}$ resonant energy transfer in the ferroelectric $Sr_{0.6}Ba_{0.4}Nb_2O_6$ laser crystal, Phys. Rev. B Condens. Matter 77 (2008) 6–13, https://doi.org/10.1103/PhysRevB.77.075121.

[46] A. Vyas, C.P. Joshi, S.V. Moharil, Sensitization of nir emission by tetravalent cerium in K_2CeO_3:Nd,Yb, J. Alloys Compd. 763 (2018) 159–163, https://doi.org/10.1016/j.jallcom.2018.05.285.

[47] M. Rathaiah, A.D. Lozano-Gorrín, P. Babu, C.K. Jayasankar, V. Lavín, V. Venkatramu, Efficient Nd^{3+} sensitized Yb^{3+} emission and infrared-to-visible energy conversion in gallium nano-garnets, RSC Adv. 6 (2016) 78669–78677, https://doi.org/10.1039/c6ra13729f.

[48] S. Shi, Q. Shi, C. Cui, L. Wang, Y. Tian, P. Huang, Near-infrared luminescence and energy transfer processes in LaOF:Nd^{3+}, Yb^{3+}, RSC Adv. 6 (2016) 92127–92132, https://doi.org/10.1039/c6ra19953d.

[49] X. Bian, Q. Shi, C. Cui, L. Wang, Y. Tian, B. Xu, Z.K. Mamytbekov, P. Huang, Near-infrared luminescence and energy transfer mechanism in K_2YF_5:Nd^{3+}, Yb^{3+}, Mater. Res. Bull. 110 (2019) 102–106, https://doi.org/10.1016/j.materresbull.2018.10.024.

[50] S. Ye, Y. Katayama, S. Tanabe, Down conversion luminescence of Tb^{3+}-Yb^{3+} codoped SrF_2 precipitated glass ceramics, J. Non-Cryst. Solids 357 (2011) 2268–2271, https://doi.org/10.1016/j.jnoncrysol.2010.11.083.

[51] B. Xu, D. Li, Z. Huang, C. Tang, W. Mo, Y. Ma, Alleviating luminescence concentration quenching in lanthanide doped CaF2 based nanoparticles through Na^{+} ion doping, Dalton Trans. 47 (2018) 7534–7540, https://doi.org/10.1039/c8dt00519b.

[52] Y. Li, P. Zhang, H. Ning, J. Zeng, Y. Hou, L. Jing, C. Liu, M. Gao, Emitting/sensitizing ions spatially separated lanthanide nanocrystals for visualizing tumors simultaneously through up- and down-conversion near-infrared II luminescence in vivo, Small 15 (2019) 1–12, https://doi.org/10.1002/smll.201905344.

[53] S.K. Ranjan, A.K. Soni, V.K. Rai, Nd^{3+}-Yb^{3+}/Nd^{3+}-Yb^{3+}-Li+ co-doped Gd2O3 phosphors for up and down conversion luminescence, Luminescence 33 (2018) 647–653, https://doi.org/10.1002/bio.3458.

[54] Q. Cheng, J. Sui, W. Cai, Enhanced upconversion emission in Yb^{3+} and Er^{3+} codoped $NaGdF_4$ nanocrystals by introducing Li + ions, Nanoscale 4 (2012) 779–784, https://doi.org/10.1039/C1NR11365H.

[55] X. Chen, Z. Liu, Q. Sun, M. Ye, F. Wang, Upconversion emission enhancement in Er^{3+}/Yb^{3+}- codoped $BaTiO_3$ nanocrystals by tridoping with Li^{+} ions, Opt Commun. 284 (2011) 2046–2049, https://doi.org/10.1016/j.optcom.2010.12.007.

[56] E.F. Huerta, J. De Anda, I. Martínez-Merlin, U. Caldiño, C. Falcony, Near-infrared luminescence spectroscopy in yttrium oxide phosphor activated with Er 3þ , Li þ and Yb 3þ ions for application in photovoltaic systems, J. Lumin. 224 (2020) 117271, https://doi.org/10.1016/j.jlumin.2020.117271.

[57] O. Soriano-Romero, R.L. Flores-Cruz, R. Lozada-Morales, U. Caldiño, C. Falcony, S. Cármona-Téllez, I. Camarillo, A. Méndez-Blas, A.N. Meza-Rocha, Tunable white light emission in zinc phosphate glasses activated with Ag^{+}_{mn} clusters and Sm^{3+}, J. Lumin. 222 (2020) 1–9, https://doi.org/10.1016/j.jlumin.2020.117104.

Bibliography

[1] The world Counts. `https://www.theworldcounts.com/challenges/climate-change/energy/global-energy-consumption/story`, 2021.

[2] Xiaodong Pi, Qing Li, Dongsheng Li, and Deren Yang. Spin-coating silicon-quantum-dot ink to improve solar cell efficiency. *Solar Energy Materials and Solar Cells*, 95(10):2941–2945, 2011.

[3] Jianhua Han, Songping Luo, Xuewen Yin, Yu Zhou, Hui Nan, Jianbao Li, Xin Li, Dan Oron, Heping Shen, and Hong Lin. Hybrid pbs quantum-dot-in-perovskite for high-efficiency perovskite solar cell. *Small*, 14(31):1801016, 2018.

[4] T. Trupke, M. A. Green, and P. Würfel. Improving solar cell efficiencies by down-conversion of high-energy photons. *Journal of Applied Physics*, 92(3):1668–1674, 2002.

[5] D. Serrano, A. Braud, J.-L. Doualan, P. Camy, and R. Moncorgé. Visible to infrared down conversion in rare-earth doped fluorides for luminescent solar converters. *Next Generation (Nano) Photonic and Cell Technologies for Solar Energy Conversion II*, 8111:811104, 2011.

[6] Shiman Shi, Qiufeng Shi, Cai'e Cui, Lei Wang, Yue Tian, and Ping Huang. Near-infrared luminescence and energy transfer processes in LaOF:Nd^{3+}, Yb^{3+}. *RSC Adv.*, 6:91127–91132, 2016.

[7] Kaimo Deng, Tao Gong, Lingxun Hu, Xiantao Wei, Yonghu Chen, and Min Yin. Efficient near-infrared quantum cutting in $NaYF_4$: Ho^{3+}, Yb^{3+} for solar photovoltaics. *Optics Express*, 19(3):1749, 2011.

[8] Jianxu Hu, Yun Zhao, Baojiu Chen, Haiping Xia, Yuanpeng Zhang, and Huanqing Ye. Efficient near-infrared downconversion and energy transfer mechanism in Pr^{3+}/Yb^{3+} co-doped $Na_5Y_9F_{32}$ single crystals. *Journal of Luminescence*, 205:500–507, 2019.

[9] Hang Lin, Daqin Chen, Yunlong Yu, Zhifa Shan, Ping Huang, Anping Yang, and Yuansheng Wang. Broadband UV excitable near-infrared downconversion luminescence in Eu^{2+}/Yb^{3+}:CaF_2 nanocrystals embedded glass ceramics. *Journal of Alloys and Compounds*, 509(7):3363–3366, 2011.

[10] Jing Zhao, Ying Jie Zhu, Jin Wu, and Feng Chen. Microwave-assisted solvothermal synthesis and upconversion luminescence of CaF_2: Yb^{3+}/Er^{3+} nanocrystals. *Journal of Colloid and Interface Science*, 440:39–45, 2015.

[11] M. Back, R. Marin, M. Franceschin, N. Sfar Hancha, F. Enrichi, E. Trave, and S. Polizzi. Energy transfer in color-tunable water-dispersible Tb-Eu codoped CaF_2 nanocrystals. *Journal of Materials Chemistry C*, 4(9):1906–1913, 2016.

[12] F. Enrichi, C. Armellini, S. Belmokhtar, A. Bouajaj, A. Chiappini, M. Ferrari, A. Quandt, G. C. Righini, A. Vomiero, and L. Zur. Visible to NIR downconversion process in Tb^{3+}-Yb^{3+} codoped silica-hafnia glass and glass-ceramic sol-gel waveguides for solar cells. *Journal of Luminescence*, 193(July 2017):44–50, 2018.

[13] Jianxu Hu, Yuanpeng Zhang, Haiping Xia, Huanqing Ye, Baojiu Chen, and Yongsheng Zhu. NIR Downconversion and Energy Transfer Mechanisms in Tb $^{3+}$ /Yb $^{3+}$ Codoped Na 5 Lu 9 F 32 Single Crystals. *Cite This: Inorg. Chem*, 57:7792–7796, 2018.

[14] Ningthoujam Premananda Singh, Nandini Kumam, Laishram Priyobarta Singh, Nongmaithem Rajmuhon Singh, and Sri Krishna Srivastava. Luminescent enhance-

ment study of 3Tb,5Ce,5Li:CaF_2: Effect of Li^+ ion concentration and hyperthermia applications of 3Tb:CaF_2/Fe_3O_4 nanocomposite. *New Journal of Chemistry*, 43(3):1328–1339, 2019.

[15] M. Y.A. Yagoub, H. C. Swart, and E. Coetsee. Energy transfer study between Ce^{3+} and Tb^{3+} ions in a calcium fluoride crystal for solar cell applications. *Journal of Luminescence*, 187:96–101, 2017.

[16] Benjamin Ritter, Thoralf Krahl, Knut Rurack, and Erhard Kemnitz. Nanoscale CaF2doped with $Eu^{3+}$and Tb^{3+}through fluorolytic sol-gel synthesis. *Journal of Materials Chemistry C*, 2(40):8607–8613, 2014.

[17] Lege Wang, Zijian Yang, You Fen Li, Ru Yang, Zhigang Dai, Shuqiao Hu, Liangliang Sun, and Yaoyao Tong. Fluorescence resonance energy transfer of CaF_2: Eu^{2+}, Tb^{3+} applied to dye-sensitized solar cells. *Spectrochimica Acta - Part A: Molecular and Biomolecular Spectroscopy*, 202:76–80, 2018.

[18] Suwen Li, Qingqing Huang, Yi Jiang, and Min Hu. Near-Infrared Quantum Cutting for Solar Cells in Ce^{3+}-Yb^{3+} Co-Doped CaF_2 Nanoparticles. *Journal of Nanoscience and Nanotechnology*, 16(4):3679–3683, 2016.

[19] S. V. Kuznetsov, A. S. Nizamutdinov, M. N. Mayakova, E. I. Madirov, A. R. Khadiev, V. G. Gorieva, V. V. Voronov, A. D. Yapryntsev, V. K. Ivanov, V. V. Semashko, and P. P. Fedorov. Synthesis and down-conversion luminescence investigation of CaF_2:Yb:Ce powders for photonics. *Journal of Fluorine Chemistry*, 222-223(April):46–50, 2019.

[20] V. Petit, P. Camy, J. L. Doualan, and R. Moncorǵ. Cw and tunable laser operation of Yb^{3+} in Nd:Yb: CaF_2. *Applied Physics Letters*, 88(5):1–3, 2006.

[21] IEA, Paris. `https://www.iea.org/reports/global-energy-review-2021`, 2021.

[22] Lennon Wade. `https://lynniezulu.com/what-is-the-am1-5g-spectrum/`, 2021.

[23] William Shockley and Hans J. Queisser. Detailed balance limit of efficiency of p-n junction solar cells. *Journal of Applied Physics*, 32(3):510–519, 1961.

[24] Mugdha V. Dambhare, Bhavana Butey, and S. V. Moharil. Solar photovoltaic technology: A review of different types of solar cells and its future trends. *Journal of Physics: Conference Series*, 1913(1), 2021.

[25] Jung Min Ji, Haoran Zhou, Yu Kyung Eom, Chul Hoon Kim, and Hwan Kyu Kim. 14.2% Efficiency Dye-Sensitized Solar Cells by Co-sensitizing Novel Thieno[3,2-b]indole-Based Organic Dyes with a Promising Porphyrin Sensitizer. *Advanced Energy Materials*, 10(15):1–12, 2020.

[26] Mikko Kokkonen, Parisa Talebi, Jin Zhou, Somayyeh Asgari, Sohail Ahmed Soomro, Farid Elsehrawy, Janne Halme, Shahzada Ahmad, Anders Hagfeldt, and Syed Ghufran Hashmi. Advanced research trends in dye-sensitized solar cells. *Journal of Materials Chemistry A*, 9(17):10527–10545, 2021.

[27] Naveen Kumar Tailor, Mojtaba Abdi-Jalebi, Vinay Gupta, Hanlin Hu, M. Ibrahim Dar, Gang Li, and Soumitra Satapathi. Recent progress in morphology optimization in perovskite solar cell. *Journal of Materials Chemistry A*, 8(41):21356–21386, 2020.

[28] Mengmeng Hao, Yang Bai, Stefan Zeiske, Long Ren, Junxian Liu, Yongbo Yuan, Nasim Zarrabi, Ningyan Cheng, Mehri Ghasemi, Peng Chen, Miaoqiang Lyu, Dongxu He, Jung Ho Yun, Yi Du, Yun Wang, Shanshan Ding, Ardalan Armin, Paul Meredith, Gang Liu, Hui Ming Cheng, and Lianzhou Wang. Ligand-assisted cation-exchange engineering for high-efficiency colloidal $Cs_{1x}FA_xPbI_3$ quantum dot solar cells with reduced phase segregation. *Nature Energy*, 5(1):79–88, 2020.

[29] Esther López, Antonio Martí, Elisa Antolín, and Antonio Luque. On the potential of silicon intermediate band solar cells. *Energies*, 13(12), 2020.

[30] Satya Saripalli and Vikram Dalal. Microcrystalline silicon-germanium solar cells fabricated using vhf pecvd. In *2008 IEEE International Conference on Electro/Information Technology*, pages 414–418, 2008.

[31] S. Gloger, N. Brinkmann, and B. Terheiden. Low surface recombination velocity using amorphous silicon on industrial-type cleaned surfaces. *Energy Procedia*, 8:666–671, 2011. Proceedings of the SiliconPV 2011 Conference (1st International Conference on Crystalline Silicon Photovoltaics).

[32] Siyu Wang, Wei-Hai Fang, and Run Long. Hydrogen passivated silicon grain boundaries greatly reduce charge recombination for improved silicon/perovskite tandem solar cell performance: Time domain ab initio analysis. *The Journal of Physical Chemistry Letters*, 10(10):2445–2452, 2019.

[33] J. Ajayan, D. Nirmal, P. Mohankumar, M. Saravanan, M. Jagadesh, and L. Arivazhagan. A review of photovoltaic performance of organic/inorganic solar cells for future renewable and sustainable energy technologies. *Superlattices and Microstructures*, 143:106549, 2020.

[34] Bryan M. van der Ende, Linda Aarts, and Andries Meijerink. Lanthanide ions as spectral converters for solar cells. *Phys. Chem. Chem. Phys.*, 11:11081–11095, 2009.

[35] William J. Evans. Perspectives in reductive lanthanide chemistry. *Coordination Chemistry Reviews*, 206-207:263–283, 2000.

[36] Jiming Liu, Shiwu Zhang, and Yiming Ye. Lanthanide Luminescence. volume 7 of *Springer Series on Fluorescence*, page 457. Springer Berlin Heidelberg, Berlin, Heidelberg, 2011.

[37] Jean Claude G. Bünzli and Svetlana V. Eliseeva. Intriguing aspects of lanthanide luminescence. *Chemical Science*, 4(5):1939–1949, 2013.

[38] Stephen Isadore Klink. *Synthesis and photophysics of light-converting lanthanide complexes*. PhD thesis, Universiteit Twente, Drienerlolaan 5, 7522 ME Enschede, Netherlands, 5 2000. An optional note.

[39] Gerhard H. Dieke. Spectra and energy levels of rare earth ions in crystals. *American Journal of Physics*, 38(3):399–400, 1970.

[40] George Blasse and BC Grabmaier. A general introduction to luminescent materials. In *Luminescent materials*, pages 1–9. Springer, 1994.

[41] Robert Withnall and Jack Silver. *Physics of Light Emission from Rare-Earth Doped Phosphors*, pages 1019–1028. Springer Berlin Heidelberg, Berlin, Heidelberg, 2012.

[42] Linda Aarts. Downconverion for solar cells with lanthanide ion couples. Technical report.

[43] U. Caldiño, D. Jaque, E. Martín-Rodríguez, M. O. Ramírez, J. García Solé, A. Speghini, and M. Bettinelli. $Nd^{3+} \rightarrow Yb^{3+}$ resonant energy transfer in the ferroelectric $Sr_{0.6}Ba_{0.4}Nb_2O_6$ laser crystal. *Physical Review B - Condensed Matter and Materials Physics*, 77(7):6–13, 2008.

[44] Mamilla Rathaiah, Antonio Diego Lozano-Gorrín, Palamandala Babu, Chalicheemalapalli Kulala Jayasankar, Víctor Lavín, and Vemula Venkatramu. Efficient Nd^{3+} sensitized Yb^{3+} emission and infrared-to-visible energy conversion in gallium nano-garnets. *RSC Advances*, 6(82):78669–78677, 2016.

[45] Eyring Carnall, Gscheneidner JR. *Handbook on the Physics and Chemistry o Rare Earths*. North-Holland Publishing Company, vol 4 edition, 1979.

[46] Dan Yuan, Weiwei Li, Bingchu Mei, and Jinghong Song. Synthesis and characterization of Nd^{3+}-doped CaF_2 nanoparticles. *Journal of Nanoscience and Nanotechnology*, 15(12):9741–9745, 2015.

[47] Ajay Vasudeo Rane, Krishnan Kanny, V.K. Abitha, and Sabu Thomas. Methods for Synthesis of Nanoparticles and Fabrication of Nanocomposites. In *Synthesis of Inorganic Nanomaterials*, pages 121–139. Elsevier Ltd., 2018.

[48] C Pandurangappa, B N Lakshminarasappa, and B M Nagabhushana. Synthesis and characterization of CaF_2 nanocrystals. *Journal of Alloys and Compounds*, 489:592–595, 2010.

[49] Xiaofan Zhao, Zining Yang, Xu Yang, Rui Wang, Maohui Yuan, Kai Han, Zongfu Jiang, Hongyan Wang, and Xiaojun Xu. Controlling the multicolor upconversion luminescence in CaF_2 nanocrystals doped with Yb^{3+} , Er^{3+} and Nd^{3+} ions under the excitation of a 808 nm laser. *Optical Materials Express*, 9(12):4578, 2019.

[50] Qian Cheng, Jiehe Sui, and Wei Cai. Enhanced upconversion emission in Yb^{3+} and Er^{3+} codoped $NaGdF_4$ nanocrystals by introducing Li^+ ions. *Nanoscale*, 4:779–784, 2012.

[51] Gorka Salas, Rocío Costo, and María del Puerto Morales. Synthesis of inorganic nanoparticles. In *Frontiers of Nanoscience*, volume 4, pages 35–79. 2012.

[52] Guoming Huang, Chun Hua Lu, and Huang Hao Yang. *Magnetic Nanomaterials for Magnetic Bioanalysis*. Elsevier Inc., 2018.

[53] E. F. Huerta, A. N. Meza-Rocha, R. Lozada-Morales, A. Speghini, S. Bordignon, and U. Caldiño. White, yellow and reddish-orange light generation in lithium-aluminum-zinc phosphate glasses co-doped with Dy^{3+}/Tb^{3+} and tri-doped with $Dy^{3+}/Tb^{3+}/Eu^{3+}$. *Journal of Luminescence*, 219:116882, 2020.

[54] Tian Xu, Nan Ding, Xiaojuan Yang, Quan Liu, Lixi Wang, Le Zhang, and Qitu Zhang. Influence of charge compensators $Li^+/Na^+/K^+$ on luminescence properties of Sr_2CeO_4:Eu^{3+}. *Journal of Materials Science: Materials in Electronics*, 27(10):10207–10212, 2016.

[55] Paolo Cortelletti, Marco Pedroni, Federico Boschi, Sonia Pin, Paolo Ghigna, Patrizia Canton, Fiorenzo Vetrone, and Adolfo Speghini. Luminescence of Eu^{3+} Activated CaF_2 and SrF_2 Nanoparticles: Effect of the Particle Size and Codoping with Alkaline Ions. *Crystal Growth and Design*, 18(2):686–694, 2018.

[56] Bing Xu, Dongyu Li, Zhen Huang, Chunliang Tang, Wenhao Mo, and Ying Ma. Alleviating luminescence concentration quenching in lanthanide doped CaF_2 based nanoparticles through Na^+ ion doping. *Dalton Transactions*, 47(22):7534–7540, 2018.

[57] Santosh Kumar Gupta, Kathi Sudarshan, Ashok Kumar Yadav, Ruma Gupta, Dibyendu Bhattacharyya, Shambhu Nath Jha, and Ramakant Mahadeo Kadam. Deciphering the Role of Charge Compensator in Optical Properties of $SrWO_4$:Eu^{3+}:A (A = Li^+, Na^+, K^+): Spectroscopic Insight Using Photoluminescence, Positron Annihilation, and X-ray Absorption. *Inorganic Chemistry*, 57(2):821–832, 2018.

[58] Wei Xu, Yuwei Hu, Longjiang Zheng, Zhiguo Zhang, Wenwu Cao, and Hailong Liu. Enhanced NIR-NIR luminescence from $CaWO_4$:Nd^{3+}/Yb^{3+} phosphors by Li^+ codoping for thermometry and optical heating. *Journal of Luminescence journal*, 208(December 2018):415–423, 2019.

[59] A. K. Singh, S. K. Singh, and S. B. Rai. Role of Li^+ ion in the luminescence enhancement of lanthanide ions: Favorable modifications in host matrices. *RSC Advances*, 4(51):27039–27061, 2014.

[60] E. F. Huerta, S. Carmona-Téllez, J. G. Cabañas-Moreno, and C. Falcony. Visible and near infrared upconversion photoluminescence from Y_2O_3:Er^{3+}, Yb^{3+}, Li^+ phosphors under 1532 nm excitation light. *Journal of Alloys and Compounds*, 732:422–428, 2018.

[61] J. De Anda, E.F. Huerta, J.U. Balderas, G.C. Righini, and C. Falcony. The effect of Li^+ incorporation in Yb^{3+}-Nd^{3+} co-doped CaF_2 phosphors over the NIR photolumines-

cence emission excited under visible light. *Ceramics International*, 47(4):4694–4701, feb 2021.

[62] Saurabh K. Sengar, B. R. Mehta, and Govind. Size and alloying induced changes in lattice constant, core, and valance band binding energy in Pd-Ag, Pd, and Ag nanoparticles: Effect of in-flight sintering temperature. *Journal of Applied Physics*, 112(1), 2012.

[63] Sheng Jiang, Jing Liu, Ligang Bai, Xiaodong Li, Yanchun Li, Shangming He, Shuai Yan, and Dongxu Liang. Anomalous compression behaviour in Nd_2O_3 studied by x-ray diffraction and Raman spectroscopy. *AIP Advances*, 8(2), 2018.

[64] Nakhaei Omolfajr, Shahtahmassebi Nasser, Rezaeeroknabadi Mahmood, and Ahmad Kompany. Synthesis and characterization of CaF_2 NPs with co-precipitation and hydrothermal methods. *Journal of Nanomedicine and Nanotechnology*, 2(5):10–13, 2011.

[65] Lihua He, Xiao Zou, Xiang He, Fengying Lei, Na Jiang, Qiaoji Zheng, Chenggang Xu, Yongfu Liu, and Dunmin Lin. Reducing Grain Size and Enhancing Luminescence of $NaYF_4$:Yb^{3+}, Er^{3+} Upconversion Materials. *Crystal Growth and Design*, 18(2):808–817, 2018.

[66] Bati Sn and Nd Yb. Photoluminescence , structural , morphology and dielectric properties of. *Journal of Scientific Research in Science*, 36(36):248–268, 2019.

[67] Shiman Shi, Qiufeng Shi, Cai'E Cui, Lei Wang, Yue Tian, and Ping Huang. Near-infrared luminescence and energy transfer processes in LaOF:Nd^{3+}, Yb^{3+}. *RSC Advances*, 6(94):92127–92132, 2016.

[68] O. Soriano-Romero, R. L. Flores-Cruz, R. Lozada-Morales, U. Caldiño, C. Falcony, S. Cármona-Téllez, I. Camarillo, A. Méndez-Blas, and A. N. Meza-Rocha. Tunable

white light emission in zinc phosphate glasses activated with Ag_m^{n+} clusters and Sm^{3+}. *Journal of Luminescence*, 222:1–9, 2020.

[69] A. D. Sontakke, K. Biswas, A. K. Mandal, and K. Annapurna. Concentration quenched luminescence and energy transfer analysis of Nd^{3+} ion doped Ba-Al-metaphosphate laser glasses. *Applied Physics B: Lasers and Optics*, 101(1-2):235–244, 2010.

[70] J.L. Sommerdijk, A. Bril, and A.W. de Jager. Two photon luminescence with ultraviolet excitation of trivalent praseodymium. *Journal of Luminescence*, 8(4):341–343, 1974.

[71] W.W. Piper, J.A. DeLuca, and F.S. Ham. Cascade fluorescent decay in Pr^{3+}-doped fluorides: Achievement of a quantum yield greater than unity for emission of visible light. *Journal of Luminescence*, 8(4):344–348, 1974.

[72] René T. Wegh, Harry Donker, Koenraad D. Oskam, and Andries Meijerink. Visible quantum cutting in $LiGdF_4$:Eu^{3+} through downconversion. *Science*, 283(5402):663–666, 1999.

[73] Janne Mieke Meijer, Linda Aarts, Bryan M. Van Der Ende, Thijs J.H. Vlugt, and Andries Meijerink. Downconversion for solar cells in YF_3: Nd^{3+}, Yb $^{3+}$. *Physical Review B - Condensed Matter and Materials Physics*, 81(3):1–9, 2010.